POLITECNICO DI TORINO

SCUOLA INTERPOLITECNICA DI DOTTORATO

Doctoral Program in Biomedical Engineering and Bioengineering

Final Dissertation

Computer Aided Diagnosis systems for MR cancer detection

Valentina Giannini

Tutor
Prof. Filippo Molinari
Co-tutors
Dott. Daniele Regge
Prof. Kim Butts-Pauly

Co-ordinator of the Research Doctorate Course
Prof.ssa Cristina Bignardi

January 2012

Laugh as we always laughed
at the little jokes we enjoyed together.

Summary

The research activity conducted during my PhD aims to develop two different Computer Aided Diagnosis (CAD) systems for breast and prostate cancer diagnosis using Magnetic Resonance Imaging.
During the first part of this thesis I will illustrate a fully automatic CAD system for breast cancer detection and diagnosis with Dynamic Contrast Enhanced MRI (DCE-MRI) developed by our group. The main goal of a CAD system is lesions detection and characterization. The processing pipeline includes automatic segmentation of the breast and axillary regions, registration of unenhanced and contrast-enhanced frames, lesion detection and classification according to kinetic and morphological criteria. During my PhD I, firstly, studied the physiological phenomena correlated to breast tumors growth and diagnosis, then I elaborated and created C++ algorithms for:

1. breasts segmentation, where the breasts and axillary regions are automatically identified in order to reduce the computational burden and preventing false positives (FP) due to enhancing structures (such as the heart and extra-breast vessels) which are not of clinical interest.

2. lesion detection, in which suspicious areas showing contrast enhancement are automatically segmented and FPs are identified and discarded.

These step are innovative as they are fully automatic, thus they do not suffer of inter- and intra-operator variability, and because of the normalization process, based on the mammary arteries segmentation, that makes the system able to deal with images coming from different centers, thus having different acquisition parameters. This work is being performed in collaboration with the Institute for Cancer Research and Treatment (IRCC) of Candiolo (MD Daniele Regge), and with i-m3D S.p.A., which designs, develops, produces and markets medical devices intended for early diagnosis in medical imaging. Thanks to the

contribution of i-m3D, I could register a patent based on these algorithms called "Method and system for the automatic recognition of lesions in a set of breast magnetic resonance images".

The second part of my thesis will concern the development of a CAD system for prostate cancer. The importance of this project is associated to the recent interest in adapting focal methods of tissue ablation, such as cryotherapy and Focused Ultrasound guided by MR (MRgFUS), to cure or control localized prostate cancer. Focal treatments rely on imaging to locate tumor, to determine the staging of disease, to detect recurrences and to guide the treatment. The aim of this part of my PhD was to create a multispectral computer aided diagnosis system able to: a) detect the tumor in order to guide real-time biopsy, b) characterize the malignancy of the lesion and c) guide the local treatment, by adopting a new multispectral approach. In this project I, actively, elaborated and developed C++ algorithm to register different datasets and to monitor the focal treatment using Diffusion Weighted-MRI (DWI) self-made acquisitions.The registration between T2-w, DCE-MRI and DWI images are applied in order to correct for patients movements and DWI distortions. Results obtained within 19 patients showed a Dice's overlap coefficient higher than 0.7, considered optimal in literature.

Monitoring the focal therapy was the aim of the last part of this project, that I actively developed during a visiting period in the Radiological Science Laboratory of the Stanford University (Kim Butts Pauly Research Lab). The main goal was to characterize the role of the DWI during MRgFUS. DWI, in fact, is very sensitive to cell death and tissue damage and information can be used to evaluate the treatment without relocating the patient and the applicators and without involving the administration of contrast agent. In this study, I wanted to assess the use of DWI images to estimate prostate tissue damage during HIFU ablation, by measuring diffusion coefficients of canine prostate pre and post ablation, using multiple b-factors ranging up to 3500 s/mm^2. This study demonstrated a bi-exponential decay of the signal increasing the b-values suggesting the presence of two different type of diffusion, called fast and slow.

In conclusion, during my PhD, I obtained the following original and novel goals:

a. I actively contributed to develop a fully automatic CAD system for breast cancer diagnosis able to deal with images coming from different center. This goal is innovative because in literature there are few methods completely automatic, and they work only with MRI dataset acquired without fat-saturation. Fat-saturation has

been introduced to enhance the contrast between lesion and surrounding tissue and to overcome the limitations due to subtraction artifacts, however, it introduces additional challenges for breast lesion segmentation, especially due to the lower signal-to-noise-ratio (SNR) within the breasts.

b. I developed a CAD system to detect and diagnose prostate cancer, that uses the novel approach of a multispectral analysis, that is the combinations of parameters coming from different datasets (i.e. DWI, DCE, T2-weighted sequences). The multispectral approach is able to improve the sensibility of the system, but makes the analysis more complex, even for the experienced radiologist.

c. I elaborated a new method to monitor focal treatment of the prostate cancer, using DWI sequences, therefore, conversely to the gold standard used for this scope (contrast enhanced MRI), without the administration of a contrast agent.

Acknowledgements

I am heartily thankful to my tutor, Filippo Molinari, for introducing me to the world of medical imaging, and for his encouragement, supervision and support, from the preliminary to the concluding level, that enabled me to develop an understanding of the subject.
I am deeply grateful to Dr. Daniele Regge, for creating from scratch our research group, and for trusting in it so passionately to give us a room in his Department at IRCC. The ongoing "Medical Imaging Lab", is largely due to Daniele's vision, to his warm and friendly personality, and to his ability to deal calmly and rationally with any situation. Moreover, it was due to his valuable guidance, cheerful enthusiasm and ever-friendly nature that I was able to complete my research work in a respectable manner.
My special thanks to Prof. Kim Butts-Pauly, for having me in her amazing group at Lucas Center (Stanford University). I have been extraordinarily lucky to have spent 6 months there. There are so many wonderful things that could be said about Lucas—the people, the "tea time", the open doors, the atmosphere, countless interesting visitors and the diversity of interests. It is hard to imagine a more stimulating and encouraging academic environment. It will be difficult and sad to leave Lucas, Lena, Rachelle, "the girls", and all the people who made me grow up as a researcher and as a person. I would not have the same great experience there without Lena, who took care of me, from the first step at SFO to the last one at SFO, always offering unconditional help and friendship.
I would also like to convey my deep regards to Prof. Elsa Angelini, and Prof. Dr. Gillian Newstead for allowing their precious time to read the manuscript and providing me their valuable suggestions. I wish to thank, also, Prof. Francesco Sardanelli, Dr. Laura Martincich, Dr. Filippo Russo, Dr. Ilaria Bertotto, Dr. Luca Carbonaro, and Dr. Enrico Armando for patiently creating the ground truth of the database and for helping me with all the medical doubts.

My thesis, would not be the same without the precious help and cooperation of my colleagues Anna, Massimo and Diego, and most important my days at work would absolutely not be the same without Anna's friendship, cheerfulness, and kindness.
I wish to thank my parents for their constant support and encouragement in all my professional endeavors, for setting high moral standards and supporting me through their hard work, and for their unselfish love and affection. I want to thank Alessio and my special friends, Gessica, Anna and Alessandra, that supported me in hundreds of ways during my life, and whose love make my life an amazing trip.
Finally, I want to dedicate this thesis to my beloved grandmother. She is not here to see her granddaughter reaching a such important goal, but she was so proud of me during my studies, and she always trusted in me, and in my abilities. Her spirits and teaching, will always be with me.
This research was supported by a grant from the FPRC (Fondazione Piemontese per la ricerca sul Cancro), and by a grant from the Interpolytechnic School of the Polytechnic of Turin.

Contents

Chapter 1

Introduction

Computer Aided Diagnosis (CAD) systems are playing an increasingly important role in medical diagnosis, with a wide variety being proposed within the last decade [1, 2, 3, 4, 5]. The main idea of a CAD systems is to assist radiologists in interpreting medical images by using dedicated computer systems to provide a "second opinions". Studies on CAD systems show that CAD can help to improve diagnostic accuracy of radiologists, lighten the burden of increasing workload, reduce cancer missed due to fatigue, overlooked or data overloaded and improve inter- and intra-reader variability. Two typical and widely used examples of application of CAD in clinical areas are the use of computerized systems in mammography for breast cancer screening and for the early diagnosis of lung cancer with computed tomography (CT) scans. In this work CAD systems have been developed to cope with problems related to early diagnosis of two common tumors: breast cancer which is the second most common malignancy after lung cancer and the most common cancer in women [6, 7], and prostate cancer, the most common malignancy affecting men in the world, representing the third cause of cancer death in industrialized countries [8, 9, 10]. Magnetic Resonance Imaging (MRI) has been chosen as imaging modalities because of its intrinsic high soft tissue resolution. However different MR sequences could be used, according to the aim of the exam and the type of tumor. For breast cancer diagnosis, Dynamic Contrast-Enhanced Magnetic Resonance Imaging (DCE-MRI) is increasingly used as an adjunct to conventional imaging techniques (mammography and sonography) [11]. It relies on signal enhancement after the intravenous injection of a two-compartment gadolinium-based paramagnetic contrast agent: the intensity increases with the concentration of the

contrast agent as it perfuses the tumoral vasculature and diffuses in the extravascular extracellular space. As many image volumes are collected during DCE-MRI exam, the diagnosis is time consuming and could suffer from a high inter- intra observer variability. For this reason a fully automatic CAD system, that aids in the visualization of kinetic information by providing a color map based on the kinetic information, that facilitates analysis through graphical and quantitative representations and provides an index of suspicion, has been developed.

For prostate cancer diagnosis in addition to DCE-MRI imaging, generally, T2-weighted (T2-w) are used to allow a clear visualization of the prostate anatomy; the central lobe can be easily distinguished from the periphery of the gland and the capsule is clearly discernible as a thin dark linear structure. Moreover, Magnetic Resonance Spectroscopy (MRS) extends the possibilities to detect PCa by allowing assessment of molecular constituents of the tissue, especially of choline, which is in higher concentration in tissue with a high cellular metabolism [12]. Finally, Diffusion Weighted Imaging (DWI) can measure the diffusion of water molecules in tissue and hence provide information on the structural organization of the tissue. However, each MR approach alone has some drawbacks, which can be implied from the large range of sensitivity and specificity variations reported in literature, only partially explained by the different diagnostic criteria used in the various study [12, 13]. Recently it has been shown that combining 2 or more MR modalities improves the sensitivity by almost 15%, bringing it up to 83-87% for tumors measuring 5 cm^3 or more [14]. However the more variables are introduced the more difficult is, even for the experienced reader, to integrate all the available information into one reliable final report. Complex problems, such as the one reported in the previous paragraph, have been approached by developing a CAD scheme that aid the radiologist in diagnosing disease.

Chapter 2

Angiogenesis and hemodynamic parameters

2.1 Angiogenesis and cancer

Angiogenesis is a crucial mechanism required for a number of physiological and pathological events. In physiological conditions, angiogenesis is a highly regulated phenomenon, while it is unregulated in pathological conditions, such as psoriasis, diabetic retinopathy and cancer [15]. In physiologic conditions, cells are located within 100 and 200 μm from blood vessels, their source of oxygen, and when a multicellular organism is growing, cells induce angiogenesis and vasculogenesis in order to recruit new blood supply. In the same way, in a pathological condition such as cancer, angiogenesis performs a critical role in the development, survival and proliferation of the tumor. Solid tumors smaller than 1 to 2 cubic millimeters are not vascularized, and to spread, they need to be supplied by blood vessels that bring oxygen and nutrients and remove metabolic wastes. Beyond the critical volume of 2 cubic millimeters, oxygen and nutrients hardly diffuse to the cells in the center of the tumor, causing a state of cellular hypoxia that marks the onset of tumoral angiogenesis.

New blood vessel development is an important process in tumor progression. It favors the transition from hyperplasia to neoplasia, i.e., the passage from a state of cellular multiplication to a state of uncontrolled proliferation characteristic of tumor cells. Neovascularization also influences the dissemination of cancer cells throughout the entire body eventually leading to metastasis formation. The vascularization level of a solid tumor is thought to be an

excellent indicator of its metastatic potential.

2.2 The role of hypoxia

Hypoxia arises early in the process of tumor development because rapidly proliferating tumor cells outgrow the capacity of the host vasculature. Tumors with low oxygenation have a poor prognosis, and strong evidence suggests that this is because of the effects of hypoxia on malignant progression, angiogenesis, metastasis, and therapy resistance. Tumor cells located more than 100 μm away from blood vessels become hypoxic, some clones will survive by activating an angiogenic pathway. If new blood vessels do not form, tumor clones will be confined within 1-1.5 mm diameter. Such clones can remain dormant from months to years before they switch to an angiogenic phenotype. Vascular cooption is confined only in the tumor periphery and gradual tumor expansion causes a progressive central hypoxia. Hypoxia induces the expression of pro-angiogenic factors through hypoxia-inducible factor and, if pro-angiogenic factors are in excess of anti-angiogenic factors, it may lead to the switch to an angiogenic phenotype. The presence of viable hypoxic cells is likely a reflection of the development of hypoxia tolerance resulting from modulation of cell death in the microenvironment. This acquired phenotype has been explained on the basis of clonal selection. The hypoxic microenvironment selects cells capable of surviving in the absence of normal oxygen availability.
However, the persistence and frequency of hypoxia in solid tumors raise a second potential explanation. It has also been suggested that stable micro-regions of hypoxia may play a positive role in tumor growth. Although hypoxia inhibits cell proliferation and eventually causes cell death, hypoxia also provides angiogenic and metastatic signals, thus allowing prolonged survival in the absence of oxygen and generation of a persistent angiogenic signal.

2.3 Mechanisms of new vessels formation

The first interest in angiogenesis related to cancer was in 1968, when it was first highlighted that tumor secretes a diffusible substance that stimulates angiogenesis [16]. Since then, several investigators studied the different pro-angiogenic factors that tumor cells diffuse when the mass reaches the limited size of the early tumor. Pioneering studies performed by Folkman in 1971 proposed an insightful anticancer therapy by starvation of blood supply [17]. Folkman's intuition that tumor growth and metastasis strictly depend on angiogenesis

led to the idea that blocking tumor nourishment could be one of the ways to avoid its spread.
The new vessels formation mechanisms could be distinguished into cellular and molecular.

2.3.1 Cellular mechanisms

Tumors can use four cellular mechanisms to acquire new blood vessels: co-option of pre-existing vessels, angiogenesis, vasculogenesis and intussusception. Tumor cells can grow along existing vessels without evoking an angiogenic response. This process was defined as vessel co-option.
With tumor growth, cancer cells migrate along blood vessels, compressing and destabilizing them, which leads to vessel regression and reduced perfusion. This causes hypoxia and tumor-cell death. Hypoxia and mutations in cancer cells induce the secretion of growth factors that recruit new blood vessels through angiogenesis. Alternatively, in some cases angiogenesis is driven by Vascular Endothelial Growth Factor (VEGF) through the accumulation of a hypoxia-inducible factor in the absence of hypoxia.
Another mechanism by which tumors can acquire new vasculature is adult vasculogenesis (vasculogenesis means the formation of a *de novo* vascular system from endothelial precursor cells). Although this process is incompletely understood and controversial, bone-marrow-derived cells can enter blood circulation and contribute to vessels formation by direct incorporation into functional vasculature.
Finally, a mechanism referred to as intussusception, in which tumor vessels remodel and expand through the insertion of interstitial tissue columns into the lumen of pre-existing vessels, has been seen in murine models of colon and lung cancer metastasis in the brain [18].

2.3.2 Molecular mechanisms

Neovascularization of tumors could be driven by VEGF signalling through its endothelial receptor. During sprouting angiogenesis, vessels initially dilate and become leaky as an initial response to VEGF secreted by cancer or stromal cells. Angiopoietin 2 and certain proteinases mediate the dissolution of the existing basement membrane and interstitial matrix by acting in concert with VEGF. Numerous molecules stimulate endothelial proliferation, migration and assembly into vascular networks. Although VEGF and its receptor are currently the main targets for anti-angiogenic agents developed for cancer therapy,

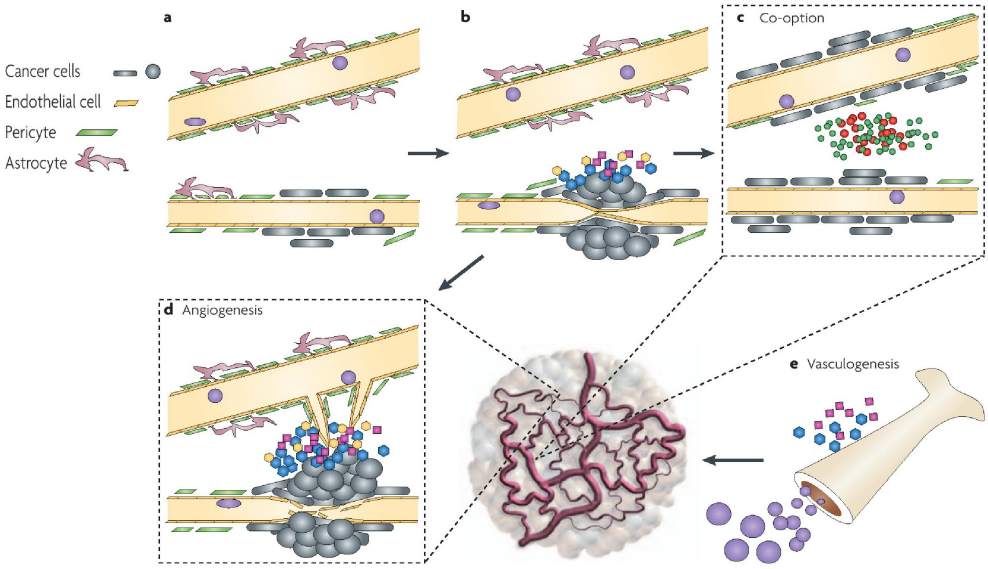

Figure 2.1. *Schematic representation of the mechanisms of vessel formation and the associated molecular components (in the case of brain tumor). Normal blood vessels are typically composed of three cell types: endothelial cells, pericytes and astrocytes (a). Tumors can use four mechanisms to acquire new blood vessels: co-option, angiogenesis, vasculogenesis and intussusception (not shown). When tumor cells colonize the brain, whether from a distant site (metastasis) or locally, they initially infiltrate along the blood vessels and white-matter tracts (factors, cells and receptors that contribute to cell tumor invasion, upregulation of VEGF and increase of the tumor vascular supply are depicted in blue, yellow and purple)(b). The co-option of the normal brain capillaries (c) provides the invading tumor cells with oxygen and nutrients. Angiopoietin 1 (ANG1, in green) maintains vessel integrity. ANG2 (in red) - produced by tumor or endothelial cells - can bind to a receptor on endothelial cells and destabilize the vessels. As the tumor grows, cancer cells migrate along blood vessels, compressing and destabilizing them, leading to vessel regression and reduced perfusion. This causes hypoxia and even tumor cell death. Hypoxia and mutations in cancer cells induce the secretion of growth factors, such as vascular endothelial growth factor (VEGF), that recruit new blood vessels through angiogenesis (d). In addition, platelet-derived growth factor receptor (PDGF) can upregulate VEGF, and exert autocrine effects on endothelial and perivascular cells. These molecules can also induce vasculogenesis, which is another mechanism by which brain tumors may acquire new vasculature (e) [18].*

the number of molecular players involved in tumor blood vessel survival and growth is expanding.

2.4 Angiogenesis and metastases

Angiogenic primary tumors possess a large number of micro-vessels that can stimulate metastatic activity, by carrying the metastasizing cells, increased 100-fold or more [19],

through the blood stream to the other organs. The well-recognized hyper-permeability of tumor vessels, tied to angiogenesis, may also contribute to the transendothelial escape of tumor cells. New, proliferating capillaries have fragmented basement membranes that partially account for this hyperpermeability. Having entered the circulation, the cells must survive the journey, escape immune surveillance, penetrate (or grow from within) the microvessels of the target organ, and again induce angiogenesis in the target in order to grow beyond 2 mm in diameter. It is noteworthy that angiogenesis may not be sufficient, in itself, for metastases to occur. However, the inhibition of angiogenesis prevents the growth of tumor cells at both the primary and secondary sites and thereby can prevent the emergence of metastases. Being a limiting factor for both tumor growth and metastases, it has been assumed that angiogenesis correlates with tumor aggressiveness. Indeed, this assumption has been supported in clinical series investigating a variety of tumor types. Histological assays of angiogenesis based on the Microvascular Density (MVD), the number of endothelial clusters in a high-power microscopic field, in randomly selected human breast cancers showed that MVD correlated with the presence of metastases at time of diagnosis and with decreased patient survival times. MVD is widely accepted as a measurable surrogate of the angiogenesis process.

2.5 Tumor vasculature characterization

In mature (non-growing) capillaries, the vessel wall is composed by an endothelial cell lining, a basement membrane, and a layer of cells called pericytes, which partially surround the endothelium. The pericytes are contained within the same basement membrane as the endothelial cells and occasionally make direct contact with them. Angiogenic factors produced by tumoral cells bind to endothelial cell receptors and initiate the sequence of angiogenesis. When the endothelial cells are stimulated to grow, they secrete proteases, heparanase, and other digestive enzymes that digest the basement membrane surrounding the vessel. Degradation of basement membrane and the extracellular matrix surrounding preexisting capillaries, usually post-capillary venules, is a mechanism allowed by matrix metalloproteinases, a family of metallo-endopeptidase secreted by the tumor cells and the supporting cells. The dissolution of extracellular matrix also allows the release of pro-angiogenic factors from the matrix. The junctions between endothelial cells become altered, cell projections pass through the space created, and the newly formed sprout grows toward the source of the stimulus. Endothelial cells invade the matrix and begin to migrate and

proliferate into the tumor mass. In this location, newly formed endothelial cells organize into hollow tubes (canalization) and create new basement membrane for vascular stability. Fused blood vessels newly established form the blood flow within the tumor. The structure of solid tumors is fundamentally chaotic, in contrast to the elegant and ordered anatomical design of normal tissues and organs [20].
Tumor microcirculation highly differs from that of normal organs in different ways:

- flow characteristics and, sometimes, the blood volume of the microvasculature;
- microvascular permeability;
- for many malignant tumors, in the increased fractional volume of Extracellular Extravascular Space (EES);
- increased interstitial fluid pressure (IFP).

The microvasculature is now known to be aberrant in many malignant tumors and in leukemic bone marrow, because of tumor-derived factors that stimulate the endothelial cells to form new small vessels (angiogenesis) and affect the maturation of these vessels (vasculogenesis). The network of blood vessels in many solid tumors has been shown to deviate markedly from normal hierarchical branching patterns and to contain gaps in which tumor cells lack close contact with perfusing vessels. This phenomenon has been shown in a variety of solid tumors to lead to blood flow that is both spatially and temporally more heterogeneous than the efficient, uniform perfusion of normal organs and tissues. In addition to these abnormalities, tumors often differ from the surrounding organ in the permeability (more properly, permeability $\times$ surface area product) of their capillaries. This altered permeability is important in itself, because it changes the rules governing the transfer of compounds between blood and tumor tissue.
Another abnormality, which specifically affects the trapping and clearance of agents in tumors, is the marked alteration in relative volumes of major tissue compartments (vascular, intracellular, and extravascular-extracellular), with expansion of the EES distribution volume. In cases of tissue injury or pathology, the fractional EES volume, v_e, may increase significantly.
In healthy tissues with normal microvascular perfusion and lymphatic drainage, the IFP is close to zero mm Hg resulting in a positive transcapillary pressure gradient which favors extravasation of the drugs from the capillaries into the interstitial space. In tumors, however,

the increase in the capillary permeability and impaired lymphatic drainage augment IFP to values ranging from 7 mm Hg to as high as 60 mm Hg thereby reducing, and at times even eliminating, the positive transcapillary pressure gradient that cause extravasation of solutes from the capillaries. Furthermore, the interstitial pressure gradient generated by the high IFP in the tumor center as compared to the tumor periphery, causes outward convection and reduced delivery to central regions [21].

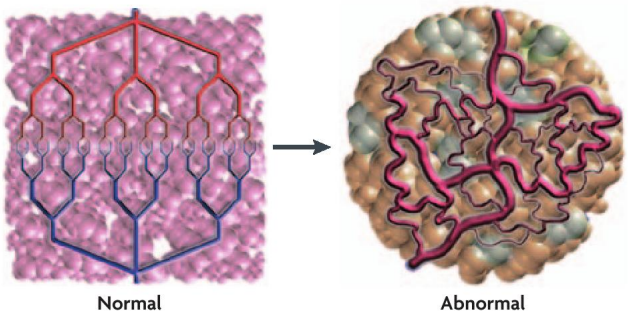

Figure 2.2. *Left: in health, an organized and efficient vascular supply. Right: tumors produce angiogenic factors (various shades of green) that induce an abnormal, inefficient vascular network [18].*

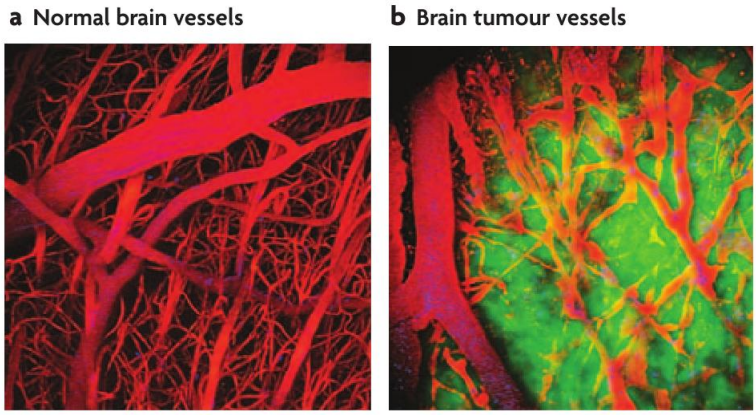

Figure 2.3. *Structural and functional differences between normal and tumor vasculature. a) Photomicrograph of normal vasculature in mouse brain. The vasculature is optimally organized, appropriately connected and shaped to provide nutrients to all parenchymal cells. b) Photomicrograph of vasculature in a glioma xenografted into the brain of an immunodeficient mouse (cancer cells shown in green). This vasculature (vessels shown in red, red blood cells in blue) is disorganized, poorly connected and tortuous, resulting in regions of hypoxia [18].*

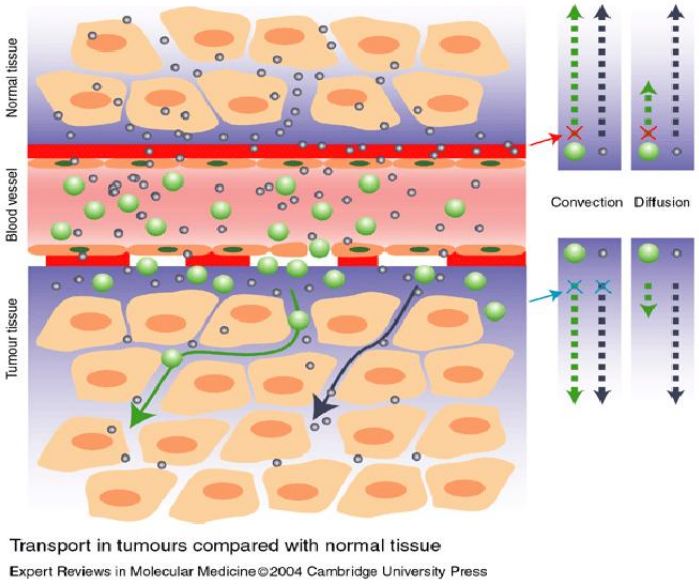

Figure 2.4. *Transport in tumors compared with normal tissue. In normal tissues, the basal lamina and endothelial lining of tumor blood vessels allow extravasation of low-molecular-weight (LMW) molecules (grey) either by convection (transmission of molecules by the movement of the medium) or diffusion (spontaneous movement of molecules by random thermal motion). However, extravasation of high-molecular-weight (HMW) macromolecules and particulates (green) by convection or diffusion is normally prevented in most tissues; this is indicated by the red cross in the right panel. In tumor tissues, the basal lamina and endothelial lining of tumor blood vessels have a leaky morphology, allowing macromolecules and particulates below a "pore "cut-off size to pass through the vessel walls. After extravasation, these macromolecules and carriers become trapped within the tumor because increased interstitial pressure, dysfunctional hydrodynamics and lack of lymphatic vessels reduce fluid drainage and therefore reduce transport by convection (blue crosses in the right panel) rather than by diffusion. Thus, transport beyond the blood vessels and in the tumor interstitium depends largely on diffusion rather than convection. The efficiency of transport by diffusion depends on the hydrodynamic radius and is therefore better for LMW drugs (as indicated by the longer arrow for LMW molecules than HMW in the right panel). Interstitial transport of large entities is further limited by spatial restrictions owing to the density of the extracellular matrix. As a consequence, the tumor acts like a sieve that filters out suitable carriers from the blood stream: this is the so-called enhanced permeability and retention (EPR) effect. The tumor tissue is illustrated here with extra layers of cells, to represent the longer diffusion distances that might need to be traversed. However, even for LMW drugs, distribution throughout the tumor is not necessarily homogeneous and an equilibrium might only be reached after extended periods of drug exposure.*

Chapter 3

Imaging angiogenesis

Imaging of angiogenic vasculature may be a better alternative than measuring microvessel density for assessing therapy because it is non invasive and can be used to assess much larger volumes than biopsy samples. Several imaging methods have been developed to measure blood volume and blood flow, as well as differences in blood vessel permeability, vascular size, and oxygenation. The modalities used to image angiogenic vasculature include x-ray computed tomography (CT), Dynamic Contrast-Enhanced magnetic resonance imaging (DCE-MRI), Diffusion Weighted Magnetic Resonance imaging (DWI-MRI), positron emission tomography (PET), single-photon emission computed tomography (SPECT), ultrasound and and near-infrared optical imaging.
DWI, PET, SPECT and US are steady-state imaging methods: the contrast agent remains confined within the vasculature at a constant concentration throughout the imaging period, while DCE-MRI and dynamic CT are dynamic contrast imaging methods, in which the contrast agent permeate the vascular endothelium and serial images are acquired as the agent enters and leaves the tissue [22].

3.1 Computed Tomography

Dynamic or functional CT could be readily incorporated into routine conventional CT examinations, and the physiological parameters obtained could provide an in vivo marker of angiogenesis in tumors. Using this technique, it is possible to determine absolute values for tissue perfusion, relative blood volume, capillary permeability, and leakage. These parameters correlate with the microscopic changes that occur with tumor angiogenesis,

characterized by an increased number of small blood vessels. These microvessels are too small to be imaged directly, but their increased density leads to in vivo to an increased tumor perfusion and blood volume. Dynamic CT has been used by various investigators to evaluate tumor microvessels density.
Hemodynamic data from CT imaging may be more quantitative than data obtained by MRI because the change in CT image intensity due to the contrast agent is linearly related to the concentration of the contrast agent. In addition, CT has the highest spatial resolution of all imaging modalities and dynamic CT is a simple, widely available and reproducible technique.
However, the sensitivity of CT is limited, and high concentrations of CT contrast agent are required, which can cause toxic effects. This toxicity, together with the relatively high doses of radiation needed (because early clinical studies of antiangiogenic compounds require multiple imaging assessments of the tumor), limits the use of CT for repeated scanning [22].

3.2 Positron Emission Tomography and Single Photon Emission Computed Tomography

Both PET and SPECT imaging are highly quantitative and sensitive to very low concentrations of tracer molecules. PET, which is able to detect picomolar concentrations of tracer, is approximately 10 times more sensitive than SPECT. Both methods are well suited to molecular imaging because of the generally low concentrations of target molecules, as well as for gathering hemodynamic data. However, because the radionuclides used in PET tracers have a very short half-life (2 minutes for ^{15}O, 20 minutes for ^{11}C, and 10 minutes for ^{13}N), PET can only be performed at facilities that have a PET scanner and the necessary cyclotron and chemical laboratory for the preparation of the tracers.
The radionuclides used for SPECT are easier to prepare and somewhat longer lived than those used for PET (6 hours for ^{99m}Tc, 67 hours for ^{111}In, and 13.2 hours for ^{123}I), and SPECT imaging is much more widely available than PET imaging. However, both PET and SPECT images are of lower spatial resolution than magnetic resonance (MR) or CT images [22].

3.3 Ultrasound

Although ultrasound imaging is inexpensive, portable, and widely available, it produces images that have low spatial resolution compared with those produced by MRI or CT. However, very low concentrations of micron-sized gas-filled microbubble contrast agents can be detected by ultrasound, and these are useful agents for angiogenic imaging. Microbubbles are true intravascular contrast agents and are useful for measuring blood volume and flow, although the calculated values obtained by using these agents are not absolute but relative to those in other tissues at similar depths [22].

3.4 Near-infrared spectroscopic

Optical technologies, such as near-infrared spectroscopic diffuse optical tomography and orthogonal polarization spectroscopy, are being developed as alternative modalities for imaging characteristics of angiogenic vasculature. Near-infrared light penetrates tissue sufficiently well to obtain low-resolution images of tissues to a depth of a few centimeters, and the regional concentration of hemoglobin and oxygen saturation can be calculated from the absorption of hemoglobin and deoxyhemoglobin. Optical imaging has the advantage of being relatively inexpensive and portable, but it is not yet widely available [22].

3.5 Dynamic Contrast Enhanced MRI

DCE-MRI is a non invasive technique that yields parameters related to tissue perfusion and permeability, as it is performed during the administration of a paramagnetic contrast agent (CA). The CA is injected as a rapid intravenous bolus and, passing through tissues, it diffuses out of the blood vessels into the intravascular and extracellular fluid space of the body. Tissues taking up such agents will become bright in a T_1-weighted MRI sequence [23] (see Chapter 4), making MRI very sensitive to the concentrations of CA that permeate through capillary walls in angiogenic vasculature, and more reliable than other imaging modalities for measuring parameters that are dependent on permeability. DCE-MRI analysis, however, is time-consuming because multiple volumes are acquired, and suffers from high inter-intra observer variability. A large range of techniques have been applied to the analysis of the signal enhancement curves observed in DCE-MRI. An

approach commonly used in clinical environments is based upon a subjective evaluation of the time-signal intensity curve. Relative changes in semiquantitative parameters, such as the maximum gradient of the signal-intensity-time curve, the maximum increase in signal intensity normalized to baseline signal intensity (enhancement), and the area under the initial part of the curve, can be examined and are indirectly related to changes in the physiologic end points of interest: tissue perfusion, vascular permeability, and vessel surface area. A review about the semiquantitative techniques can be found in Ref. [24], chapt. 1.

One of the attractions of dynamic post contrast imaging is the potential insight it offers into CA distribution kinetics in the tissue [25]. These quantities are generally derived from simple models of the tissue as a compartmentalized system (usually a plasma-interstitial two-compartments model is used), using of kinetic analysis strategies originally developed for use with nuclear medicine tracers.

3.5.1 Semiquantitative and quantitative hemodynamic parameters

Several semiquantitative hemodynamic parameters have been derived from enhancement curves acquired from dynamic contrast imaging. These parameters include the initial and steepest slope of the curve, the time taken to reach 90% of the maximum enhancement (change in intensity), and the maximum enhancement attained after injection of a bolus of contrast agent. Prolonged changes in signals due to extravasation of contrast agent are seen in both MRI and CT imaging, especially in the more permeable angiogenic vasculature of tumors.

Because contrast agents used for CT and MRI pass through the vascular endothelium but not cell membranes, effectively confining them to the plasma and the extracellular extravascular space, a two-compartment model can be used to derive quantitative parameters linked to physiologic characteristics. Several quantitative hemodynamic parameters have been established as standards [26]: K_{trans} (min^{-1}), the rate of contrast agent flux into the extracellular extravascular space within a given volume, or volume transfer constant; v_e, the volume of the extracellular extravascular space; and k_{ep} (min^{-1}), the rate constant for the backflux from the extracellular extravascular space to the vasculature. These parameters are related to each other by the equation:

$$k_{ep} = \frac{K_{trans}}{v_e}. \tag{3.1}$$

K_{trans} has several physiologic interpretations, depending on the balance between capillary permeability and blood flow. In situations in which capillary permeability is very high, the flux of the contrast agent into the extravascular extracellular space is limited by the flow rate. In this case, the kinetics follows the Kety model, and K_{trans} is equal to the blood plasma flow per unit volume of tissue.
When tracer flux is very low and blood flow is high, the blood plasma can be considered as a single pool, in which the concentration of contrast agent does not change substantially during the scan. Any change in signal is, therefore, due to the increase in the concentration of the contrast agent in the extravascular extracellular space. In this case, K_{trans} is equal to the product of the permeability and the surface area of the capillary vascular endothelium (i.e., K_{trans} is equal to the permeability surface area).
If the passage of contrast agent across the vasculature endothelium is limited by blood flow as well as by permeability, then the fractional reduction of capillary blood concentration of the contrast agent as it passes through the tissue must be taken into account. The rate of contrast agent flow out of the capillaries is initially high but decreases over time as the backflow of the contrast agent increases. The rate of clearance of the contrast agent from the system must also be accounted for by using a proportionality constant that links the concentration of the contrast agent to the rate of elimination of the agent from a compartment.
All of these situations fit into a generalized kinetic model, which can be expressed by the equation:

$$\frac{dC_t}{dt} = K_{trans}(\frac{C_p - C_t}{v_e}) = K_{trans}C_p - k_{ep}C_t, \tag{3.2}$$

where C_t is the tracer concentration in tissue, C_p is the tracer concentration in plasma, and t is time (in seconds) [22].

3.6 Diffusion Weighted MRI

A new, emerging functional technique that is now finding a role in cancer imaging is diffusion-weighted MRI (DWI), which produces information about tissue cellularity and the integrity of cellular membranes. DWI provides information on the random (Brownian) motion of water molecules in tissues. The Brownian displacements of millions of water molecules over time are normally distributed with a mean final value of zero for all time periods measured, but with a standard deviation that is proportional to the diffusion coefficient and time measured. This was the basis for Einstein's diffusion equation published in

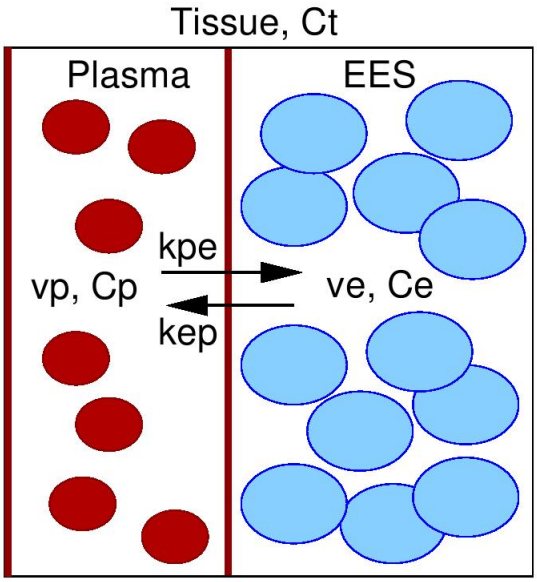

Figure 3.1. *Major compartments and functional variables involved in the distribution of contrast agent in tissues.C_t is the tracer concentration in tissue, C_p is the tracer concentration in the plasma and C_e is the tracer concentration in the EES (respectively in units of mM). v_p is the plasma volume fraction and v_e is the EES fraction in a given volume element of tissue. k_{ep} and k_{pe} are the transport constants related to the leakage space in units of min^{-1}. K_{trans}, defined as $K_{trans} = v_e k_{pe}$, defines, roughly speaking, the amplitude of the initial response (the amount of tracers that enters the EES), while k_{pe} determines the washout rate from EES back into the blood plasma.*

1905, which subsequently helped to earn him the 1921 Physics Nobel Prize. In tissues, DWI probes the movement of water molecules, which occurs largely in the extracellular space. However, the movement of water molecules in the extracellular space is not entirely free, but is modified by interactions with hydrophobic cellular membranes and macromolecules [27]. Hence, diffusion in biological tissue is often referred to as "apparent diffusion". By comparing differences in the apparent diffusion between tissues, tissue characterization becomes possible. For example, a tumor would exhibit more restricted apparent diffusion compared with a cyst because intact cellular membranes in a tumor would hinder the free movement of water molecules.

Chapter 4

MRI sequences

4.1 MRI basics

The basic theoretical elements of a pulsed Nuclear Magnetic Resonance (NMR) experiment, adopting a semi-classical approach, are synthetically introduced.

4.1.1 Spin and magnetic moment

Spin is an intrinsic property of elementary particles that was first observed in electrons. In the 1880's scientists studying the spectrum of light emitted by mercury vapor discovered that light emitted by atoms was not a continuous range of frequencies but rather a discrete one. As instruments measuring the emission spectra of various elements acquired more and more resolving power, it was discovered that the discrete lines in the emission spectra of alkali metals are themselves formed of a set of even finer lines. Just as the initial coarser splitting of the emission spectra was due to the properties of the orbital angular momentum of electrons around the nucleus, two Dutch physicists, Samuel Goudsmith and George Uhlenbeck, attributed this new *fine structure* splitting to an intrinsic angular momentum of the electron. The discovery of the further splitting of each component of the spectra in even finer lines let Wolfgang Pauli propose the existence of the *hyperfine structure* related to nuclear spin. The existence of nuclear spin was first demonstrated in 1922 by the Stern Gerlach experiment, in which a beam of silver atoms were passed through a magnetic field and split into two beams. The two beams represent two states, up $|\uparrow\rangle$ and down $|\downarrow\rangle$, of the silver nuclei. The nuclear spin has an associated intrinsic angular momentum, a vector represented by the symbol $\mathbf{I}$. According to the Heisenberg

uncertainty principle, we can know simultaneously the length of $\mathbf{I}$, together with only one of its components, conventionally assumed as the z-component, I_z :

$$| \mathbf{I} |^2 = \hbar[I(I+1)] \tag{4.1}$$

$$I_z = \hbar m \tag{4.2}$$

where $\hbar$ is Planck's constant divided by 2π, I is the spin quantum number and m is the magnetic quantum number, taking the following set of values: $m = (-I, -I+1, ..., I-1, I)$. In the case of spin $1/2$ nuclei ($I = 1/2$), like the two most abundant silver isotopes or ^{1}H, m can only be equal to -1/2 or $1/2$. Nuclei having a spin angular momentum also have an associated magnetic moment, $\boldsymbol{\mu}$, given by:

$$\boldsymbol{\mu} = \gamma \mathbf{I} \tag{4.3}$$

$$\boldsymbol{\mu_z} = \gamma I_z = \gamma \hbar m \tag{4.4}$$

where Eqn. 4.2 has been exploited and γ is the gyromagnetic ratio (sometimes called the magnetogyric ratio), an intrinsic property of each nucleus.
For a given abundance, nuclei with higher values of γ produce higher sensitivity NMR spectra. In fact, ^{1}H is the most commonly used isotope in magnetic resonance because of his abundance and sensitivity (all over the document we assume to deal with ^{1}H nuclei).

4.1.2 Effect of a static magnetic field

During an NMR experiment, the sample is placed into a static magnetic field, generally referred to as $\boldsymbol{B_0}$. The energy of a magnetic moment immersed in $\boldsymbol{B_0}$ is given by:

$$E = -\boldsymbol{\mu} \cdot \boldsymbol{B_0} \tag{4.5}$$

The z reference axis is conventionally chosen along $\boldsymbol{B_0}$ and the magnitude of the field (coinciding with its z component) is referred to as B_0, i.e.,

$$\boldsymbol{B_0} = B_0 \boldsymbol{k} \tag{4.6}$$

where $\boldsymbol{k}$ is the unit vector along z (in the following, unit vectors along x and y are referred to as $\boldsymbol{i}$ and $\boldsymbol{j}$, respectively). Substituting Eqn.s 4.6 and 4.4 in Eqn. 4.5, the energy of the nuclear spins of the sample can be written as:

$$E = -\mu_z B_0 = -\gamma I_z B_0 \tag{4.7}$$

or

$$E_m = -m\gamma\hbar B_0 \tag{4.8}$$

where E_m is the energy of the spin state with the specific quantum number m.
In absence of field, the $|\uparrow\rangle$ and $|\downarrow\rangle$ states of a spin 1/2 system have the same energy and are equally populated, leading to zero net magnetization. When samples are placed into a magnetic field, a non-zero energy difference between the states (known as the *Zeeman splitting*) develops:

$$\Delta E = E_{|\downarrow\rangle} - E_{|\uparrow\rangle} = \gamma\hbar B_0 \tag{4.9}$$

where Eqn. 4.8 has been used. A *small* excess of nuclei fall into the lower energy $|\uparrow\rangle$ state, according to the Boltzmann distribution:

$$\frac{N_{|\uparrow\rangle}}{N_{|\downarrow\rangle}} = exp(\frac{\Delta E}{k_B T}) \tag{4.10}$$

where k_B is the Boltzmann's constant, T is the absolute temperature and $N_{|\uparrow\rangle}/N_{|\downarrow\rangle}$ is the ratio between the populations of the states. The difference in population between the spin states, give rise to a non-null macroscopic magnetization vector, $\boldsymbol{M}$, defined as the vector sum of all the microscopic magnetic moments in the specimen:

$$\boldsymbol{M} = \sum_i \boldsymbol{\mu_i} \tag{4.11}$$

where $\boldsymbol{\mu_i}$ is the magnetic moment of the i-th nuclear spin, and the sum is performed over all the spins in the sample.
The fractional population difference at equilibrium in a typical clinical setup (protons in a magnetic field of 1.5 T at 300 K) is:

$$\frac{N_{|\uparrow\rangle} - N_{|\downarrow\rangle}}{N_{|\uparrow\rangle} + N_{|\downarrow\rangle}} = 5 \times 10^{-6}. \tag{4.12}$$

This excess of spins accounts for the entire net magnetization measured in the NMR experiment. This explains the relatively low sensitivity of MRI (only five protons in a million can be measured) compared with imaging techniques involving radioactive isotopes, where any single decay can be detected.

4.1.3 Magnetization and radio frequency pulses

From Planck's law, $\Delta E = \hbar\nu$, and Eqn. 4.9, the frequency ν_0 of an NMR transition in a magnetic field B_0 is:

$$\nu_0 = \frac{\Delta E}{h} = \frac{\gamma B_0}{2\pi} \tag{4.13}$$

or, given $\nu_0 = \omega_0/2\pi$,

$$\omega_0 = \gamma B_0 \tag{4.14}$$

where ω_0 is known as the *Larmor precession frequency.*
NMR transitions are induced by linearly polarized radio frequencies (rf) pulses, with the magnetic field oscillating in the plane perpendicular to $\boldsymbol{B_0}$. It is conventional to represent the oscillatory field as a sum of two circularly polarized components, each of amplitude B_1, counter-rotating in the xy-plane at angular velocity ω. One of these components will rotate in the same sense as the nuclear spin precession:

$$\boldsymbol{B_1}(t) = B_1[cos(\omega t)\boldsymbol{i} - sin(\omega t)\boldsymbol{j}] \tag{4.15}$$

and it will be responsible for the resonance phenomenon when ω equals ω_0. The counterrotating component can be ignored provided $B_1 \ll B_0$, which is invariably the case in NMR experiments.
The necessity of using circularly polarized rf comes from quantum mechanical selection rules, dictating that NMR signals can only arise when the Δm of the corresponding transition equals -1 [28].

4.1.4 Variable magnetic fields

Let us consider the effect on the bulk magnetization of a generic variable field $B(t)$. According to classical mechanics:

$$\frac{d\boldsymbol{J}(t)}{dt} = \boldsymbol{M}(t) \times \boldsymbol{B}(t) \tag{4.16}$$

where $\boldsymbol{J}$ is the bulk spin angular momentum, defined, analogously to Eqn. 4.11, as:

$$\boldsymbol{J} = \sum_i \boldsymbol{I_i}. \tag{4.17}$$

Substituting Eqn.s 4.11, 4.17 and 4.3 in Eqn.4.16, and multiplying each side by γ, we obtain:

$$\frac{d\boldsymbol{M}(t)}{dt} = \gamma \boldsymbol{M}(t) \times \boldsymbol{B}(t) \tag{4.18}$$

which is the equation of the motion of $\boldsymbol{M}$ in the laboratory reference frame.
In our case, $\boldsymbol{B}$ is the sum of the static field $\boldsymbol{B_0}$ and the rotating rf field $\boldsymbol{B_1}$:

$$\boldsymbol{B}(t) = \boldsymbol{B_0} + \boldsymbol{B_1}(t) \tag{4.19}$$

so, it is convenient to introduce a new reference frame, (x', y', z'), with $z' \equiv z$ and the $x'y'$-plane rotating around z at a velocity ω. The transformation rules can be succinctly written in complex notation, as:

$$M_{x'y'} = M_{xy}e^{i\omega t} \tag{4.20}$$

$$M_{z'} = M_z \tag{4.21}$$

where the magnetization vector is chosen as an example, and:

$$M_{xy} = M_x + iM_y \tag{4.22}$$

$$M_{x'y'} = M_{x'} + iM_{y'}. \tag{4.23}$$

Rewriting Eqn. 4.15 in complex notation:

$$B_{1xy}(t) = B_1 e^{-i\omega t} \tag{4.24}$$

and applying the transformation of Eqn. 4.20, it is clear that in the rotating frame, $\boldsymbol{B_1}$ is a static field lying in the $x'y'$-plane (see Eqn. 4.15). In fact, the x'-direction is chosen along $\boldsymbol{B_1}$. In the rotating frame, Eqn. 4.18 becomes (see [29]):

$$\frac{d\boldsymbol{M}}{dt} = \gamma \boldsymbol{M} \times \boldsymbol{B}_{eff} \tag{4.25}$$

where $\boldsymbol{B}_{eff}$ is called *effective field*:

$$\boldsymbol{B}_{eff} = \boldsymbol{B} + \frac{\boldsymbol{\omega}}{\gamma} \tag{4.26}$$

and:

$$\boldsymbol{\omega} = -\omega \boldsymbol{k} \tag{4.27}$$

where $\boldsymbol{k}$ coincides with $\boldsymbol{k}'$. Eqn. 4.25 shows that the ordinary equations of motion applicable in the laboratory system are valid in the rotating frame as well, provided that $\boldsymbol{B}_{eff}$ is used instead of $\boldsymbol{B}$. In other words, the magnetization will precess about $\boldsymbol{B}_{eff}$.

4.1.5 Effect of the rf pulse

Recalling Eqn. 4.19, $\boldsymbol{B}_{eff}$ can be written as:

$$\boldsymbol{B}_{eff} = \boldsymbol{B_0} + \boldsymbol{B_1} + \frac{\boldsymbol{\omega}}{\gamma} = (B_0 - \frac{\omega}{\gamma})\boldsymbol{k} + \boldsymbol{B_1} \tag{4.28}$$

where Eqn.s 4.6 and 4.27 have been used. Under resonance conditions ($\omega = \omega_0$), holds:

$$\boldsymbol{B}_{eff} = (\frac{\omega_0}{\gamma} - \frac{\omega}{\gamma})\boldsymbol{k} + \boldsymbol{B_1} \tag{4.29}$$

where Eqn. 4.14 has been used. Note that, the longitudinal component of the effective fields gets deleted. According to Eqn. 4.25 and last findings, when a rf pulse of length τ is applied to the sample, $\boldsymbol{M}$ precesses about $\boldsymbol{B_1}$ (i.e., x') with the velocity:

$$\omega_1 = \gamma B_1. \tag{4.30}$$

Therefore, at the end of the pulse, the magnetization will form the angle:

$$\alpha = \omega_1 \tau \tag{4.31}$$

with the z-axis (see Fig. 4.1b). α is called *Flip Angle* (FA) and it is one of the most important parameters characterizing an rf pulse in NMR. A 90°-pulse flips the magnetization down to the y'-axis and is called *saturation* pulse, since it equals the populations of the spin states. In the laboratory frame, the $\boldsymbol{M}$ precession around $\boldsymbol{B_0}$ has to be added. The resulting magnetization motion is a spiral trajectory like the one shown in Fig. 4.1a.

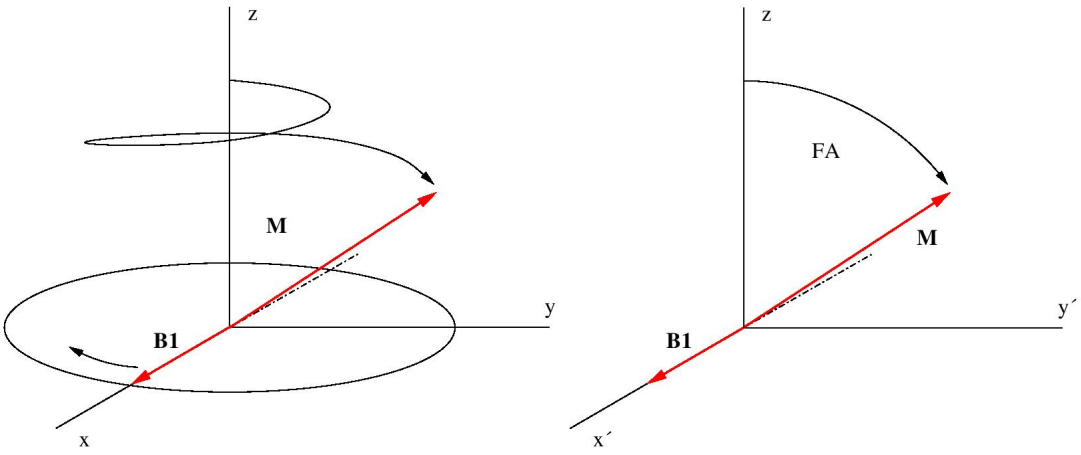

(a) Laboratory frame (b) Rotating frame

Figure 4.1. *Evolution of the magnetization vector in the presence of an on-resonance rf pulse. In the laboratory frame (a), the magnetization simultaneously precesses about $\boldsymbol{M_0}$ at ω_0 and about $\boldsymbol{B_1}$ at ω_1. In the rotating frame (b), the effective longitudinal field is zero and only the precession about B_1 is apparent.*

4.1.6 After the pulse

In 1946 Felix Bloch formulated a set of equations describing the behavior of a nuclear spin in a magnetic field, under the influence of rf pulses. He modified Eqn. 4.25 to account for the observation that nuclear spins relax to equilibrium values, following the application of rf pulses. Bloch assumed they relax, following first order kinetics, along the z-axis and in the xy-plane at different rates, designated $1/T_1$ and $1/T_2$, respectively. The relaxation processes regulated by the *characteristic times* T_1 and T_2 are called longitudinal (or *spin-lattice*) and transverse (or *spin-spin*) relaxation, respectively (see section 4.1.8).
Adding relaxations, Eqn. 4.25 becomes:

$$\frac{d\boldsymbol{M}}{dt} = \gamma \boldsymbol{M} \times \boldsymbol{B}_{eff} - \frac{M_{x'}\boldsymbol{i'} + M_{y'}\boldsymbol{j'}}{T_2} - \frac{(M_{z'} - M_0)\boldsymbol{k'}}{T_1} \tag{4.32}$$

where M_0 is the thermal equilibrium value of M_z, that is, at equilibrium:

$$\boldsymbol{M} = M_0 \boldsymbol{k'}. \tag{4.33}$$

During the application of the rf pulse, the relaxation influence in the magnetization motion can be neglected, since the length of the pulse is always much shorter than T_1 and T_2. After the end of the pulse $\boldsymbol{B_1}$=0, so in the Larmor-rotating frame, also $\boldsymbol{B}_{eff}$ is null (see Eqn. 4.29), and the Bloch equation simplifies as:

$$\frac{dM_{x'y'}}{dt} = -\frac{M_{x'y'}}{T_2} \tag{4.34}$$

$$\frac{dM_{z'}}{dt} = -\frac{(M_{z'} - M_0)}{T_1} \tag{4.35}$$

where $M_{x'y'}$ and $M_{z'}$ are the transverse and longitudinal magnetization components, respectively. One can verify that the solutions to Eqn.s 4.34 and 4.35 are:

$$M_{x'y'}(t) = M_{x'y'}(0)e^{-t/T_2} \tag{4.36}$$

$$M_{z'}(t) = M_{z'}(0)e^{-t/T_1} + M_0(1 - e^{-t/T_1}) \tag{4.37}$$

where $t = 0$ means immediately after the end of the pulse. If the system was at thermal equilibrium before the pulse, then:

$$M_{x'y'}(0) = M_0 \sin\alpha \tag{4.38}$$

$$M_{z'}(0) = M_0 \cos\alpha \tag{4.39}$$

where α is the pulse flip angle.
The combined effect of free precession and relaxation can be seen by putting the magnetization vector back to the laboratory frame. Specifically, applying the transformation rules in Eqn.s 4.20 and 4.21 to Eqn.s 4.36 and 4.37, respectively, we obtain:

$$M_{xy}(t) = M_{xy}(0)e^{-t/T_2}e^{-i\omega_0 t} \tag{4.40}$$

$$M_z(t) = M_z(0)e^{-t/T_1} + M_0(1 - e^{-t/T_1}) \tag{4.41}$$

where $M_{xy}(0)$ is the transverse magnetization observed in the laboratory frame, immediately after the rf pulse. Eqn.s 4.40 and 4.41 describe the magnetization precessing in the xy-plane of the laboratory frame at the Larmor frequency, while it is relaxing along the z-axis at a rate $1/T_1$ and relaxing in the xy-plane at a rate $1/T_2$.

4.1.7 Signal from precessing magnetization

According to Faraday induction law and the principle of reciprocity, the signal in a NMR experiment is detected as the electromagnetic force (emf) induced by the precessing magnetization in a receiver coil (a conducting loop) [29]:

$$emf = -\frac{\partial \Phi_M(t)}{\partial t} = -\frac{\partial}{\partial t}\int_{sample} \boldsymbol{M}(\boldsymbol{r},t)\cdot\boldsymbol{B}_{rec}(\boldsymbol{r})d\boldsymbol{r} \tag{4.42}$$

where Φ_M is the time-varying magnetic flux through the coil and $\boldsymbol{B}_{rec}$ is the magnetic field produced at location $\boldsymbol{r}$ by a hypothetical unit current flowing in the coil. The coil is placed around the sample with its symmetry axis perpendicular to the polarizing field, so only the transverse magnetization can induce some signal. A common configuration is to use the same rf coil to transmit $\boldsymbol{B}_1$ fields to the object and to receive signal from the magnetization.
Let us analyze the signal generated by a 90°-pulse on a system at thermal equilibrium. According to Eqn.s 4.38 and 4.40, the transverse magnetization component in the laboratory frame at time t, following the pulse, is:

$$M_{xy}(t) = M_0 e^{-t/T_2}e^{-i\omega_0 t} \tag{4.43}$$

where the pulse duration τ is assumed to be negligible with respect to the Larmor precession time. This assumption allows to forget the phase shift accumulated during τ between $M_{x'y'}(0)$ and $M_{xy}(0)$. If the receiver coil has a homogeneous reception field $\boldsymbol{B}_{rec}$ over the

sample, it can be shown that the signal takes the following expression:

$$S(t) = S(0)e^{-t/T_2}e^{-i\omega_0 t} \tag{4.44}$$

where $S(0)$ is the signal amplitude immediately following the pulse, a number which depends on the hardware configuration and which is proportional to $M(0)$. The primary NMR signal is measured in the time domain as an oscillating, decaying emf induced by the magnetization in free precession. It is therefore known as the *Free Induction Decay* (FID). An example of FID is represented in Fig. 4.2.

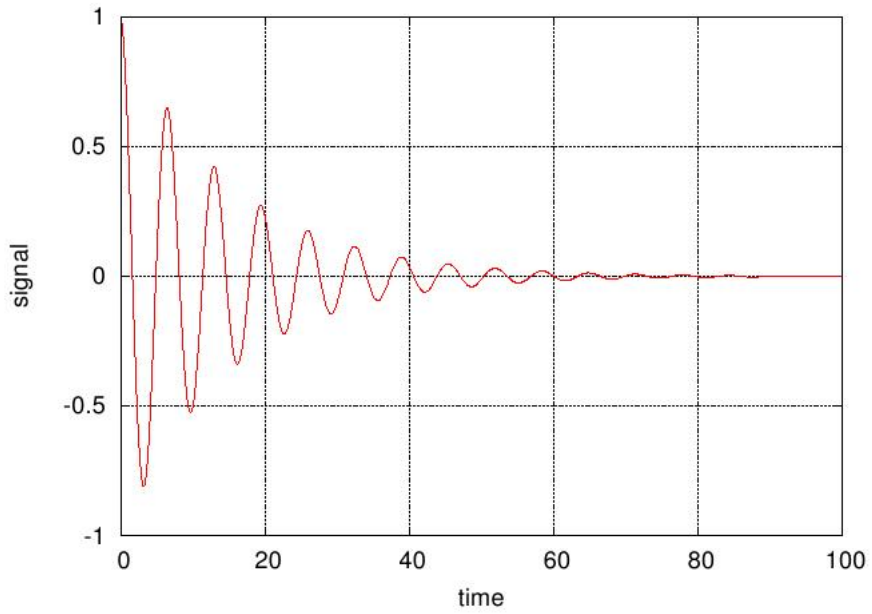

Figure 4.2. *Typical example of FID signal. Signal and time are expressed in arbitrary units.*

4.1.8 Relaxation mechanisms

As already discussed, the equilibrium net magnetization along $\boldsymbol{B_0}$ can be perturbed by an rf pulse with a frequency exactly matched to the energy difference between the two spin population states. Once the perturbing field is turned off, the nuclear spins start to relax, due to different relaxation mechanisms, to claim back their equilibrium state.
Adopting a phenomenological approach, we observe that spins relax along the z-axis and in the xy-plane at different rates, designated $1/T_1$ and $1/T_2$, respectively. However, the

description of the mechanisms underlying spin-lattice and spin-spin relaxations needs a microscopic approach.

Spin-lattice relaxation

The mechanism responsible for the returning of the longitudinal component of the magnetization to its equilibrium value is known as spin-lattice relaxation. The spin-lattice relaxation time T_1 manages the energy exchange between the spin system and the lattice. In a non-equilibrium situation due to different populations in the two energy states, the transition to the equilibrium state is accomplished by energy transfer from the spin system to the lattice. Because the non-equilibrium state is a thermodynamic in stable state, T_1 is also a measure of the thermodynamic coupling. A spin in the high-energy state can make a transition to the low-energy state either via spontaneous emission or stimulated emission. However, since the probability of spontaneous emission depends on the third power of the frequency, the probability for spontaneous emission is too low to be significant at radio frequencies. As a result, all NMR transitions are stimulated.
In order to undergo a transition, the spin needs stimulation in form of a fluctuating magnetic field with components at the Larmor frequency in the xy-plane. Such a field is produced by the random motions of the molecules in the surrounding medium. As the molecules move around, they carry the nuclear magnetic moments with them generating a *magnetic noise* at the site of any nucleus. The broad frequency range of this noise will cover the Larmor frequency of the nuclei, stimulating a transition back to the lower energy level, that is an energy exchange between the spin system and the lattice.
Several processes, commonly referred to as T_1*-processes*, can generate magnetic noise, namely magnetic dipole-dipole, electric quadrupole, chemical shift anisotropy, scalar coupling and spin rotation interactions. All mechanisms contribute to the observable T_1 according to the following [30]:

$$\frac{1}{T_1} = \sum_m \frac{1}{T_{1,m}} \tag{4.45}$$

where $T_{1,m}$ is the time constant of mechanism m.

Spin-spin relaxation

The magnetization present in the transverse plane after an rf excitation decay toward zero due to a process known as spin-spin relaxation. Immediately after a 90° rf pulse, the

individual nuclear magnetic moments have the maximum phase coherence. This phase coherence would be maintained if all the protons experienced exactly the same local magnetic field. However, this is not the case in real systems, where the local field experienced by each proton is affected by its surroundings. Therefore, magnetic moments will gradually lose their phase coherence (*dephasing*), leading to the disappearance of a detectable net transverse magnetization.

The two main sources of dephasing are: *extrinsic* magnetic inhomogeneities (T_2-relaxation processes) and *intrinsic* magnetic inhomogeneities (T_2-relaxation processes). Extrinsic inhomogeneities arise from instrumental imperfection of the polarizing field, application of magnetic field gradients (see section 4.2) and magnetic susceptibility differences within the sample. At the interfaces (e.g., air/water interface) where there is a sudden change in magnetic susceptibility ($\Delta\chi$), protons experience a significant change in the local magnetic field over a short distance [31].

The slight difference in B_0 from point to point will result in a frequency distribution:

$$\Delta\omega = \gamma \Delta B_0 \tag{4.46}$$

and hence in a dephasing.

Extrinsic magnetic inhomogeneities are time invariant and their dephasing effect can be reversed by an additional 180° rf pulse (see section 4.3). On the other hand, intrinsic magnetic inhomogeneities are due to the magnetic noise around the spins and cannot be reversed by 180° pulses.

Extrinsic and intrinsic processes contribute to the transverse relaxation as follows:

$$\frac{1}{T_2^*} = \frac{1}{T_2} + \frac{1}{T_2'} \tag{4.47}$$

where T_2^* is the *observed* or *effective* spin-spin relaxation time ($T_2^* < T_2$).

4.1.9 From spectra to images

Effect of magnetic field gradients

In conventional NMR spectroscopy the spectrum of nuclear precession frequencies gives information about the chemical environment of the spins and it is very important that the polarizing field, B_0, varies as little as possible across the sample.

In NMR the resonance frequency varies between 10 and 100 MHz, depending on the magnetic field applied. The associated wavelength is bigger than human body dimensions and

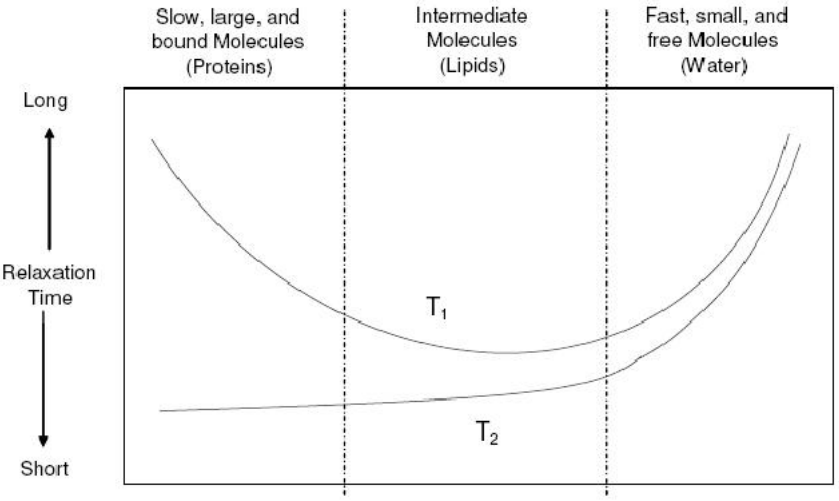

Figure 4.3. *T_1 and T_2 versus the molecular motion correlation time τ_c. For rotational motion, τ_c is defined as the time the molecule takes to rotate $\pi/2$ radians, while for translational motion τ_c is the average time between molecular collisions. Molecules in liquids have shorter correlation time than molecules bound to a gel or solid matrix.*

it would not be possible to have a resolution power in the range of mm. The idea of Lauterbur to overcome this problem became the key element of an NMR imaging experiment: the presence of gradients varying linearly the field magnitude across the sample, in order to encode the signal of the spins in space.
In two-dimensional (2D) *Fourier Imaging*, one of the most common imaging technique, the spatially localized magnetic resonance information is obtained through the sequential application of three perpendicular pulsed gradients. Each gradient has a different effect, generally referred to as *slice selection*, *phase encoding* and *frequency encoding*.

Slice selection

Slice selection (or selective excitation) is performed by applying a magnetic field gradient during the rf excitation. Often, the direction of the slice selective gradient is chosen along z (the direction of the static magnetic field, B_0) so, for the sake of simplicity, here we will consider only this case, referring to the *slice selection gradient* as G_z, where:

$$G_z = \frac{\partial B_0}{\partial z} \tag{4.48}$$

Analogous definitions take G_x and G_y.
It is worth stressing that, in any case, only the magnitude of the static field is influenced

by the gradients, whereas the direction of $\boldsymbol{B_0}$ remains constant all over the sample.
In presence of G_z the Larmor frequency becomes a function of z, i.e.,

$$\omega = -\gamma(B_0 + G_z z). \tag{4.49}$$

By exciting the sample with an rf of ω_{rf}, only the spins about

$$z = -\frac{\omega_{\text{rf}} + \gamma B_0}{\gamma G_z} \tag{4.50}$$

will be rotated into the xy-plane, contributing to the final signal, thus selecting a plane of the sample perpendicular to B.
For a rectangular rf pulse of duration τ, there will be a spread of frequencies described by the *Fourier Transform* (FT) of a rectangular window function, i.e., a sinc function centered on ω_{rf}, with a bandwidth proportional to $1/\tau$.
The approximate width of the slice selected will thus be:

$$\Delta z \sim \frac{1}{\gamma G_z \tau}. \tag{4.51}$$

The duration of the rf pulse is the main parameter controlling the slice thickness. A slice profile that is a sinc function however is not ideal, as it produces substantial excitation in the lobes away from the selected slice. Improved slice profiles can be obtained by using excitation pulses of different shapes, like sinc or Gaussian.

Frequency and phase encoding

Once the slice has been excited, the frequency and phase of the precessing macroscopic magnetic moment can be made a function of position within the slice. In the simplest case, if a magnetic field gradient in the x-direction, G_x, is switched on during the signal acquisition, then the Larmor frequency becomes a function of x (*frequency encoding*):

$$\omega(x) = -\gamma(B_0 + G_x x) \tag{4.52}$$

and the slice is cut into *strips* of constant Larmor frequency. Ignoring the T_2 decay, an area $dxdy$ in the selected slice gives a contribute $dS(t)$ to the total signal:

$$dS(t) = \rho(x, y) e^{-i\gamma(B_0 + G_x x)t} dxdy \tag{4.53}$$

where ρ is the proton density function and the time origin is set at the G_x activation (i.e., at the beginning of the signal acquisition).

Demodulating the signal, to remove the carrier frequency γB_0, and integrating over the slice, we obtain the following expression for the total signal:

$$S(t) = \int \underbrace{\int \rho(x,y)dy}_{\rho_{y-projection}} e^{-i\gamma G_x x t} dx \tag{4.54}$$

where we recognize the ρ projection along the y-axis.
The ρ projection along y can be resolved applying, for a certain amount of time, a gradient along y, immediately following selective excitation and just before signal acquisition. By briefly turning on the G_y field gradient, the precessional phases of the rotating macroscopic magnetization can be manipulated as follows. G_y induces a variation of the Larmor frequency along the y-direction, according to:

$$\omega(y) = -\gamma(B_0 + G_y y). \tag{4.55}$$

If G_y is now turned off after a time τ_y, $\boldsymbol{M}$ returns to the constant frequency ω_0, but having accumulated a phase shift, ϕ, as a function of y (*phase encoding*), i.e.,

$$\phi(y) = \gamma G_y y \tau_y. \tag{4.56}$$

If the frequency encoding gradient is now turned on and the signal acquired, then the FID is a function of t and τ_y i.e.,

$$\begin{aligned} S(t,\tau_y) &= \int\int \rho(x,y) e^{-i(\gamma G_x x t + \phi(y))} dxdy \\ &= \int\int \rho(x,y) e^{-i(\gamma G_x x t + G_y y \tau_y)} dxdy. \end{aligned} \tag{4.57}$$

Using G_x and G_y we have indexed each nutated macroscopic magnetic moment in the selected slice, that is each (x, y) position, with an unique combination of *Larmor frequency* and *Larmor phase*, (ω, ϕ).

k-space and pulse sequences

Eqn. 4.57 can be conveniently rewritten as:

$$S(k_x, k_y) = \int\int \rho(x,y) e^{-i(k_x x + k_y y)} dxdy \tag{4.58}$$

where:

$$k_x = \gamma G_x t \tag{4.59}$$

$$k_y = \gamma G_y \tau_y \tag{4.60}$$

The plane defined by the $\boldsymbol{k} = (k_x, k_y)$ points is called k-space, and it plays an important role in the interpretation of MRI experiments.
In Eqn. 4.58 we can note that $S(k_x, k_y)$ and $\rho(x, y)$ are *FT-pairs*.
The proton density over the slice (i.e., the image, in absence of relaxations) can thus be obtained by taking the inverse 2D FT of the demodulated FID over the k-space. k_y is varied by stepping through different values of G_y, whereas k_x is sampled by holding on the frequency encoding gradient while sampling the signal discretely.
The acquisition of each line of the k-space (i.e., $\{\forall(k_x, k_y) : k_y = \text{const}\}$) implies at least an rf pulse (the excitation), a series of gradient pulses, and the signal acquisition.
The time course between two subsequent excitation rf pulses is called *repetition time*, and referred to as T_R. The complex sequence of time delays, gradient and rf pulses is known as *pulse sequence*. The total acquisition time of a slice, T_{acq} is thus given by:

$$T_{acq} = N_y T_R \tag{4.61}$$

where N_y is the number of k_y steps.
From the properties of the FT, we know that the signal acquired at each k-space location contains information about the whole image, but the type of information varies across the k-space. Most of the contrast of the final image is encoded at the center of the k-space (small k_x and k_y), while its peripheral part accounts mainly for the high frequency contributes to the image, that is resolution of details and noise.
The trajectory of the vector $\boldsymbol{k}$ during the pulse sequence can be written as:

$$\boldsymbol{k}(t) = \gamma \int_0^t \boldsymbol{G}(t')dt' \tag{4.62}$$

where the time origin is now at the beginning of the sequence and $\boldsymbol{G}(t)$ is the general function describing orientation, shape and duration of the magnetic field gradients applied during the MRI experiment.
The $\boldsymbol{k}(t)$ formalism is of great help in interpreting complex pulse sequences.

Steady state and T_1-weighted images

In order to let the longitudinal magnetization recover the thermal equilibrium before the acquisition of the next line (and therefore obtaining the maximum signal) T_R should be at least 5-7 times T_1. This is actually impractical for in-vivo imaging, due to the resulting

too long acquisition time (Eqn. 4.61). In fact, T_R is always set $\lesssim T_1$.
After a few pulses, the recovered value of M_z reaches a *steady state*, depending upon the T_1 of the sample, but always lower than M_0.
The longitudinal magnetization after the n-th T_R interval is given by:

$$\begin{aligned} M_z^{(n)} &= M_z^{(n-1)} \cos\alpha + (1-E)(M_0 - M_z^{(n-1)} \cos\alpha) \\ &= (1-E)M_0 + KM_z^{(n-1)} \end{aligned} \tag{4.63}$$

where α is the FA of the excitation pulse (Eqn. 4.31), and we define:

$$E = e^{-T_R/T_1} \tag{4.64}$$

$$K = E\cos\alpha. \tag{4.65}$$

Writing Eqn. 4.63 as a sequence, we have:

$$\begin{aligned} M_z^{(n)} &= (1-E)M_0(1 + K + K^2 + \cdots + K^n) + K^n e^{-T_R/T_1} M_0 \\ &= (1-E)M_0 \frac{1-K^{(n+1)}}{1-K} + K^n E M_0 \end{aligned} \tag{4.66}$$

and, since $K < 1$, for $n \to \infty$, the steady state value is:

$$M_z^{(n\to\infty)} = M_z^{\text{steady}} = \frac{(1-E)M_0}{(1-K)} \tag{4.67}$$

A short T_R, together with reducing T_{acq}, can thus be used to induce a contrast between two regions of the sample having the same proton density, but different (T_1-*weighted image*).

Multi-slice 2D imaging

The coverage of a 3D volume is accomplished through the multi-slice approach, by applying a sequence of rf pulses, exciting different slices, within a single T_R. During each T_R, one k-space line is acquired for all the slices, thus keeping the same T_{acq} of the single-slice acquisition. On the other hand, TR has to be set long enough to allow for the pulse sequence of each slice being executed.
Because of imperfect rf profiles, the immediate neighborhood of an excited slice is also partly excited (*slice cross-talk effect*). In multi-slice imaging, this region cannot be included in the following slice since the spins do not have time to recover toward equilibrium. To overcome the problem, it is common either to leave a gap between slices, or to excite the odd numbered slices first and the even numbered ones afterwards (*interleaved acquisition*).

3D volume imaging

As an alternative to the 2D multi-slice approach for imaging 3D volumes, the 2D coverage of k-space described in section 4.1.9 can be generalized to 3D.
The excitation pulse is used to select a thick *slab* of the sample, then the 3D k-space is discretely sampled in both directions, k_y and k_z, through phase encoding. The read sampling along the x-direction is carried out, as in 2D, with measurements at finite time steps Δt during the continuous application of a gradient G_x. The associated step in the k_x direction is:

$$\Delta k_x = \gamma G_x \Delta t. \tag{4.68}$$

The (k_x, k_y) position of each acquisition line is determined by applying the orthogonal gradients G_y and G_z, for the τ_y and τ_z time intervals, respectively. The corresponding steps in k-space are:

$$\Delta k_y = \gamma \Delta G_y \tau_y \tag{4.69}$$

$$\Delta k_z = \gamma \Delta G_z \tau_z \tag{4.70}$$

where ΔG_y is the difference in G_y intensity between two consecutive read lines, and analogously for ΔG_z.
Under 3D imaging conditions, the signal from a single rf excitation of the whole sample can be written as a 3D FT of the proton density:

$$S(\boldsymbol{k}) = \int \rho(\boldsymbol{r}) e^{-i\boldsymbol{k}\cdot\boldsymbol{r}} d\boldsymbol{r}. \tag{4.71}$$

3D vs 2D

3D imaging presents several advantages in comparison with multi-slice imaging:

1. The ability to change the number of the N_z phase encoding steps over the excited slab of thickness TH, gives the control over the size of the partition thickness $\Delta z = \mathrm{TH}/N_z$ without any limitation on the rf amplitude or duration. In general, higher z resolutions are obtainable.

2. The Signal-to-Noise Ratio (SNR) can be enhanced, thanks to the higher flexibility in setting the pulse program parameters available in 3D imaging, but achieving this may come at the expense of increased imaging time [31].

3. Consecutive slices may be adjacent without cross-talk effects.

4. Shorter T_R are usable if necessary, since only one k-space line has to be acquired each repetition.

On the other hand, the total acquisition time for 3D imaging is given by:

$$T_{acq} = N_y N_z T_R \tag{4.72}$$

where N_y and N_z denote the number of phase encoding steps along y and z. As evident from the Eqn.s 4.61 and 4.72 the 2D imaging lasts much shorter time with respect to the 3D imaging. An immediate consequence is the capability of acquiring more 2D than 3D images within the same time, thus allowing a higher temporal resolution, in dynamic studies. A more indirect effect is due to the capability (but also the necessity, see section 4.1.9) of setting longer T_R, given a certain T_{acq}, in multi-slice imaging. A longer T_R implies a higher steady-state value of the longitudinal magnetization, thus giving a higher SNR.

4.2 Gradient Recalled Echo

In the imaging sequences described so far, we always assumed to acquire FID signals (see section 4.1.7), however this is almost never done in practice. In fact, after excitation and phase encoding, the echo of the original FID is recalled by means of the read gradient, and measured (*Gradient Recalled Echo*, GRE). The reason for this is best explained by inspecting the meaning of FID and echo acquisitions in the k-space formalism.
Let us watch at the FID at first, and let us consider Eqn. 4.59. Up to the acquisition start G_x is turned off, so $k_x = 0$, while k_y is determined by the phase-encoding (Eqn. 4.60). In other words, as the acquisition starts the $\boldsymbol{k}$ point is located somewhere on the k_y axis.
When G_x is turned on, k_x increases linearly in time, that is $\boldsymbol{k}$ travels along a line parallel to the k_x axis in the positive direction, stepping according to the sampling frequency (Eqn. 4.68).
The $\boldsymbol{k}$ trajectory is shown with blue arrows in Fig.4.4a, note that only the $k_x > 0$ half of the k-space is sampled.
In the echo scheme, a negative read gradient ($G_x = -G_-$ where $G_- > 0$) is applied in the time interval τ_-, before starting the acquisition. As a consequence, $\boldsymbol{k}$ moves in the negative k_x direction up to $k_x = -\gamma G_- \tau_-$, and spins along x dephase according to:

$$\phi_G(x) = -\gamma G_x x \tau_- = +\gamma G_- x \tau_- \tag{4.73}$$

canceling the signal.

G_x is then switched to the positive value G_+ and the acquisition started.

$\boldsymbol{k}$ reverts its motion, traveling in the positive k_x direction, and the spins start re-phasing, increasing the signal. The phase coherence is completely recovered (the center of the echo) after the time τ_+, when:

$$\phi_G^{echo}(x) = \underbrace{+\gamma G_- x \tau_-}_{G_x<0} \underbrace{-\gamma G_+ x \tau_+}_{G_x>0} = 0 \tag{4.74}$$

and $\boldsymbol{k}$ reaches the k_y axis.

The last part of the echo scheme resembles the FID acquisition: the G_x gradient is held on for another τ_+, $\boldsymbol{k}$ moves in the $k_x > 0$ half and the signal cancels away again.

The time interval between the rf excitation and the center of the echo is called *echo time* and it is referred to as T_E. In order to minimize T_E (see below), the negative lobe of G_x is usually applied contemporaneously to G_y, and the general condition for having a GRE is:

$$\int_{T_E} G_x(t)dt = 0. \tag{4.75}$$

The $\boldsymbol{k}$ trajectory for the full echo sampling is shown with red arrows in Fig.4.4b, while the scheme of the sequence, with the basic elements discussed above, is shown in Fig. 4.5. Standard conventions for the sequences representation have be adopted [28].

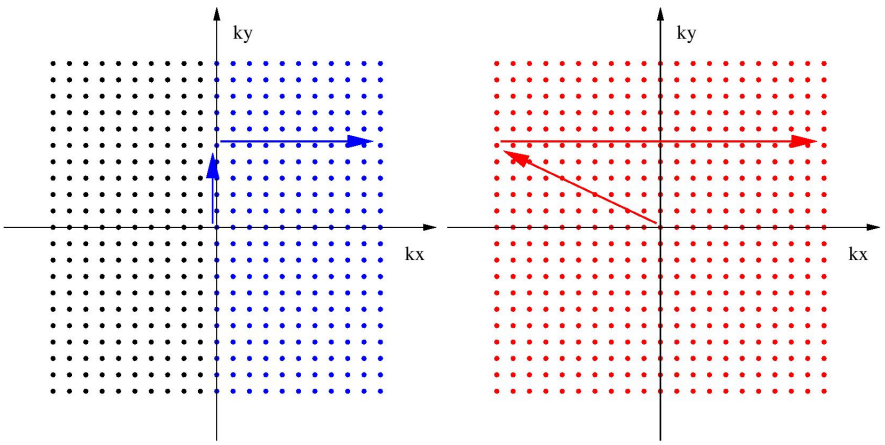

(a) FID sampling (b) Echo sampling

Figure 4.4. $\boldsymbol{k}$ *trajectories across the k-space for the FID and echo sampling schemes. The visited sampling points in the two cases are shown as colored points.*

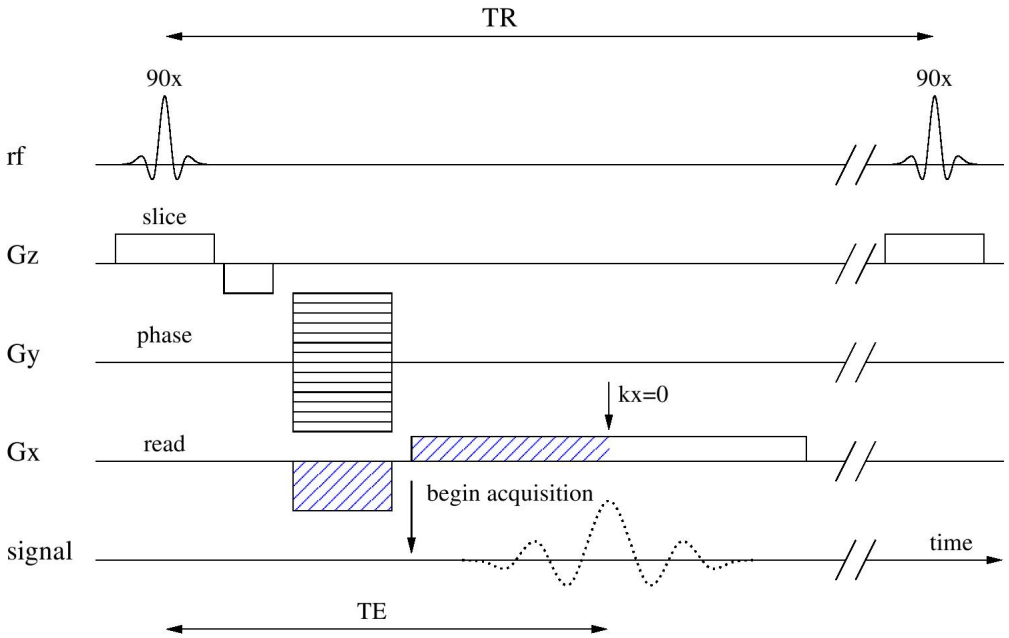

Figure 4.5. *Scheme of the basic elements of the GRE sequence. The dashed blue areas of the read gradient represent the echo condition expressed Eqn. 4.74. T_R and T_E are also reported.*

4.2.1 Echoes and T_2-weighted images

The full echo sampling scheme confers two advantages over the FID acquisition:

- The double of the sampling k-points are acquired, so there is a factor 2 of SNR gain.
- The signal is sampled in a raster of $\boldsymbol{k}$ points centered at the k-space origin, therefore there is not dispersion spectrum and $\rho(\boldsymbol{r})$ can be calculated directly by taking the modulus of the resulting FT.
- The delay between excitation pulse and acquisition start can be used for applying the phase gradients or other magnetization manipulations.

There is, however, a difficulty with the full echo sampling scheme where T_2 relaxation is significant. The acquisition of the maximum of the signal is delayed at the center of the echo, when part of the transverse magnetization is already lost. The effect is even enhanced by the inhomogeneities in the static field introduced by the gradients, reducing the transverse relaxation time to T_2^* (Eqn. 4.47).
In order to maximize the signal, the minimum echo time should be chosen. A longer T_E

can, however, be employed to get an image contrast between areas having different T_2, thus obtaining a *T_2-weighted image*.

4.2.2 Spoiling residual magnetization

If T_R is set very short ($T_R \sim T_2^*$), a fraction of the transverse magnetization of the preceding repetition can still be present at the acquisition time, disturbing the signal.
The *spoiling* is the method by which residual transverse magnetization is destroyed deliberately prior to the excitation pulse of the subsequent repetition. Sequences may be rf spoiled or gradient spoiled, or both.
rf spoiling involves applying a phase offset to each successive rf excitation pulse.
Think of it as the same flip angle but in a different direction, so that the residual magnetization in the xy-plane always points in a different direction, preventing any build up towards a steady state.
Gradient spoiling occurs after each echo by using strong gradients in the slice-select direction after the frequency encoding. Spins in different locations, experiencing a variety of magnetic field strengths, precess at differing frequencies, thus, dephasing.
Magnetic field gradients are not very efficient at spoiling the transverse steady state. To be effective, the spins must be forced to precess far enough to become phased randomly with respect to the rf excitation pulse.

4.2.3 GRE signal

The steady state image signal for a GRE sequence is given by:

$$I = A\frac{(1 - e^{(-T_R/T_1)})\sin\alpha}{1 - e^{-T_R/T_1}e^{-T_R/T_2^*} - \cos\alpha(e^{-T_R/T_1}e^{-T_R/T_2^*})}e^{-T_E/T_2^*} \tag{4.76}$$

where A is a constant which takes into account the proton density and the receiver gain as well, α is the FA of the excitation pulse, whereas T_1, T_2 and T_R have their usual meaning. When $T_R \gg T_2^*$ (or under conditions of perfect spoiling of the transverse magnetization) e^{-T_R/T_2^*} approach zero; if also $T_E \ll T_2^*$ holds, then Eqn. 4.76 reduces to:

$$I = A\frac{(1 - e^{-T_R/T_1})\sin\alpha}{1 - \cos\alpha e^{-T_R/T_1}}. \tag{4.77}$$

Recalling now Eqn. 4.67, from their similarity, we can understand that Eqn. 4.77 describes the steady state signal and that can be analogously derived.
The dependence upon T_R and FA of the GRE signal, as expressed in Eqn. 4.77, is shown

in Fig. 4.6. Note how the FA corresponding to the maximum signal, conventionally called *Ernst angle*, increases with T_R.

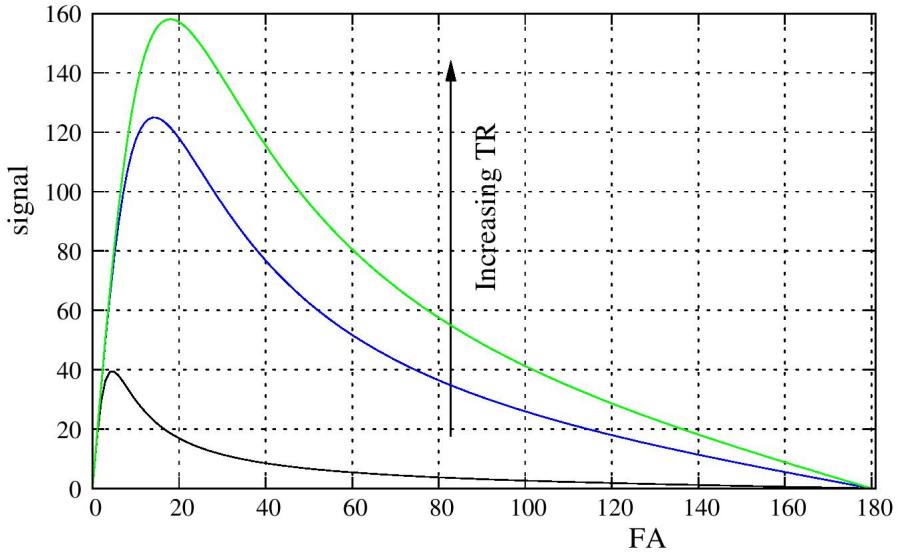

Figure 4.6. *Simulated GRE signal intensity, as expressed in Eqn. 4.77, vs FA. A and* T_1 *are set to 1 and 1000 ms, respectively, while* $T_R = 5, 50, 80$ *ms.*

4.3 Spin Echo

In spectroscopic NMR sequences, signal echoes are obtained through a 180° rf pulse following the excitation pulse.

Immediately after a 90°_x excitation pulse, in the rotating reference frame, the magnetization lies on the y-axis.

Due to field inhomogeneities, spins start dephasing by precessing in opposite directions and at different speed. If, after a time τ, a 180°_y pulse is applied, the spins are *flipped* around y so that, conserving their angular velocity, they start re-phasing. After another τ, the spins are back in phase to give a *Spin Echo* (SE), where $T_E = 2\tau$.

In SE imaging sequences rf and gradient pulses are arranged so to synchronize the gradient and spin echoes. Thanks to the y-axis flipping caused by the 180 rf pulse, the dephasing due to field gradients is recovered completely. In other words, the only source of signal reduction is the *pure* spin-spin T_2 relaxation, resulting in a net signal gain over GRE (where T_2^* is acting).

The main limit of SE imaging is that T_R can not be set as short as in GRE, due to the

higher complexity of the sequence. However, by making T_R long compared to T_E, it is possible to generate several spin echoes in one T_R interval. This is successfully utilized in *Fast Spin Echo* (FSE) sequences, where single 90°_y pulse is followed by several 180°_y pulses. Each 180°_y pulse creates an echo, which is individually phase encoded, and several k-space lines of the same slice can thus be acquired following a single excitation.
Within T_R, the transverse magnetization is subject to T_2 relaxation, so last echoes of each repetition are strongly T_2-weighted, and the resulting image is T_2-weighted as well.

4.4 Echo Planar Imaging

Echo Planar Imaging (EPI) is capable of significantly shortening MR imaging times, allowing acquisition of images in 20-100 ms. This time resolution virtually eliminates motion-related artifacts, therefore, making possible imaging of rapidly changing physiologic processes. Echo-planar images with resolution and contrast similar to those of conventional MR images can be obtained by using multishot acquisitions in only a few seconds. To obtain this time resolution, multiple lines of imaging data are acquired after a single RF excitation. Like a conventional SE sequence, a SE-EPI sequence begins with 90° and 180° RF pulses. However, after the 180°_y RF pulse, the frequency-encoding gradient oscillates rapidly from a positive to a negative amplitude, forming a train of gradient echoes (4.7). Each echo is phase encoded differently by phase-encoding blips on the phase-encoding

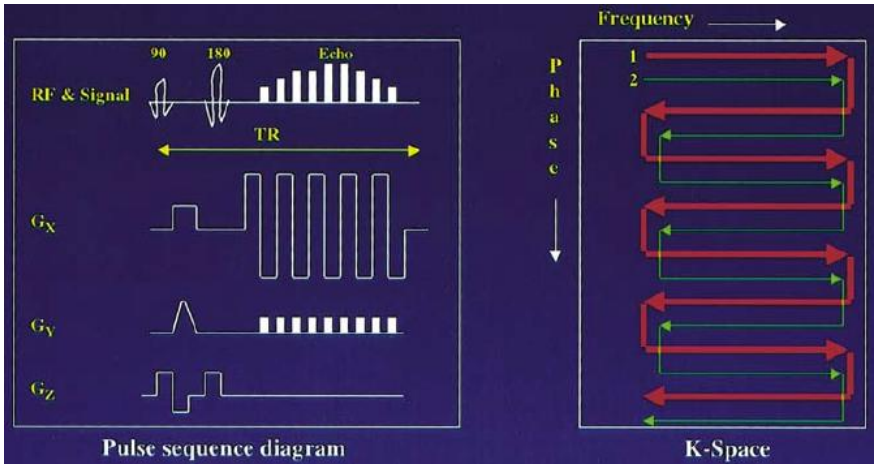

Figure 4.7. *EPI scheme. Within each TR period, multiple lines of imaging data are collected. G_x = frequency-encoding gradient, G_y = phase-encoding gradient, G_z = slice selection gradient.*

axis. Each oscillation of the frequency-encoding gradient corresponds to one line of imaging data in k space, and each blip corresponds to a transition from one line to the next in k-space. This technique is called blipped echo-planar imaging [32]. In the original echo-planar imaging method, the phase-encoding gradient was kept on weakly but continuously during the entire acquisition [33]. Today, echo-planar imaging has many variants. In one of these variants, asymmetric echo-planar imaging, data are collected only during the positive frequency-encoding gradient lobe. The negative frequency-encoding gradient lobe is used to just traverse back to the other side of k space [34]. This type of data collection strategy is also used in flow-compensated EPI.

4.4.1 Diffusion Weighted Echo Planar Imaging

One of the most used application of EPI imaging concern the diffusion of water molecules in tissues. As we said in section 3.6, diffusion is the random thermal motion of molecules through a tissue compartment. The signal intensity at MR imaging is dependent among other factors on water motion, which intrinsically produces contrast. Diffusion of water molecules through a magnetic field gradient causes intravoxel dephasing and loss of signal intensity. Water molecules diffuse approximately at a rate of only 1:10 mm/sec. In diffusion-weighted echo-planar imaging, image acquisition is sensitized to the diffusion of water molecules by inserting very strong motion-sensitizing gradient pulses into the echo-planar imaging pulse sequence. Diffusion pulses cause the echo-planar imaging MR signal to dephase or to diminish in proportion to the random velocities of the diffusing water molecules, within the order of magnitude of the voxel size during an echo time (TE). These velocities have been referred to as intravoxel incoherent motion [35]. To obtain diffusion-weighted images, a pair of strong gradient pulses (G_d) are added to the pulse sequence, usually of the SE-EPI type (spin echo ultrafast echo planar imaging preparation) that is T2 weighted, see Fig. 4.8. The G_d pulse is applied along the x, y, or z direction to obtain images of diffusion in the x, y, or z directions respectively. These twoG_d pulses are identical in amplitude and width (δ), separated by a time Δ, and placed symmetrically about the 180◦ pulse. The function of the G_d pulses is to dephase magnetization from spins which have diffused to a new location in the period Δ.

These pulses have no effect on stationary spins. For example, a stationary spin exposed to the first G_d pulse, applied along the Z axis, will acquire a phase in radians given by

$$\phi = 2\pi\gamma \int zG_z dt \tag{4.78}$$

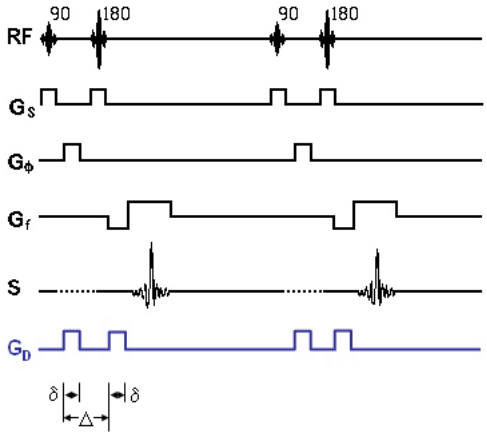

Figure 4.8. This timing diagram shows two repetitions of a diffusion weighted sequence

The spin will acquire an equal but opposite phase from the second pulse since the pulses are on different sides of the 180 degree RF pulse. Thus, their effects cancel each other out. Vice versa, the spins of the water molecules that move in the direction of the gradients, during the interval between the two gradient applications, will not be rephased by the second gradient: they dephase in relation to the hydrogen nuclei of the immobile water molecules (Fig. 4.9).

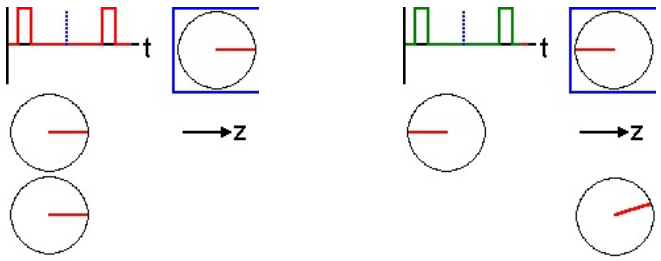

(a) (b)

Figure 4.9. a) Effect of the gradient pulses applied along z in stationary spins, b) effect of the gradient pulses applied along z in moving spins.

The relationship between the signal (S) obtained in the presence of a G_D in the i direction (G_i) and the diffusion coefficient in the same direction (D_i) is given by the

following equation where S_o is the signal at $G_i = 0$.

$$\frac{S}{S_0} = \exp\left[-(G_i\gamma\delta)2D_i(\Delta - \frac{\delta}{3}\right] = \exp(-bD) \tag{4.79}$$

where γ is the gyromagnetic ratio, δ is the duration of the gradient , Δ the time between the two pulses. b represents the degree of diffusion weighting of the sequence, expressed as the b-factor $\left[\frac{s}{mm2}\right]$, which depends on the following characteristics of the diffusion gradients:

- gradient amplitude
- application time
- time between the two gradients

Diffusion magnitude, calculated from the 3 diffusion images thus obtained, renders the image weighted in global diffusion (trace image). Two diffusion sequences with different b-factors can be used to quantitatively measure the degree of molecular mobility, by calculating the apparent diffusion coefficient (ADC). ADC is represented in the form of a map, whose values no longer depend on T2. An ADC hyposignal thus corresponds to a restriction in diffusion. In current practice, diffusion imaging for cancer detection consists of an acquisition with a b-factor b = 0 $\frac{s}{mm2}$ (T2-weighted) and imaging with a b-factor = 600 $\frac{s}{mm2}$(with diffusion weighting). The stronger the gradients, the longer they are applied and the more spread out in time, the greater the b-factor.The advantage of strong gradients is that they avoid the need to lengthen gradient time and spacing, which would impose an even longer TE (without removing the T2 weighting part of the signal).*Pure* diffusion contrast is obtained when using b-values above 1000$\frac{s}{mm2}$. However, image quality can be limited by signal loss that occurs at such b-values and higher. Diffusion sequences are actually T2 weighted sequences, sensitized to diffusion by gradients. The contrast of the diffusion image will have both a diffusion and a T2 component, which must be taken into consideration in the interpretation. Namely, a hypersignal in the diffusion image with b = 600 $\frac{s}{mm2}$ can either correspond to a diffusion restriction or to a lesion that is already in T2 hypersignal (T2-shine-through).

4.5 Fat-suppression

Fat-suppression is used in routine magnetic resonance imaging for many purposes: to suppress the signal from normal adipose tissue, to reduce chemical shift artifact, to improve

visualization of uptake of contrast material and to characterize tissues. The optimal fat-suppression technique depends on the amount of lipid that requires signal suppression.
Fat-suppression is a generic term that includes various techniques, each with specific advantages, disadvantages, and pitfalls. Lipid protons and hydrogen protons from water behave differently during an MR imaging acquisition, and fat-suppression techniques are based on these differences. Two major properties are involved: first, there is a small difference in resonance frequency, δ_{f_0}, between lipid and water protons, which is related to the different electronic environments. This so-called chemical shift allows frequency-selective fat-saturation. Second, the difference in T_1 between adipose tissue and water can be used to suppress the fat signal with inversion-recovery techniques. The chemical shift between lipid and water also allows fat-suppression with opposed-phase imaging.
During a fat-saturation acquisition, a frequency-selective saturation radio-frequency pulse with the same resonance frequency as that of lipids is applied to each slice-selection radio-frequency pulse. A homogeneity spoiling gradient pulse is applied immediately after the saturation pulse to dephase the lipid signal (Fig. 4.10).
The signal excited by the subsequent slice-selection pulse contains no contribution from lipid [36].

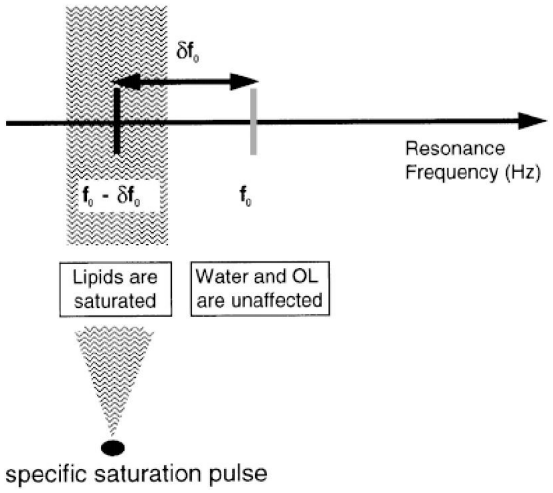

Figure 4.10. *Fat-saturation. Diagram shows a frequency-selective saturation radio-frequency pulse applied to each slice-selection radio-frequency pulse. OL = olefinic fatty acid [36].*

4.5.1 Advantages

Fat-saturation is lipid specific. Therefore, this method is reliable for contrast material-enhanced T_1-weighted imaging and tissue characterization particularly in areas with a large amount of fat. Fat-saturation is also useful for avoiding chemical shift misregistration artifacts. Because fat-suppression is achieved by preceding the normal acquisition with a frequency-selective saturation pulse, fat-saturation can be used with any imaging sequence. Signal in non-adipose tissue is practically unaffected as long as the saturation pulse frequency and bandwidth are properly selected; the signal-to-noise ratio in adipose tissue is of course decreased. Fat-saturation thus allows good visualization of small anatomic details [36].

4.5.2 Disadvantages

To achieve reliable fat-saturation, the frequency of the frequency-selective saturation pulse must equal the resonance frequency of lipid. However, inhomogeneities of the static magnetic field will shift the resonance frequencies of both water and lipid. In these areas, the saturation pulse frequency might not equal the lipid resonance frequency; this discrepancy would result in poor fat-suppression. Even worse, the saturation pulse can saturate the water signal instead of the lipid signal; the result would be a water-suppressed image. Static field inhomogeneities inherent in magnet design are relatively small in modern magnets and can be reduced by decreasing the field of view, centering over the region of interest, and autoshimming. However, substantial inhomogeneities can be caused by local magnetic susceptibility differences. Inhomogeneities are also likely to occur in areas of sharp variations in anatomic structures.

Inhomogeneities in the radio-frequency field can also reduce the efficacy of fat-saturation. For complete saturation of the lipid signal, the saturation pulse must be exactly 90°. Where the radio-frequency field is inhomogeneous, the pulse will be greater or less than 90° and will leave residual fat signal. The problem can be exacerbated by use of surface coils. Even when surface coils are used for reception only, the presence of such coils can distort the transmitter field sufficiently so that substantial fat signal is left.

Besides technical problems, there are two other reasons why fat-saturation can result in incomplete fat-suppression. First, the fraction of adipose tissue that is water will not be saturated. Second, a small fraction of fatty acids (5%) have the same resonance frequency as water, and signal from these fatty acids will be unsuppressed; such fatty acids, which

are free or bound to triglycerides, are called olefinic fatty acids or alkenes. Therefore, detection of a small amount of fat can be impaired.
The chemical shift between lipid and water increases with the strength of the magnetic field (at 1.0 T, $\delta_{f_0} \approx 150Hz$; at 1.5 T, $\delta_{f_0} \approx 220Hz$). Fat-suppression is therefore of lower quality when low-field-strength magnets are used because δ_{f_0} is small. It is thus difficult to achieve effective lipid saturation without also producing water saturation [36].

4.6 Other principal techniques

4.6.1 Inversion-Recovery imaging

In inversion-recovery imaging, suppression of the fat signal is based on differences in the T_1 of the tissues. The T_1 of adipose tissue is shorter than the T_1 of water. After a 180° inversion pulse, the longitudinal magnetization of adipose tissue will recover faster than that of water. If a 90° pulse is applied at the null point of adipose tissue, adipose tissue will produce no signal whereas water will still produce a signal (Fig. 4.11). Therefore, the fat signal can be suppressed by using a short inversion time inversion-recovery sequence (STIR). As long as the repetition time is much longer than the inversion time (TI), the null point will be at a TI (TI_{null}) equal to 0.69 times the T_1. The T_1 and hence the optimal TI_{null} for achieving suppression of adipose tissue signal depend on the magnetic field strength. At 1.5 T, TI_{null} occurs at approximately 130-170 msec.
STIR imaging is usually performed with a fast spin-echo readout sequence, which allows shorter acquisition times than does a conventional spin-echo sequence [36].

4.6.2 Opposed-phase imaging

The opposed-phase technique is based on phase differences in images acquired at different echo times.
Because lipid protons and water protons have different resonance frequencies, the phases of these protons relative to each other change with time after the initial excitation (Fig. 4.12).
Immediately after excitation, the lipid signal and water signal are in phase (i.e., the phase difference between them is zero). However, water protons precess fractionally faster than lipid protons; therefore, after a few milliseconds, the phase difference between the two is 180° (i.e., the phase is opposed). After a few more milliseconds, the water spins complete a

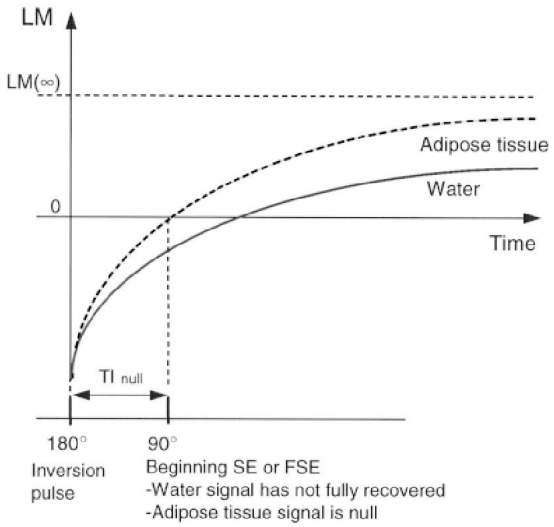

Figure 4.11. *Inversion-recovery imaging. Diagram shows the behavior of adipose tissue signal and water signal during an inversion-recovery sequence. Note that the water signal has not fully recovered at the beginning of the imaging sequence. FSE = fast spin-echo imaging, LM = longitudinal magnetization, SE = spin-echo imaging, TI = inversion time [36].*

360° rotation relative to the lipid spins and the spins are again in phase. The spins can thus be sampled in an in-phase or opposed-phase condition by selecting the appropriate echo time. In general, this technique is applicable only to gradient-echo sequences. The 180° refocusing pulse used in spin-echo sequences always brings the lipid signal and water signal back into phase regardless of the echo time. During an MR imaging sequence, the signal within a voxel is the vector sum of the lipid and water signals of the protons within that voxel (Fig. 4.13). The lipid signal and water signal are additive in in-phase images, but in opposed-phase images the signal is the difference between the lipid and water signals. Therefore, opposed-phase imaging reduces the signal from fatty tissue. Opposed-phase imaging is best suited to suppressing the signal from tissues that contain similar amounts of lipid and water. In tissues that contain predominantly lipid or predominantly water, the reduction in signal is small. For example, in adipose tissue, voxels contain mainly adipocytes and the signal from water is much smaller than the signal from lipid. The small amount of water produces only a small reduction in signal. Therefore, the adipose tissue signal is fairly high (Fig. 4.14) and the opposed-phase image is poorly fat suppressed. Conversely, voxels that contain tissue infiltrated by fat or only small areas of adipose tissue have a low signal in opposed-phase images. In this situation, the lipid and water signals

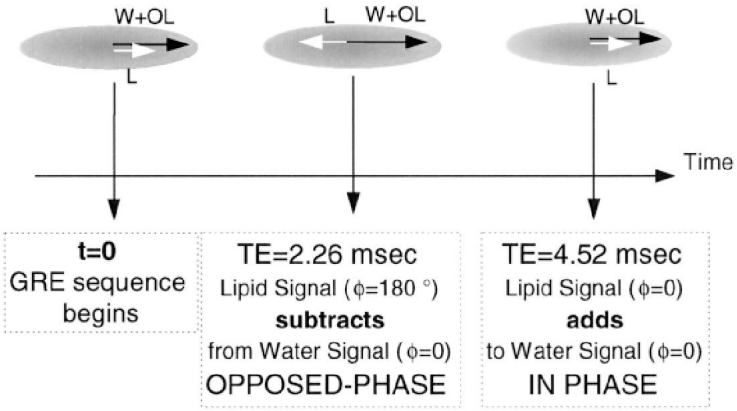

Figure 4.12. *Opposed-phase and in-phase imaging. Diagram shows the behavior of lipid (L) signal and water (W) signal relative to the echo time (TE) during a gradient-echo (GRE) sequence (1.5 T). OL = olefinic fatty acid, t = time [36].*

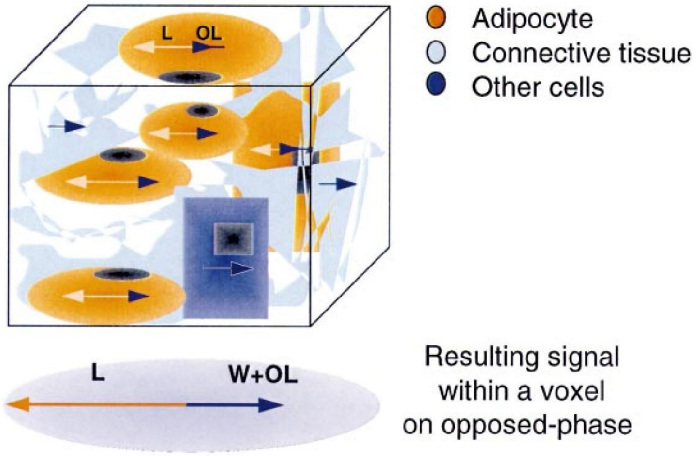

Figure 4.13. *Opposed-phase imaging. Diagram shows the signal within a heterogeneous voxel. The signal is the vector sum of the lipid (L) and water (W) signals. According to the phase of these signals, they add or subtract and produce a higher or lower signal within the voxel. OL = olefinic fatty acid [36].*

partially cancel. The signal in opposed-phase imaging is lower than the signal produced with fat-saturation: in opposed-phase imaging, the signal consists of the water signal minus the lipid signal; with fat-saturation, the signal consists of the water signal alone (Fig. 4.15) [36].

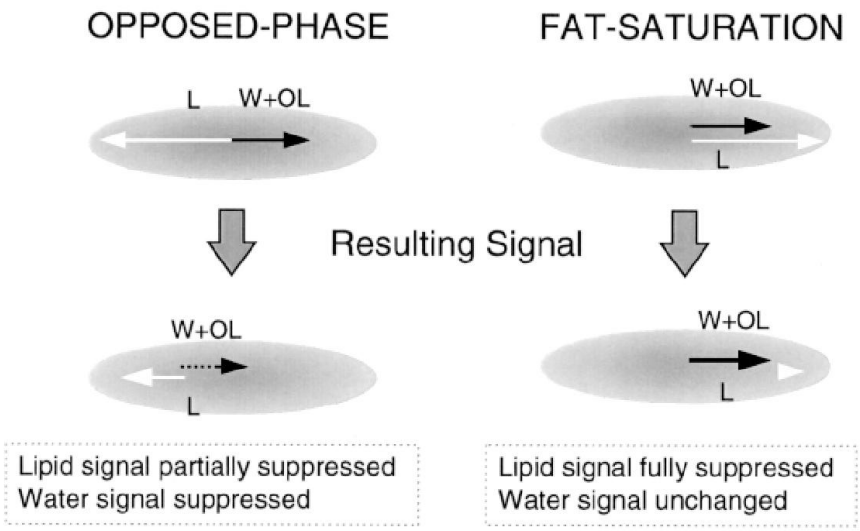

Figure 4.14. *Opposed-phase imaging versus fat-saturation. Diagram shows the respective signals from tissue with a large amount of fat. L = lipid, OL = olefinic fatty acid, W = water [36].*

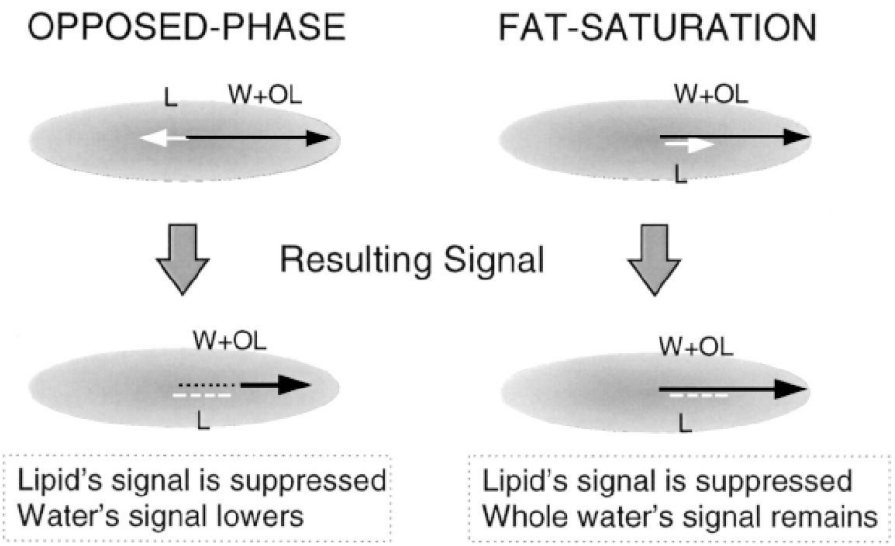

Figure 4.15. *Opposed-phase imaging versus fat-saturation. Diagram shows the respective signals from tissue with a small amount of fat. L = lipid, OL = olefinic fatty acid, W = water [36].*

Part I

Registration, Lesion Detection and Discrimination for Breast Dynamic Contrast Enhanced Magnetic Resonance Imaging

For breast cancer detection and diagnosis, the main advantages of DCE-MRI over traditional imaging modalities are the possibility to obtain and analyze both morphological and functional features related to malignant growth, the high sensitivity in invasive breast carcinoma detection and the ability to provide high resolution three-dimensional (3D) images [37, 38, 39]. This technique relies on signal enhancement after the intravenous injection of a two-compartment gadolinium-based paramagnetic contrast agent: the intensity increases with the concentration of the contrast agent as it perfuses the tumoral vasculature and diffuses in the extravascular extracellular space. The time-intensity curve is therefore correlated with neoangiogenic-induced vascular changes and allows to provide information on tumor biological aggressiveness, to monitor tumor response to therapy and to define the state of angiogenesis [24].

DCE-MRI shows promise in detecting both invasive and ductal carcinoma in situ cancers, gives information on the biological aggressiveness of tumors and may be utilized to evaluate response to neoadjuvant chemotherapy [37, 38, 39, 40]. However, DCE-MRI data analysis requires interpretation of hundreds of images and is therefore time-consuming [41].

The CAD system developed during this thesis aids in the visualization of kinetic information by providing color mapping, facilitates analysis through graphical and quantitative representations and provides an index of suspicion. In order to compute morphological features and kinetic curves for use in predicting pathology probability (discrimination step), a step of motion compensation between unenhanced and enhanced images (registration) and a procedure of lesion identification (lesion detection) are included. The system here proposed is fully automatic, therefore do not suffer from high inter- and intra-observer variability typical of manual or semi-automatic systems [42, 43, 44]. As it is not operator dependent, a fully automatic lesion segmentation process has the potential to reduce reading time and provide more reproducible results. Unfortunately, few papers have addressed automatic lesion detection and segmentation techniques for breast DCE-MRI [45, 46, 47]. Furthermore, these methods have been tested only on non fat-saturated (fat-sat) contrast-enhanced images. Since enhancing lesions may become isointense to adjacent fatty tissue after contrast material injection, fat-saturation has been introduced to enhance the contrast between lesion and surrounding tissue and to overcome the limitations due to subtraction artifacts [38]. Fat-sat sequences, however, introduce additional challenges for breast lesion segmentation, especially due to the lower signal-to-noise-ratio (SNR) within the breasts.

Chapter 5

Breast DCE-MRI

5.1 Dynamic curves

Using dynamic datasets (i.e. the time-signal intensity curves), two different criteria may be used to describe lesion enhancement kinetics. First, behavior of signal intensity in the early phase after the administration of contrast material is evaluated by means of the steepness of the post-contrast signal intensity curve; several descriptors are in use for this criterion: "curve slope", "early-phase enhancement rate", or "enhancement velocity", which have been given by the percentage of increase in signal intensity with respect to the signal intensity before the administration of contrast material.
Second, the behavior of signal intensity in the intermediate and late post-contrast periods may be traced to derive diagnostic information. This time course is visualized by placing a region of interest (ROI) on the lesion to plot the time-signal intensity curve. Visual or quantitative evaluation is focused on the shape of the time-signal intensity curve: whether the signal intensity continues to increase after the initial upstroke, whether it is cut off and reaches a plateau, or whether it washes out.

5.1.1 Kuhl's study: a milestone in the dynamic curves analysis

The study of Kuhl et al. [48] was basic to assess the relevance of the signal intensity time course for the differential diagnosis of enhancing lesions in dynamic magnetic resonance (MR) imaging of the breast. The study was a prospective trial with a standardized protocol. The protocol was tailored to selectively determine the diagnostic utility of signal

intensity time course analysis in dynamic breast MR imaging (i.e. to elucidate its specific contribution to the differential diagnosis of enhancing lesions in breast MR imaging). Time-signal intensity curves of enhancing lesions were plotted and presented to two radiologists who were blinded to any clinical or mammographic information of the patients. The radiologists were asked to rate the time courses as having a steady, plateau, or washout shape (type I, II, or III, respectively). The classification of the lesions on the basis of the time course analysis was then compared with both the breast MR imaging diagnosis without time course analysis (i.e., based on enhancement rates) and with the lesions' definitive diagnoses. The definitive diagnosis was obtained histologically by means of excisional biopsy or by means of follow-up in the cases that, on the basis of history, clinical, mammographic, ultrasonographic (US), and breast MR imaging findings, were rated to be probably benign.

Two hundred sixty-six breast lesions were examined with a two-dimensional dynamic MR imaging series and subtraction post-processing. The enhancement rate was quantified by means of an ROI-based determination of lesion signal intensity before and after the injection of gadopentetate dimeglumine. In particular, ROIs were placed selectively in the areas of the most rapid and strongest enhancement. The relative enhancement (percentage of signal intensity increase) was calculated according to the enhancement formula:

$$\frac{SI_{post} - SI_{pre}}{SI_{pre}} \times 100, \tag{5.1}$$

where SI_{pre} is the pre-contrast signal intensity and SI_{post} is the post-contrast signal intensity. To assess the early-phase signal intensity increase, the enhancement for the first post-contrast image was calculated. By plotting the lesion signal intensity over time, the time-signal intensity curve was obtained to depict the lesions' enhancement behavior in the early, intermediate and late post-contrast periods. The three curve types (Fig. 5.1) differ in their signal intensity time courses in the intermediate and late post-contrast periods. Type I is straight or curved. In type Ia, the straight type, the signal intensity continues to increase over the entire dynamic period; in type Ib, the curved type, the time-signal intensity curve is flattened in the late post-contrast period because of saturation effects. Type II is a plateau in which there is an initial upstroke, after which enhancement is abruptly cut off, and the signal intensity plateaus in the intermediate and late post-contrast periods. Type III is a washout in which there is an initial upstroke, after which enhancement is abruptly cut off, and the signal intensity decreases (washes out) in the intermediate post-contrast period (i.e., 2-3 minutes after injection of contrast material).

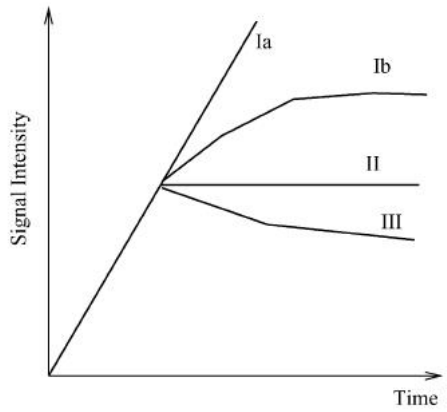

Figure 5.1. *Schematic drawing of the time-signal intensity curve types. Type I corresponds to a straight (Ia) or curved (Ib) line; enhancement continues over the entire dynamic study. Type II is a plateau curve with a sharp bend after the initial upstroke. Type III is a washout time course. On the left of the curves conjunction point is the early post-contrast phase. On the right is the intermediate and late post-contrast phase.*

From literature, the lesions were classified according to the different time-signal intensity curves. A type I time course was rated to be indicative of a benign lesion, type II was rated as suggestive of malignancy, and type III was rated as indicative of a malignant lesion. Lesions were classified according to their early-phase enhancement rates as benign if the relative signal intensity increase was less than or equal to 60%, indeterminate if it was more than 60% and less than or equal to 80%, and malignant if it was more than 80%. To determine the diagnostic accuracies, lesion classifications on the basis of the enhancement rates and curve types was compared with the lesions' definitive diagnoses.

The results of Kuhl's study showed that the early-phase enhancement rate is markedly higher in malignant lesions than in benign (Fig. 5.2) and that the shape-types II and III of the time-signal intensity curve are suggestive of breast cancer, while type I is suggestive of benign lesion (Fig. 5.3). Therefore, Kuhl et al. demonstrated that the classification scheme of three curve types (Fig. 5.1) provides a very valuable insight to identify suspicious volumes.

However, the analysis of lesion enhancement kinetics should not be used as a stand-alone diagnostic criterion but that it should be integrated into the process of lesion differential diagnosis. In fact, the following principles must be taken into account when dealing with time courses: the time-signal intensity curve analysis seems most useful in the differential

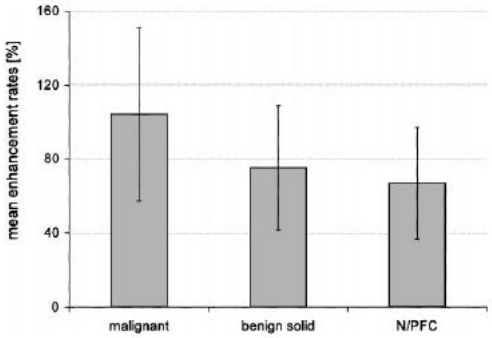

Figure 5.2. *Bar graph shows the mean early-phase enhancement rates in breast cancers, benign solid tumors, and fibrocystic changes (N/PFC: non proliferative and proliferative fibrocystic change) ± SD (error bars). Enhancement rates are calculated for the 1st post-contrast minute [48].*

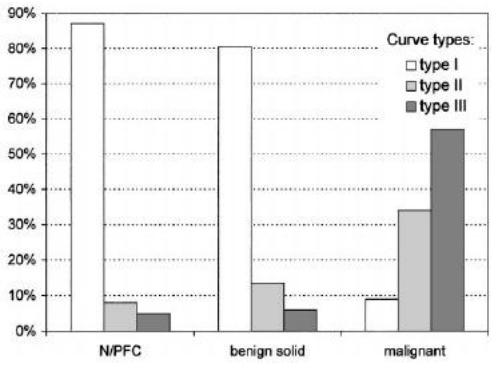

Figure 5.3. *Bar graph shows the distribution of time-signal intensity curve types in malignant lesions, benign solid lesions, and fibrocystic changes (N/PFC).*

diagnosis of focal lesions with rapid enhancement. In malignant lesions with slow enhancement, the underlying poor angiogenic activity may also prevent a washout or plateau time course. Particularly lobular or scirrhous ductal invasive cancers (and possibly also ductal carcinoma in situ) with slow or gradual enhancement may exhibit type I time courses (in these lesions morphology is almost always suggestive). Besides, a washout phenomenon is a very specific, albeit not very sensitive, indicator of malignancy.

5.2 DCE-MRI indications

Current indications for breast MRI include, but are not limited to:

1. screening.

   a. Screening of high-risk patients.

Recent clinical trials have demonstrated that breast MRI can significantly improve the detection of cancer that is otherwise clinically and mammographically occult. Breast MRI may be indicated in the surveillance of women with more than a 20% lifetime risk of breast cancer (for example, individuals with genetic predisposition to breast cancer by either gene testing or family pedigree, or individuals with a history of mantle radiation for Hodgkin's disease). Although there is no direct evidence that screening with MRI will reduce mortality, it is thought that early detection by using annual MRI as surveillance, in addition to mammography, may be useful.

b. Screening of the contralateral breast in patients with a new breast malignancy.
MRI can detect occult malignancy in the contralateral breast in at least 3% to 5% of breast cancer patients.

c. Breast augmentation - postoperative reconstruction and free injections.
Breast MRI using contrast may be indicated in the evaluation of patients with silicone or saline implants and/or free injections with silicone, paraffin, or polyacrylamide gel in whom mammography is difficult. The integrity of silicone implants can be determined by non-contrast MRI.

2. Extent of disease.

a. Invasive carcinoma and ductal carcinoma in situ (DCIS).
Breast MRI may be useful to determine the extent of disease and the presence of multifocality and multicentricity in patients with invasive carcinoma and ductal carcinoma in situ (DCIS). MRI can detect occult disease up to 15% to 30% of the time in the breast containing the index malignancy. MRI determines the extent of disease more accurately than standard mammography and physical examination in many patients. It remains to be conclusively shown that this alters recurrence rates relative to modern surgery, radiation, and systemic therapy.

b. Invasion deep to fascia.
MRI evaluation of breast carcinoma prior to surgical treatment may be useful in both mastectomy and breast conservation candidates to define the relationship of the tumor to the fascia and its extension into pectoralis major, serratus anterior, and/or intercostal muscles.

c. Post-lumpectomy with positive margins.

Breast MRI may be used in the evaluation of residual disease in patients whose pathology specimens demonstrate close or positive margins for residual disease.

d. Neoadjuvant chemotherapy.

Breast MRI may be useful before, during, and/or after chemotherapy to evaluate treatment response and the extent of residual disease prior to surgical treatment. If used in this manner, a pretreatment MRI is highly recommended. MRI-compatible localization tissue markers placed prior to neoadjuvant chemotherapy may be helpful to indicate the location of the tumor in the event of complete response with no detectable residual tumor for resection.

3. Additional evaluation of clinical or imaging findings.

a. Recurrence of breast cancer.

Breast MRI may be useful in women with a prior history of breast cancer and suspicion of recurrence when clinical, mammographic, and/or sonographic findings are inconclusive.

b. Metastatic cancer when the primary is unknown and suspected to be of breast origin.

MRI may be useful in patients presenting with metastatic disease and/or axillary adenopathy and no mammographic or physical findings of primary breast carcinoma. Breast MRI can sometimes locate the primary tumor and define the disease extent to facilitate treatment planning.

c. Lesion characterization.

Breast MRI may be indicated when other imaging examinations, such as ultrasound and mammography, and physical examination are inconclusive for the presence of breast cancer, and biopsy could not be performed (e.g., possible distortion on only one mammographic view without a sonographic correlate).

d. Postoperative tissue reconstruction.

Breast MRI may be useful in the evaluation of suspected cancer recurrence in patients with tissue transfer flaps (rectus, latissimus dorsi, and gluteal).

e. MRI-guided biopsy.

MRI is indicated for guidance of interventional procedures such as vacuum assisted biopsy and preoperative wire localization for lesions that are occult on

mammography or sonography and demonstrable only with MRI [49].

5.3 Technical aspects of breast DCE-MRI image acquisition

The conventional breast MRI investigation begins pre-contrast with either T_2 or T_1-weighted images. The signal from the body coil can be used to evaluate the position and anatomy of the breasts. Furthermore, both axillae, the supraclavicular fossae, the chest wall and anterior mediastinum can be checked (e.g., for enlarged lymph nodes). However, this is not the purpose of a breast MRI, and this evaluation may also be omitted as there is no evidence of its diagnostic value. Afterwards the signal from the dedicated double breast coil should be used. T2-w fast spin echo images can be performed as a start. In the T2-w images water-containing lesions or edematous lesions have an intense signal, and in this sequence small cysts and myxoid fibroadenomas are very well identified. In most cases cancer does not yield a high signal on T2-w images; thus, these sequences can be useful in the differentiation between benign and malignant lesions. However, as most of these lesions can also be identified onT1-w images, there is no evidence as yet of added value of T2-w sequences in breast MRI.

The most commonly used sequence in breast MRI is a T1-w, dynamic contrast-enhanced acquisition. As already said, the sequence is called "dynamic" because it is first performed before contrast administration and is repeated multiple times after contrast administration. A T1-w 3D or 2D (multi-slice) spoiled gradient echo pulse sequence is obtained before contrast injection and then repeated as rapidly as possible for 5 to 7 min after a rapid intravenous bolus of a Gd-containing contrast agent. Three-dimensional imaging indicates that phase encoding, frequency encoding, and section encoding are all achieved by applying suitable gradients during image acquisition. For 2D imaging, section encoding is achieved by means of selective excitation.

Compared with 2D imaging, 3D imaging has the inherent advantage of stronger T_1 contrast: 3D imaging uses a shorter repetition time than does 2D multisection imaging and has a higher inherent signal-to-noise ratio, which therefore allows thinner sections (or partitions) to be acquired [38]. In turn, a 2D sequence suffers less from motion and pulsation artifacts. Both sequences can be performed with and without fat-suppression. The choice of the image orientation is important. For bilateral dynamic breast MRI, axial or coronal orientations are most frequently used. Coronal imaging has advantage in that it can reduce heart pulsation artifacts, but it is more susceptible to respiratory motion and also to flow

artifacts because vessels tend to travel perpendicular to the slice-encoding direction. Although bilateral sagittal imaging is possible today, it requires about double the number of slices required for the other orientations. As this hampers the spatio-temporal resolution, such an orientation is currently not feasible.

Temporal resolution. Peak enhancement in the case of breast cancer occurs within the first 2 mins after the injection of contrast medium. Therefore, relatively short data acquisition times, in the order of 60-120 s per volume acquisition, are necessary. This allows sampling of the time course of signal enhancement after contrast injection, which is useful because the highly vascularized tumor of the breast shows a faster contrast uptake than the surrounding tissue. More importantly, it enables a detailed analysis of morphological details, because only in the very early post-contrast phase, the contrast between the cancer and the adjacent fibroglandular tissue is optimal. Tumors may lose signal (a phenomenon referred to as "wash-out") as early as 2-3 mins after contrast material injection, whereas the adjacent fibroglandular tissue can still exhibit substantial enhancement, resulting in little contrast between the cancer and the fibroglandular tissue. Long acquisition times will be associated with the risk of not resolving fine details of margins and internal architecture; this could have key importance for the differential diagnosis, and may even run the risk of missing cancers altogether because they are masked by adjacent breast tissue.

A dynamic sequence demands at least three time points to be measured, that is, one before the administration of contrast medium, one approximately 2 mins later to capture the peak and one in the late phase to evaluate whether a lesion continues to enhance, shows a plateau or shows early wash-out of the contrast agent (decrease of signal intensity). It is thus recommended to perform at least two measurements after the contrast medium has been given, but the optimal number of repetitions is unknown. However, the temporal resolution should not compromise the spatial resolution.

Spatial resolution. Detailed high spatial resolution is the other prerequisite for diagnosing breast cancer with the aid of MR imaging. This is in close agreement with mammography or breast ultrasonography (US), where for the past several years attempts have been made to further improve the visualization of morphological details. The final spatial resolution of the images depends on different factors, especially the size of the imaging volume, defined by the field of view (FOV), the slice thickness and the acquisition matrix. Breast MRI should be capable of detecting all lesions larger than or equal to 5 mm. Therefore, the voxel size should be under 2.5 mm in any direction. Preferably, the in-plane resolution should be substantially higher as morphologic features needed for lesion characterization,

such as margin appearance, can only be evaluated when the resolution is sufficiently high. Therefore, the in-plane resolution should be at least 1 mm^{-1}, in other words: pixel size (FOV/matrix) should not be greater than 1×1 mm, which requires a matrix of at least 300×300 in a 300-mm FOV.
In breast MR, however, acquisition speed and spatial resolution are diverging demands. Any increase in spatial resolution (e.g., an increase in the size of the acquisition matrix) is associated with an increase in acquisition time [38, 50].

5.4 MRI protocols

The dataset has been divided in two groups. Group A included all studies acquired on a 1.5 Tesla (T) scanner (Signa Excite HDx, General Electric Healthcare, Milwakee, WI) using a eight-channel breast radiofrequency coil and a fat-sat three-dimensional (3D) axial fast spoiled gradient-echo sequence (VIBRANT®, General Electric) with the following technical parameters: repetition time/echo time (TR/TE)=4.5/2.2 ms, flip angle 15°, reconstructed matrix 512x512, field of view 32 cm, slice thickness 2.6 mm,pixel size 0.39 mm^2. A total of seven scans were acquired for each study: one baseline, 5 contrast-enhanced frames with 50-s time resolution, and one delayed frame acquired 7 minutes after contrast injection. Gadopentetate dimeglumine (Gd-DPTA, Magnevist, Bayer-Schering, Berlin, Germany) was administered at a dose of 0.1 mmol/kg at 2 mL/s, followed by 20 mL of saline solution at the same rate.
Group B comprised studies performed on a different 1.5T scanner (Sonata Maestro Class, Siemens, Erlangen, Germany), using a dynamic 3D axial spoiled fast low angle shot sequence using a four-element two-channel coil, with the following technical parameters: TR/TE=11/4.9 ms, flip angle 25°, matrix 512x512, field of view 384 mm, slice thickness 1.3 mm, pixel size 0.56 mm2. Gd-BOPTA (MultiHance, Bracco, Milan, Italy) was used as contrast agent, administering 0.1 mmol/kg at 2 mL/s, followed by 20 mL of saline solution at the same rate. One baseline scan was acquired before contrast injection, followed by 5 contrast enhanced frames taken 118 s apart. Fat-sat sequences were not performed in group B patients. A training and a testing set were developed by randomly selecting studies from the 2 groups. The training set was used to optimize the parameters of the algorithms, whereas system performances were evaluated on the testing set. The characteristics of the training set are detailed in Figure 5.4. Lesion greatest diameter was measured manually

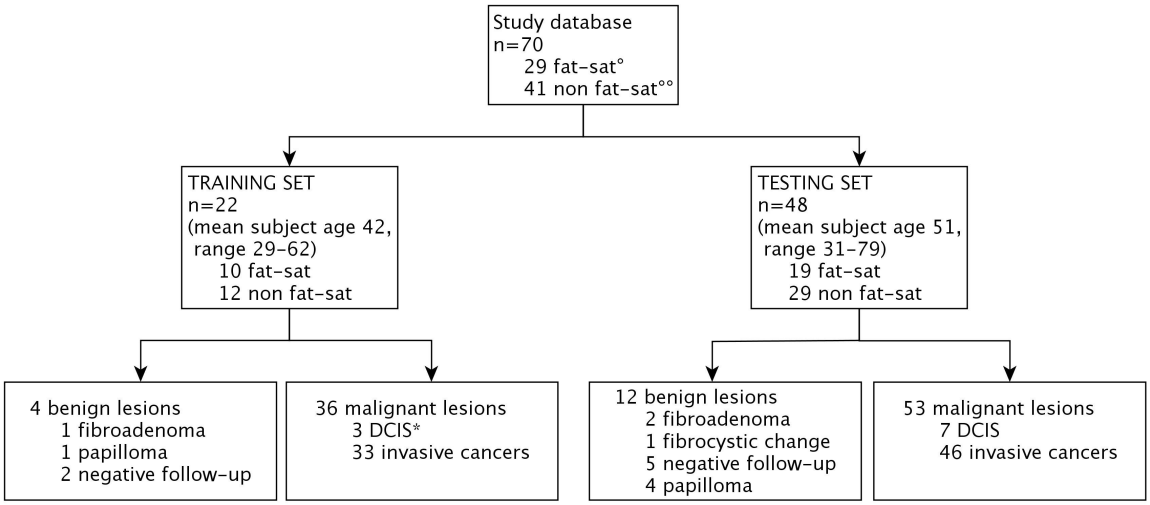

Figure 5.4. *Flow diagram showing main demographic, clinical and technical information of the study database. °Fat-sat=fat-saturation scans. °°Non-fat-sat = non-fat-saturated images. ∗DCIS = Ductal Carcinoma In Situ.*

by an experienced radiologist with an electronic caliper on the axial plane at its maximum extension. Median diameter was 16 mm (range, 12-37 mm) for benign lesions and 19 mm (range 5-90 mm) for malignant lesions; 6 of the 36 malignant lesions were sized 10 mm or less. The reference standard was surgery and histological evaluation or follow-up in some benign lesions. Enhanced areas smaller than 5 mm in diameter, the so-called foci according to the definition of the American College of Radiology (ACR) Breast Imaging Reporting and Data System (BI-RADS) for breast MRI, were not evaluated. In the majority of cases, these foci are due to a focal proliferation of glandular tissue, known as focal adenosis [38]. The studies of both datasets were acquired with the patient in the prone position, as illustrated in Fig. 5.5.

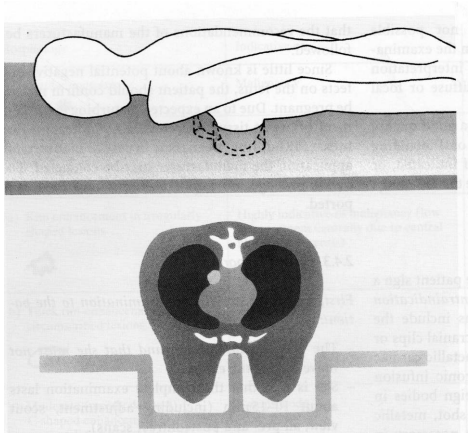

Figure 5.5. *Patient prone position during DCE-MR exam.*

Chapter 6

Breast lesion detection methods

The lesion detection pipeline consists of four main processing steps: breast segmentation, image registration, lesion detection and false positive (FP) reduction, none of which requires user interaction (see Fig. 6.1). Breast segmentation automatically identifies the breast and axillary regions to reduce the computational burden and prevent FPs due to enhancing structures (such as the heart and extra-breast vessels). The contrast-enhanced images are then registered to the unenhanced image to correct for possible misalignments in the dynamic sequence due to patient's movement. The lesion detection step consists in the extraction of suspicious contrast enhanced areas and the FP reduction step identifies and discards regions incorrectly extracted.

6.1 Breasts segmentation

This process includes the identification of the approximate size and location of each breast, and the breast segmentation itself. A rough estimate of breast location was obtained by identifying the most anterior point reached by the breasts, which is defined as the maximum point, and the minimum point which is the deepest point within the concavity between the breasts, as shown in Figure 6.2. These measures were obtained following a rough segmentation of the patient's body. To separate the skin and internal structures from external air, Otsu's thresholding algorithm [51] was applied to the unenhanced images. This algorithm also allows for removing air from lungs and other low intensity areas. Because of the high intensity noise, the Otsu thresholding algorithm may generate areas in the external air. To remove these areas, the largest connected region, i.e. the breasts,

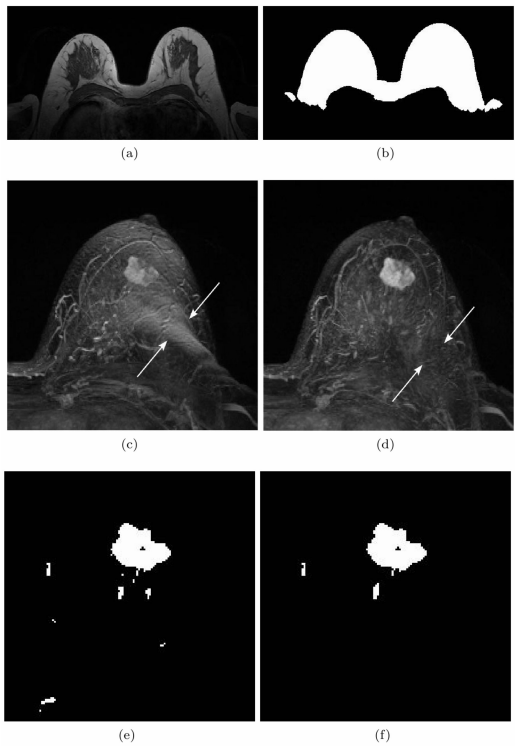

Figure 6.1. *Main steps for breast segmentation and lesion detection for a non-fat-sat study. The unenhanced frame is shown in (a); the mask resulting from breast segmentation is shown in (b). In (c) the maximum intensity projection (MIP) along the z axis of the second enhanced subtracted frame is shown before registration: subtraction artifacts due to patient movement are visible as spurious enhancing voxels (arrows). In (d) the same subtracted MIP after registration is shown: motion artifacts have been removed (arrows). In (e) the results of automatic lesion detection are shown, while in (f) the segmentation results after false positive reduction by means of morphological and kinetic criteria are illustrated.*

was selected by the algorithm and morphological operations were then applied to fill holes (six dilations and six erosions, both using a 5×5×5 kernel). The algorithm then searches for the maximum point, as previously defined, on the Otsu mask (Fig. 6.2(c)), and for the central line C, defined as the line running along the concavity between the breasts. Once the breasts size and location have been identified, breast segmentation itself can be done. This part of the algorithm is performed differently depending on whether fat-saturation was used, as determined automatically by the DICOM header.

6.1.1 Breast segmentation for non-fat-saturated images

The boundary between air and the breasts is easily detected by scanning each slice of the Otsu mask (Fig. 6.2(c)) along vertical lines starting from the anterior part of the image.

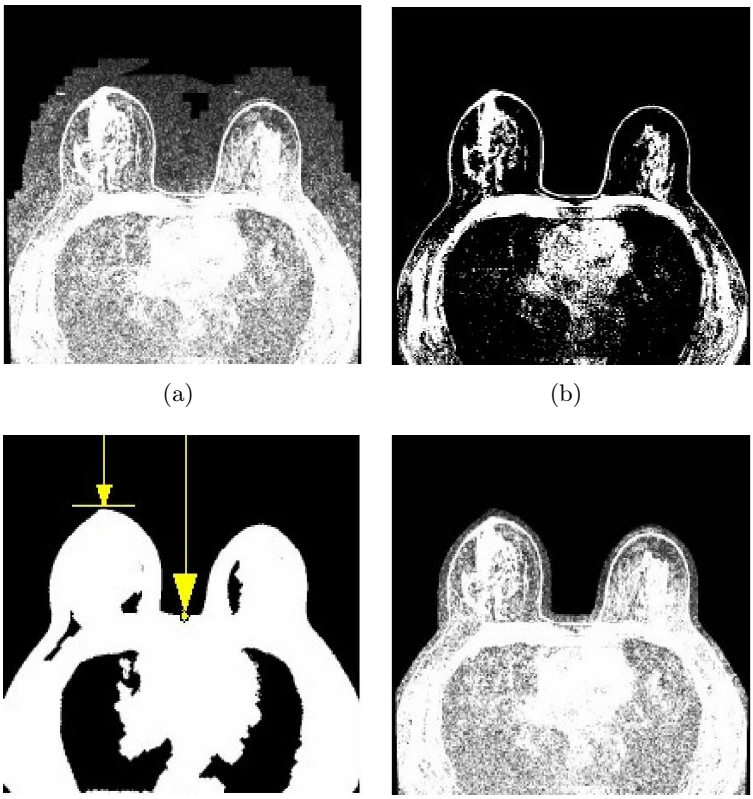

Figure 6.2. ***a)*** *pre-contrast image;* ***b)*** *result of Otsu's thresholding. The largest connected region comprises also the skin profile;* ***c)*** *result of morphological operations (6 dilations and 6 erosions, both with kernel 5×5×5). For each slice, every vertical line is scanned until the patient body is reached. The position of the central line and the breast's maximum point (shown by arrows) are identified;* ***d)*** *the mask obtained at step (c) is also used to remove external air from the pre-contrast image in order to suppress noise and artifacts in the external air.*

Then, to locate the breast-chest boundary we exploit the anatomical features of the pectoral muscle, which is located between the breasts and the chest wall. The average muscle intensity is lower than the fat within the breasts, but higher than the air in the lungs; therefore, it is characterized by a positive gradient along the border within the breasts fat tissue (denoted in the following as "upper border"), and a negative gradient at the chest wall border (denoted "lower border"in the following). As the pectoral muscle can be anatomically modeled as a smooth and thin slab of tissue, the approximate location of the upper border in the i-th slice can be estimated by placing a diagonal line passing from the i-th point of the central line, C_i, with a slope of 0.15 towards the right and -0.15 towards

the left [52]. Such diagonal lines will be used to bound the position of the actual upper border as described in the following (see Fig. 6.3). The upper and lower border is then located based on the image gradients.

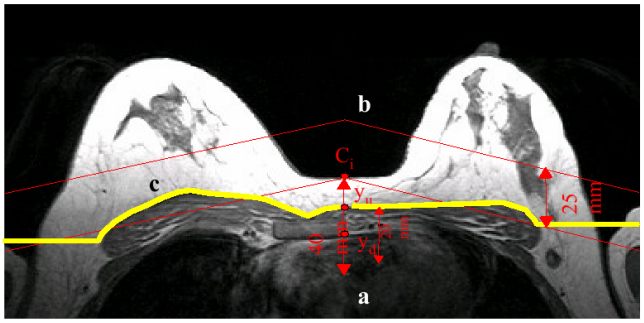

Figure 6.3. *Determination of the breast-muscle interface. (a) Identification of the initial seed points below the central line. (b) an upper bound is identified based on the diagonal lines passing by the central point with a ±0.15 slope âĂŞ no lower bound is imposed on the upper or lower border (c) the final upper border identified by the algorithm.*

The algorithm starts by locating for each slice i a couple of points $P^u(x, y^u)$ and $P^l(x, y^l)$ for each x in a limited interval of the x-coordinate of the i-th central line point $C_i(x_i, y_i)$. The set of P^u and P^l, identifying respectively the upper and lower border in the region around C_i, are located according to the flow-chart shown in Fig. 6.4 (Output 1). However, in some cases errors could arise, for instance due to inhomogeneities in the magnetic field. As P^u and P^l are used as seeds in the second part of the algorithm, it is of paramount importance that they are correctly located to avoid propagating errors. Step 2 in the flow-chart identifies erroneous voxels, based on the hypothesis that the upper boundary is very smooth and hence the distance Δy^u should be very small, whereas Step 3 searches for a new suitable couple of points (see flow-chart in Fig. 6.4). The whole upper and lower border profiles are then completed for all x-coordinates according to the procedure reported in the dashed-box of the flow-chart in Fig. 6.4. In this part of the algorithm the upper bound is also determined based on the position of the diagonal line, i.e. $y^u(x_j) < d(x_j) + 25$ mm; this prevents the contour from being attracted to the gradient between the gland and fat, in cases where the gland is very close to the pectoral muscle. The whole procedure is repeated for all the slices of the images, with an additional control for the position of the boundary in the corresponding x_j in the previous slice: the distance between $y^u(x_j)_{sliceN}$ and $y^u(x_j)_{sliceN-1}$ should be less than 2.25. In order to obtain a

closed contour even in regions where the pectoral muscle is not present, i.e. arms, if the algorithm does not find a gradient magnitude greater than T_g, $P^u(y^u(x_j))$ and $P^l(y^l(x_j))$ are set as $P^u(y^u(x_j - 1))$ and $P^l(y^l(x_j - 1))$.

As both the position of the breast-air and the upper border of the pectoral muscle are determined as a function of the x coordinate, the final segmentation can be obtained by including all voxels between the two contours. The obtained mask is then refined with a morphological closing, with kernel 2.5x2.5x2.5 mm.
This algorithm was tested on DCE-MRI cases from two different centers, with different acquisition modalities, and evaluated by quantitative comparison with a manual segmentation, performed by two operators. Overlap, recall, that is a statistical measure of underestimation of the segmented volume, precision, that is an index of overestimation of the segmented volume, and mean surface distance between the segmentation and reference contours were computed. Overall results of this segmentation method were 0.79 ± 0.09 (mean Âś SD) for overlap, 0.95± 0.02 for recall, 0.82± 0.1 for precision, and 6.3± 3.93 voxels for mean surface distance. The 95% of recall is very satisfactory, indicating that most of the manually segmented regions are included in the segmentation, which is the most important issue as undersegmentation may exclude lesions during the lesion detection step.

6.1.2 Breast segmentation for fat-saturated images

If fat-sat is used, intensity alone is not sufficient to obtain a reliable segmentation. In this case, an a priori knowledge of the main anatomical structures in the field of view was exploited, using an atlas-based segmentation scheme. A simplified atlas was used in which the breasts, heart, chest wall and lungs have been previously manually segmented and color-coded. Because breast size and shape may vary considerably across subjects, three different atlases were generated for large, medium and small breasts 6.7. The patient body was identified by the above mentioned Otsu's thresholding method, the image was down-sampled to a predefined resolution to reduce the computational burden, and then registered to the appropriate breast atlas, by a rigid and an elastic registration algorithm. Details of the registration algorithm used will be explained in Sec. 6.2. Two examples of breasts segmentation results are shown in Fig 6.8. The two methodologies yield slightly different results in the axillary area, but this is not compromising for the lesion detection. Axillae, supraclavicular fossae, chest wall, and anterior mediastinum can be assessed by breast MRI (e.g. to search for enlarged lymph nodes) but their evaluation could be omitted

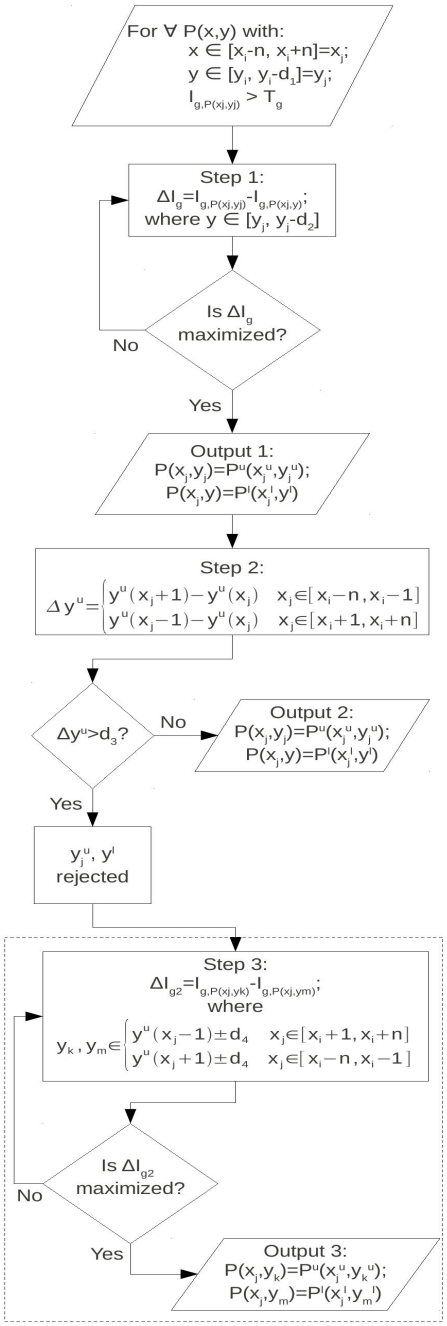

Figure 6.4. *Flow-chart of the procedure to find the upper and lower pectoral muscle border in the case of a single slice.* x_i, y_i *are the coordinates of the i-th point of the central line* $C_i(x_i, y_i)$. *n=5 pixels.* I_g *is the pixel gradient magnitude and* T_g *is the pixel gradient maximum threshold (*$T_g = 10$*).* $d_1 = 40mm$, $d_2 = 20mm$,$d_3 = 3mm$, $d_4 = 2.25mm$. *u and l apexes indicate respectively upper and lower border. The dashed-box encloses the procedure needed to complete the upper and lower borders for pixels out of the central line interval.*

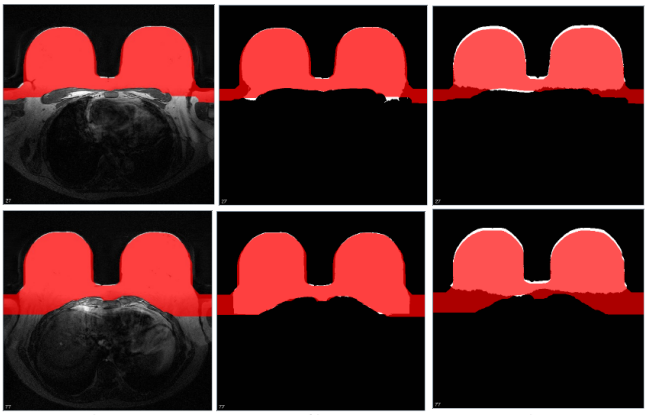

Figure 6.5. *Results for two slices from one patient. Note the drop in signal intensity away from the breasts coil. a) Automatic segmentation superimposed to the unenhanced image. b) Automatic segmentation superimposed to the manual segmentation. c) Automatic segmentation superimposed to the thresholding-based automatic segmentation method.*

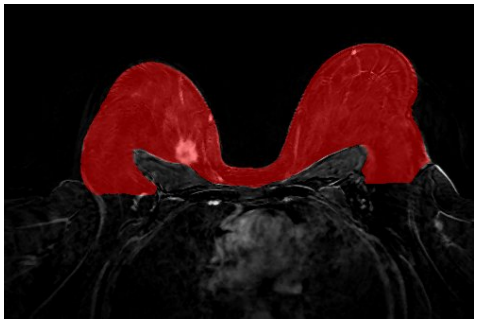

Figure 6.6. *Segmentation results in the case of a tumor very close to the pectoral muscle interface.*

as there is no evidence of its diagnostic value [50].

6.2 Registration

The first step performed by a CAD system is the registration between images coming from different datasets or acquired in different moments. During the DCE-MRI exam, for example, six 3D images are acquired in around ten minutes. During this period the patient undergoes involuntary (breathing, heart beating) and voluntary movements. In the developed CAD system the registration between DCE-MRI volumes of the same patient is performed.

The registration method, illustrated in Fig. 6.9, is based on the method proposed by

(a) (b) (c)

Figure 6.7. *Breast atlases corresponding to different breasts' size.* ***a)*** *Model for patients with "large"breasts (estimated breast size > 10 cm);* ***b)*** *model for patients with "medium"breasts (estimated breast size < 10 cm and > 7 cm) and* ***c)*** *model for patients with "small"breasts (estimated breast size < 7 cm). The represented anatomical regions are, from brightest to darkest area: thoracic wall, breasts, hearth and chest wall.*

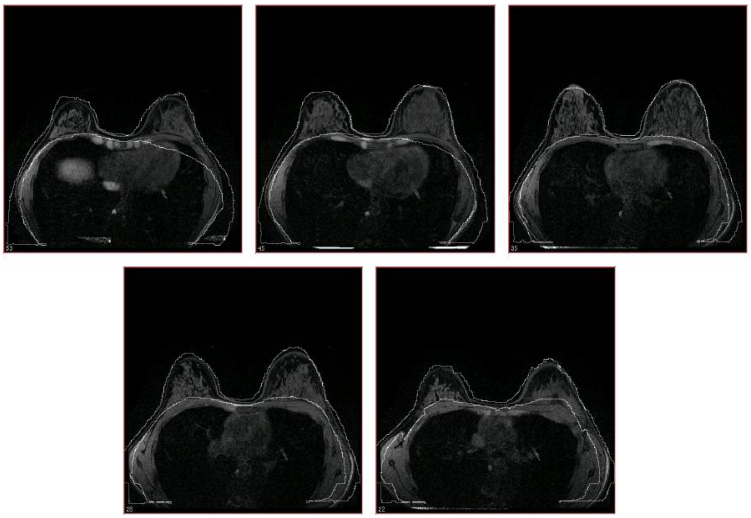

Figure 6.8. *Example of breast segmentation for studies acquired with fat-saturation (different slices of the same patient are shown). The breast masks extends further than in non-fat-suppressed sequences, as defined by the breast atlas. The breast model was not deformed in the bottom part of the image, as only a smaller ROI is taken into account by breast segmentation.*

Rueckert [54], and was implemented using the insight toolkit (itk) [55] libraries based on C++ language. To reduce the computational burden, the registration was performed at a minimal predefined resolution in each axis direction. Therefore, if the frames of the dynamic series presented a lower resolution in any of the directions, the images were down-sampled to the predefined minimal resolution. Otherwise, registration was performed at original resolution. In addition, the registration was performed within a rectangular

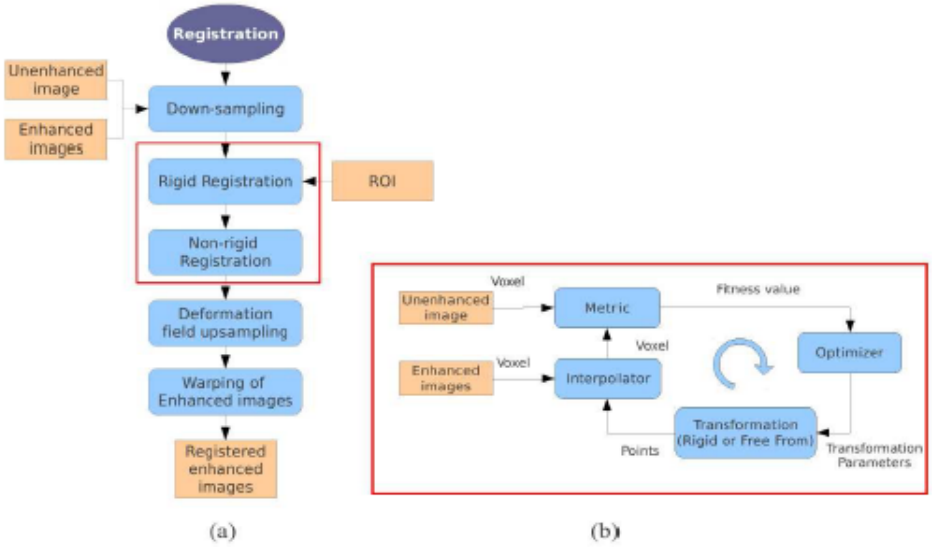

Figure 6.9. (a) Scheme of the registration method. (b) Basic components of the registration framework used for the rigid and non-rigid registration steps.

region of interest, containing the relevant part of the scans for the diagnosis (i.e. breasts and axillae), which was automatically determined based on the maximum and minimum points of the breast (as defined in section 6.1). The registration itself consists of two main steps. First, the global misalignment was compensated by using a translation and a rigid-body transformation. Subsequently, local motion was corrected by a free-form deformation model based on B-splines [54]. The second step is necessary being the breast a deformable tissue. In fact, even if the patients lays prone and the breasts are placed into the coil, a small movement of the patient's body can produce an elastic deformation on the breasts. Image registration, rigid or free-form, can be considered as trying to maximize the amount of shared information between two images, while reducing the amount of information in the combined image, which suggests the use of a measure of information as a registration metric [58]. Many metric have been presented in literature (i.e. correlation coefficient, sum of the absolute difference), however this method may not take into account the difference due to the amount of contrast agent during the dynamic acquisition, when the intensity value of the pixel might change from one image to the other. The mutual information metric, vice versa, is a measure of statistical dependency between two datasets, and is given by

$$MI(X,Y) = H(Y) - H(Y \mid X) = H(X) - H(Y) - H(X,Y), \tag{6.1}$$

where X and Y are two random variables, $H(X) = -E_x(log(P(X)))$ represents entropy of a random variable and $P(X)$ is the probability distribution of X. The method is based of the maximization of the MI, in particular by the method specified by Mattes et al [56]. Finding the maximum of similarity measure is a multidimensional optimization problem, that requires an iterative approach, in which an initial estimate of the transformation is gradually refined by trial and error. In each iteration the current estimate of the transformation is used to calculate a similarity measure. The optimization algorithm then makes another (hopefully better) estimate of the transformation, evaluates the similarity measure again, and continues until the algorithm converges, at which point no transformation can be found that results in a better value of the similarity measure, to within a preset tolerance. One of the difficulties with optimization algorithms is that they can converge to an incorrect solution called a "local optimum". In this CAD system, different optimizer have been tested, but the most suitable were found to be the gradient descent optimizer for the rigid registrations, and of the LBFGSB (Limited memory - Broyden, Fletcher, Goldfarb, and Shannon - for Bound constrained optimization) optimizer for the nonrigid sub-step [57]. If the contrast-enhanced frames were down-sampled before the registration, the respective deformation fields were up-sampled to the original resolution. Finally, the original contrast-enhanced frames were warped to obtain the transformed (aligned) contrast-enhanced frames by applying the respective deformation field. In the warping, B-spline interpolation was used to minimize the introduction of sampling artifacts. The registration method was tested on 24 patients from the group B (non fat-sat images). Sixteen of 24 patients were randomly selected while the remaining 8 were added as they presented relevant artifacts due to patient movement. The registration method was applied to the enhanced sequences with reference to the unenhanced one. Registered (REG) and non-registered (N-REG) axial images and maximum intensity projections (MIPs) of the first enhanced subtracted frame were randomized and blindly evaluated by two radiologists separately by scrolling the axial images and rotating the MIPs, with free windowing. Image quality was assessed for both axial images and MIPs. Readers were asked to define equivalence or superiority of one of the two datasets of each patient, simultaneously presented. Finally, the CAD system performed the lesion detection step 6.3 identifying suspicious enhancements (prompts) for REG and N-REG images. A radiologists excluded prompts related to real findings; the remaining false prompts and their volume were obtained for both REG and N-REG images. Image quality of REG-MIPs was found to be significantly superior than that of N-REG-MIPs for both readers (p-value$<$0.001) with a

quite good inter-rater agreement (k=0.5). Image quality of REG-axial images was found to be slightly better than that of N-REG axial images by both readers without significant difference. The mean number of false prompts per patient was 29.4±17.7 on N-REG and 25.0±16.5 for REG (p-value=0.041). Excluding one patient with wrong segmentation of the heart, the mean volume of false prompts was 13,000±11,641 mm^3 for N-REG and only 4,345±4,274 mm^3 for REG (p-value<0.001). Two examples of how registration was able to compensate for motion artifacts is shown in Fig. 6.10 and Fig. 6.11.

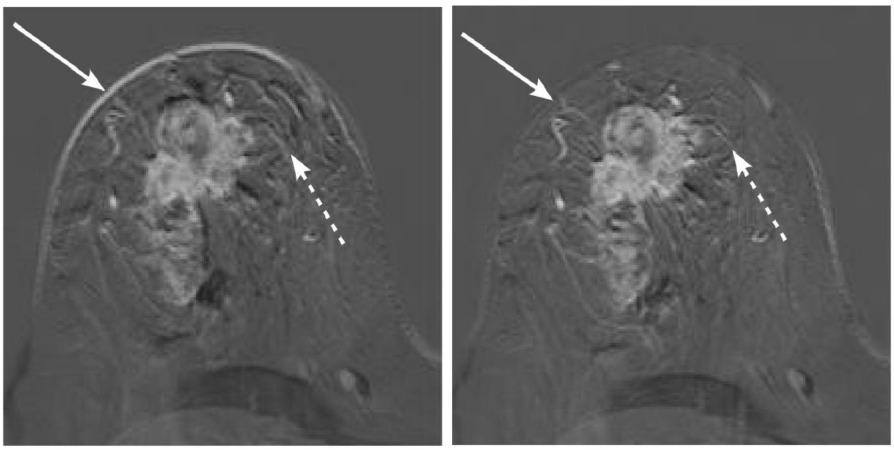

(a) (b)

Figure 6.10. Comparison between subtracted images with and without registration. A slice from a non-fat-sat examination is shown. (a) Subtraction artifacts due to patient movement are visible along the breast profile (plain arrow), in the breast parenchyma (dot arrow), at lesion and vessel borders, as well as at the borders of fat lobules. These artifacts may introduce spurious enhancing voxels, thus increasing the number of false positive findings at segmentation. (b) Subtraction artifacts are dramatically reduced when elastic registration is used.

6.3 Lesion detection

Contrast enhancement of breast lesions shows large physiologic variations, mostly depending on differences in vascular permeability [59, 60] and other technical and physiological parameters, including type and dose of contrast material [61, 62]. Differences may depend on lesion histology, on the timing of imaging or on inhomogeneities within the lesions, such as those observed in necrotic areas or in fibrosis. To take into account for the nonuniform uptake of contrast, while reducing at the same time the computational burden associated with the processing of all the contrast-enhanced registered frames, we used the subtracted

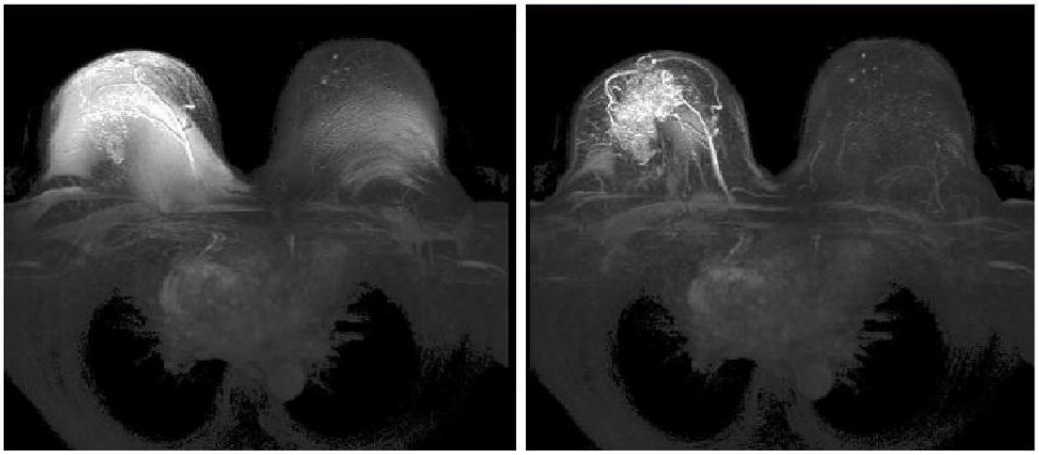

Figure 6.11. Comparison of non-registered (a) and registered (b) MIPs. The image quality is significantly superior in registered images (in N-REG images the motion artifacts introduce spurious enhancing voxels).

mean intensity projection image over time (mIPT). Being the dynamic sequence a 4D image (x×y×z×t), where t is time, the mIPT is the 3D image (x×y×z) formed by averaging each voxel along the t axis. Subtraction of the unenhanced frame was performed to neglect the contribution of regions which do not show contrast enhancement. Different scanners, coils, acquisition modalities, types and amounts of contrast agent injected, patients's physiology, and other external factors, result in significant variations of image intensities among images acquired in different hospitals, in different patients, or even among different examinations from the same patient [61, 62].

To compensate for these effects, the subtracted mIPT was normalized by contrast enhancement of the mammary vessels. Because the mammary vessels show maximum contrast enhancement in the early frames of the dynamic sequence, they were automatically segmented on the first subtracted contrast-enhanced frame. A suitable ROI was automatically selected based on the position of the central line by placing a rectangle of a fixed size (50 mm×100 mm) in each slice, with the exception of the upper 30% and lower 10% of the 3D image slices that were not considered because the mammary vessels are not usually visible. The mammary vessels were then identified by applying to the ROI the multiscale 3D Sato's vessel enhancement filter, which is based on the eigenvalues of the Hessian matrix [63, 64]. The Sato's vessel enhancement filter considers the mutual magnitude of the eigenvalues as indicative of the shape of the underlying object: isotropic structures are associated with

eigenvalues which have a similar nonzero magnitude, while vessels present one negligible and two similar nonzero eigenvalues. Let the eigenvalues of the Hessian matrix be λ_1, λ_2, λ_3 (with $\lambda_1 > \lambda_2 > \lambda_3$). On a given scale, vesselness is thus defined as:

$$V_\sigma(\lambda_1, \lambda_c) = \begin{cases} e^{-\frac{\lambda_1^2}{2(\alpha_1 \lambda_c)^2}} & \lambda_1 \leq 0, \lambda_c \neq 0 \\ e^{-\frac{\lambda_1^2}{2(\alpha_2 \lambda_c)^2}} & \lambda_1 > 0, \lambda_c \neq 0 \\ 0 & \lambda_c = 0 \end{cases} \tag{6.2}$$

where λ_c min (λ_2, λ_3), α_1 and α_2 were set to 0.5. The s footer in V_s indicates that the vesselness is computed on a smoothed version of the image and is therefore representative of the variations of image intensity on the s spatial scale. As vessels in the breasts could have different diameters, the vesselness is evaluated on a range of spatial scales, and the highest response is selected for each voxel. Specifically, the vesselness response is computed at 6 exponentially distributed scales between the maximum and minimum scales $\sigma_{min} = 0.5$ and $s_{max} = 1.0$. The most vessel-like voxels are then selected by applying a threshold equal to half the maximum vesselness value observed in the region of interest identified as described above; in Fig. 6.12 the 3D view of an example of segmented mammary vessels is shown. The

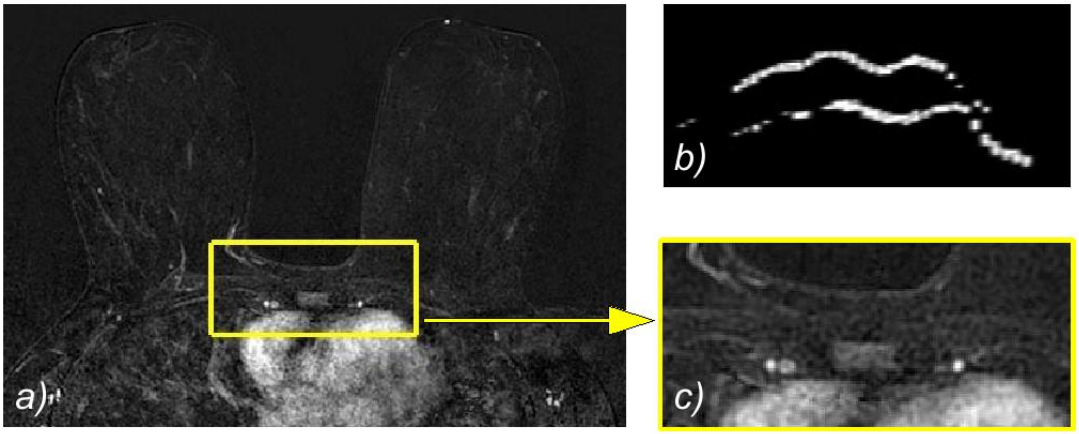

Figure 6.12. ***a)*** *Subtracted first post-contrast frame with the region where the mammary vessels are located in yellow.* ***b)*** *Zoom of the region highlighted in a).* ***c)*** *3D view of segmented mammary vessels.*

normalization factor was calculated as the mean contrast enhancement of the mammary vessel voxels in the first contrast-enhanced frame. After normalizing the subtracted mean intensity projection, regions showing contrast enhancement were extracted. Even if the

contrast-enhanced frames were normalized, we have found that a fixed threshold was not suitable to successfully segment lesions on all scans. At this step non-enhancing regions have been removed by the subtraction with the pre-contrast frame and, when present, by fat-saturation; therefore, the image histogram (in the breast and axillary regions) has a peak around zero and the intensities of enhancing regions are located in the histogram tail (Fig. 6.13). We combined the mean value, that is as closer to zero as many non-enhancing areas are discarded by subtraction and fat-saturation, and the maximum value. In particular, the maximum value is related to the maximum contrast uptake in the image and it is chosen as the maximum value with a frequency of number of voxels at least corresponding to 2 mm^3 volume, thus avoiding to consider hyper-intense isolated voxels due to noise or artifacts.
So, the global threshold T_I was determined as:

$$T_I = mean_I + \frac{max_I}{3}, \tag{6.3}$$

where $mean_I$ is the mean value of the normalized intensity histogram of the breast and axillary region and max_I is the maximum intensity value observed in the same region.
Because lesions are often connected to feeding vessels, they are often segmented together. To prevent lesion oversegmentation, which could reduce the diagnostic quality of the segmentation and limit the performance of segmentation-based CAD applications, voxels belonging to vessels were excluded from lesion detection. For each voxel, the eigenvalues of the covariance matrix were extracted, and the ratio between the highest and medium eigenvalues was used as a vesselness measure. Voxels with a ratio larger than a fixed threshold T_v (where $T_v = 10$) were labeled as vessels and excluded from lesion detection. Connected components were then extracted from the resulting mask (see Fig. 6.14. Connected components were then extracted from the resulting mask.

6.3.1 False positive reduction

The regions showing contrast uptake include not only lesions (benign and malignant), but also false positives such as skin, motion artifacts and noise.
A few heuristic criteria are applied in order to discard false positives.
First, regions with volume less than 20 mm^3 are excluded; this roughly corresponds to a lesion of 5 mm diameter, which is the cutoff for clinically relevant lesions, taking also into account image resolution and possible lesion under-segmentation.
As reported in section 5.1, contrast-enhancement kinetics can be classified as curves I,

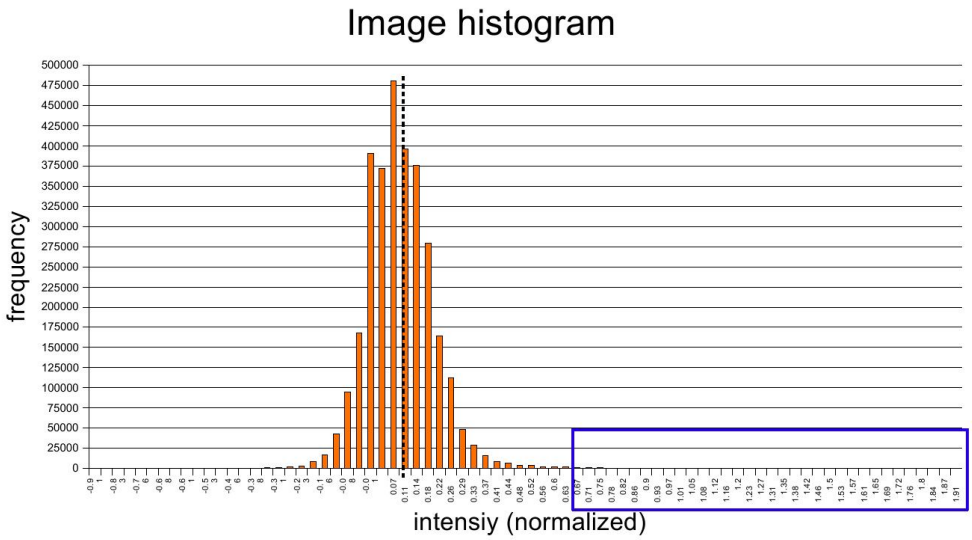

(a)

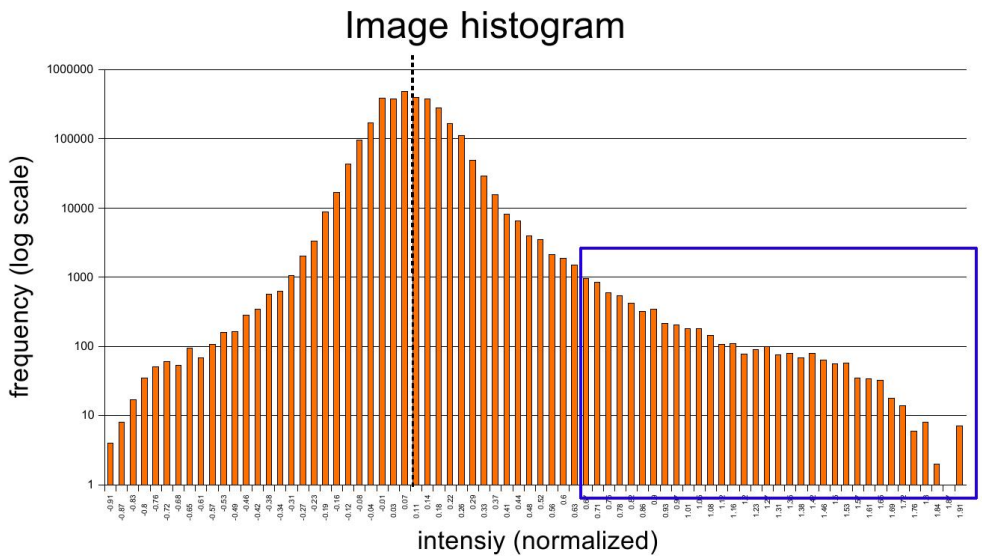

(b)

Figure 6.13. *Histogram* (a) *and log scale histogram* (b) *of the subtracted and normalized mean intensity projection (breast and axillary regions) in the case of a study acquired without fat-saturation. The dashed vertical line represents the mean value of the histogram, while the blue rectangle identifies the intensity range of contrast-enhancing regions.*

II and III with an increasing probability of malignancy (6%, 64%, and 87%, respectively) [48]. However, these curves are referred only to individual voxels or set of contiguous voxels

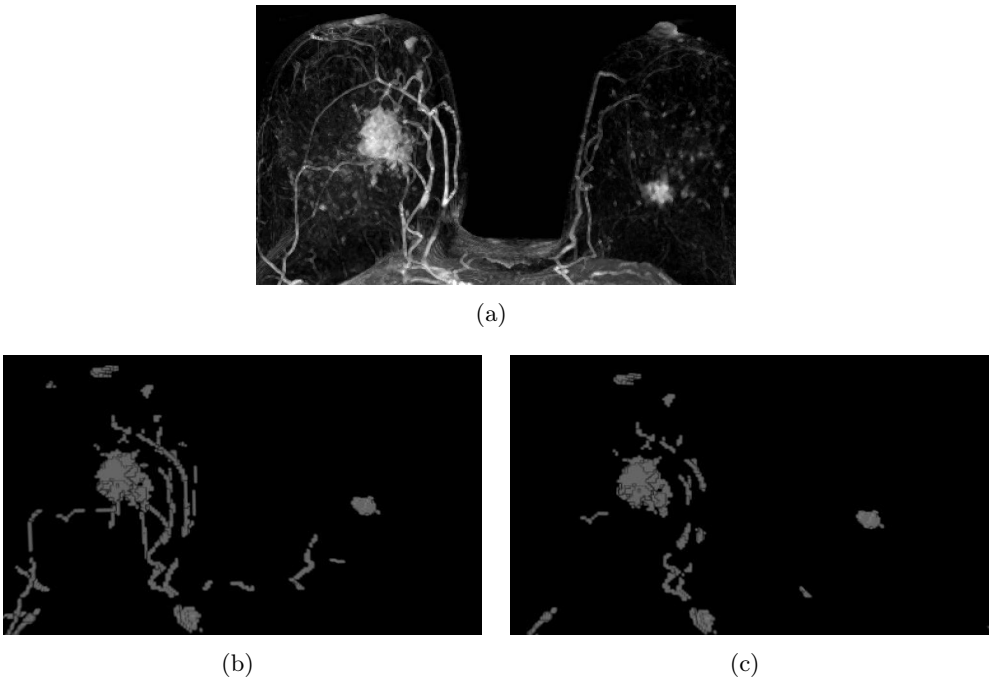

(a) (b) (c)

Figure 6.14. (a) *Maximum intensity projection of the second post-contrast subtracted frame, in the case of a study acquired with fat-saturation.* (b) *3D view of the mask obtained after thresholding the normalized subtracted mean intensity projection.* (c) *3D view of the same mask shown in (b), after application of the vessel detection step based on the eigenvalues of the covariance matrix. Many structures have been recognized as vessels and discarded, in particular vessels connected to the lesion.*

(typically formed by a few voxels) belonging to a single part of tissue having uniform vascular characteristics, and thus having homogeneous contrast-enhancement. In particular, we defined an homogeneity parameter as:

$$H = \frac{\text{image intensity standard deviation}}{\text{mean image intensity}}, \tag{6.4}$$

and we found that it could be used to discriminate tissues having ($H < 0.02$) or not having ($H > 0.02$) uniform vascular characteristics.

On the other hand, the average intensity curve calculated over an entire lesion (typically not having homogeneous vascular characteristics) is generally more similar to the average signal intensity curve shown in Fig. 6.15.

Thus, our aim was to identify trends which are indicative of structures other than benign and malignant lesions, such for example noise, artifacts or vessels. Empirically, some simple kinetic features were found to identify trends different from lesions, but rather typical of vessels or artifacts, as shown in Fig. 6.15.

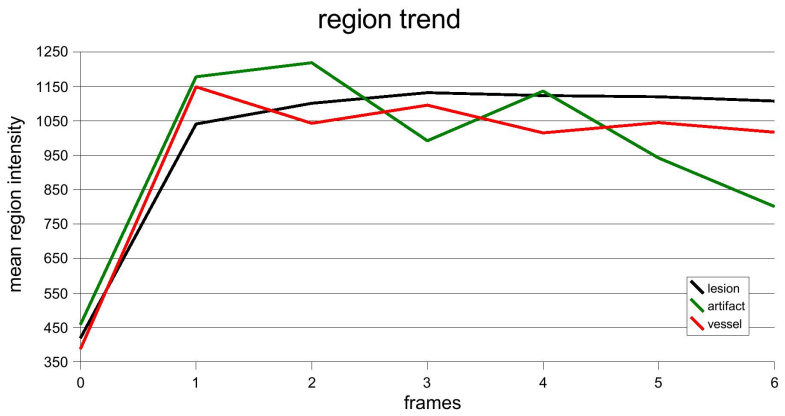

Figure 6.15. *Mean intensity curves calculated over an entire connected component in the case of a lesion (black), a vessel (red) and an artifact (green).*

For instance, artifacts due to noise and patient motion are usually characterized by high signal variations; hence, regions with standard deviation of image intensity greater than 150, or with a higher-than-10% decrease or increase in signal intensity in the last frame, with respect to the second-last frame, were discarded.
Furthermore, regions with mean intensity decreasing from the first to the second frame are discarded as this pattern was found present in vessels but not in lesions.

6.4 Results

6.4.1 Statistical analysis

The results of the registration and breast segmentation steps were visually inspected by a radiologist with more than 4 years of experience in breast MRI. The radiologist labeled a finding as a true positive if the lesion was confirmed at histology or at follow-up, otherwise it was defined as a FP. Detection rate was calculated as the number of true positives (both malignant and benign) over the total number of lesions as defined at the reference standard, whereas sensitivity was calculated as the number of malignant lesions detected by the system over the total number of malignant lesions. Lesions were grouped according to size as follows: from 5 to 10 mm, 11 to 20 mm, and larger than 20 mm [65] and detection rate and sensitivity were calculated for each group. Sensitivity and detection rate values are presented with 95% confidence intervals (CIs) using the Wilson method for

single proportions. Detection rate and sensitivity were also separately calculated for fat-sat and non-fat-sat exams, and the χ^2 test was used to assess differences between the two subgroups. The detection rate of the system for lesions satellite to index cancers detected by radiologists for which a lesion-by-lesion pathological analysis was not reported, was analyzed separately. FP findings were defined by the radiologist as mammary or extra-mammary findings, and characterized either as vessels, image artifacts (i.e., skin, chemical shift, patient movements, etc), lymph nodes, normal gland or other findings (i.e., nipple, pectoral muscle, heart, etc). The FP median, 1st and 3rd quartiles were calculated for the entire testing set, for the fat-sat and non-fat-sat subgroups. A two-sided Kruskal Wallis test was applied to test for differences between the medians for the total number of FP/patient. A P-level lower than 0.05 was considered statistically significant.

6.4.2 Results

Algorithm performance was evaluated on a dataset of 48 DCE-MRI studies performed on women with suspicion of breast cancer based on conventional imaging. Relevant demographic, clinical and technical information on the dataset is shown in the flow chart in Fig.5.4. The median of the largest diameter of benign and malignant lesions was, respectively, 6 mm (range, 5-15 mm) and 26 mm (range, 5-75 mm). Overall, there were 16 lesions sized 10 mm or less, 15 lesions between 11 and 20 mm, and 34 lesions sized larger than 20 mm. The automatic algorithm detected 58 of the 65 lesions (89% detection rate; 95% CI 79-95%), including 52 of the 53 malignant lesions (98% sensitivity; 95% CI 90-99%). Detection rate and sensitivity according to lesion size are shown in Table 6.1. In the fat-sat

Table 6.1. *Number of Lesions and Performance for Each Dimension Group. Lesions were grouped according to the National Cancer Institute. Detection rate and sensitivity were calculated with a 95% confidence interval.*

Lesion Dimension (mm)	# Malignant	# Benign	# Total	Detection Rate (Upper-Lower Limits; 95% CI)	Sensitivity (Upper-Lower Limits; 95% CI)
5-10	6	10	16	69% (44%-86%)	100% (61%-100%)
11-20	13	2	15	87% (62%-96%)	92% (67%-99%)
>20	34	0	34	100% (90%-100%)	100% (90%-100%)
Total	**53**	**12**	**65**	**89% (79%-95%)**	**98% (90%-99%)**

subgroup, 20 of the 25 lesions (80% detection rate; 95% CI 61-91%) were detected, including 19 of the 20 malignant lesions (95% sensitivity; 95% CI 76-99%). In the non-fat-sat subgroup, 38 of the 40 lesions (95% detection rate; 95% CI 84-99%) were detected, including all 33 malignant lesions (100% sensitivity; 95% CI 90-100%). Differences in sensitivity and detection rate between the two groups were not statistically significant (P=0.798 and P=0.137 respectively).

A total of 7 lesions with an average size of 7±3 mm (mean±SD) were missed by the algorithm, including 6 benign and 1 malignant nodules. Five of the undetected lesions were in dataset A including: 2 fibroadenomas, 2 small enhancements with a negative MRI follow-up of 5 and a 7 mm in size, respectively, and a 12-mm invasive ductal carcinoma. Missed lesions in dataset B were two 5 mm small enhancements unchanged at MRI follow-up. Examples of lesions detected and missed by the system are shown in Figure 6.16. In addition to malignant lesions histologically confirmed as a result of a lesion-by-lesion analysis in the pathological report, 17 lesions satellite to malignant index lesions, with a median diameter of 7 mm (range, 5-20 mm) were detected by two radiologists. Sixteen of them (94%) were detected by the system. Median mammary FPs per breast were 4 (1stâĂŞ3rd quartiles 3-7.25), while median extra-mammary FPs per study were 2 (1st-3rd quartiles 1-5). Table 6.2 shows the distribution of findings according to the type. For the fat-sat subgroup, median mammary FPs per breast were 4 (1st-3rd quartiles 2-7.25); median extra-mammary FPs per study were also 4 (1st-3rd quartiles 3-6). In the non-fat-sat group, median mammary FPs per breast were 4.5 (1st-3rd quartiles 3.5-7), while median extra-mammary FPs per study were 1 (1st-3rd quartiles 1-2). No statistical significant differences were detected between the two subgroups (P=0.72).

Average execution time was 5m48s for the non-fat-sat group and 8m48s for the fat-sat

Table 6.2. *Classification of FP findings according to the type.*

Type	#	%
vessels	267	54
artifacts*	113	23
gland	80	16
lymph nodes	2	0.4
other°	32	6

* i.e. chemical shift, skin, patient movements.
°i.e. nipple, pectoral muscle.

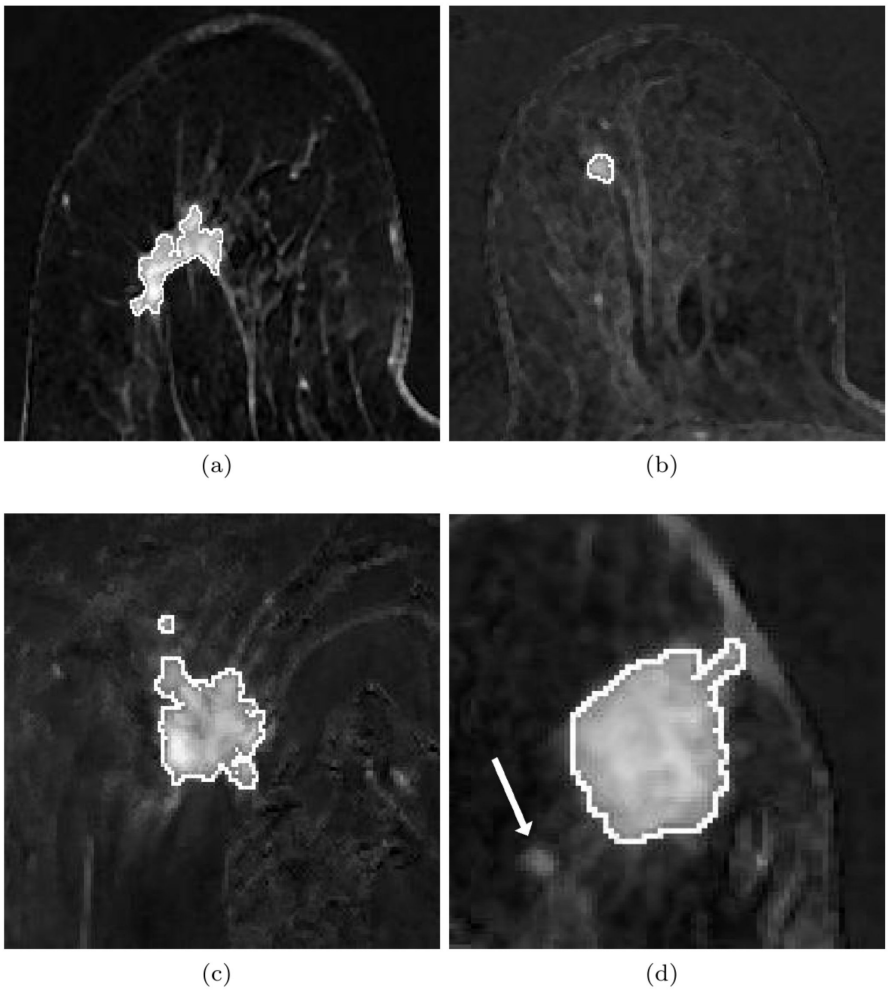

Figure 6.16. *Examples of segmentation results, superimposed on the normalized and subtracted mean projection over time. (a) A 33-mm invasive ductal carcinoma (fat-sat image) correctly segmented; (b) a 7-mm invasive ductal carcinoma (fat-sat image) correctly segmented; (c) a 26-mm invasive ductal carcinoma (non-fat-sat image) correctly segmented; (d) a 25-mm invasive ductal carcinoma (fat-sat image) correctly segmented; here a 5-mm satellite lesion (arrow) was missed by the system.*

group. Execution time was measured on a computer equipped with a CPU Intel Core i7 940 Quad Core @#2.93GHz architecture and 8 GBytes RAM.

Chapter 7

Breast lesion discrimination

Lesion discrimination is a diagnostic stage in the CAD pipeline dedicated to recognize the level of malignancy of previously detected lesions. Breast DCE-MRI allows to depict differences between malignant and benign lesions according to morphological and contrast-enhancement kinetics features of lesions. Morphological attributes such as irregular or spiculated margins, irregular shapes, heterogeneous and peripheral internal contrast enhancement are important indicators of malignancy [72]. Signal-to-time curves with rapid decreasing of signal intensity after peak enhancement, reached approximately 2 or 3 minutes after contrast injection, are more frequently found in malignant lesions, whereas benign lesions have typically slow persistent enhancement increase [72]. Figure 7.1 shows an example of a malignant lesion with irregular margins and heterogeneous internal enhancement and a benign lesion with regular margins and homogeneous internal enhancement. Clinical interpretation of the kinetic and morphological properties is subjective and qualitative, therefore several studies have proposed computer assisted approaches. Gihuijs et al. [73, 74] extracted morphological and kinetic features from lesions segmented manually or semi-automatically after manual indication of a seed point and used linear discriminant analysis and step-wise selection to select the best subset of features. Gibbs et al. [75] applied texture analysis based on Haralick features and used logistic regression analysis with backwards elimination method to select the most discriminating subset of texture features. Gal et al.[76] compared different classifiers (logistic regression, linear discriminant analysis, bayesian and support vector machine) combining kinetic and morphological features, and using an exhaustive search to select the best features.

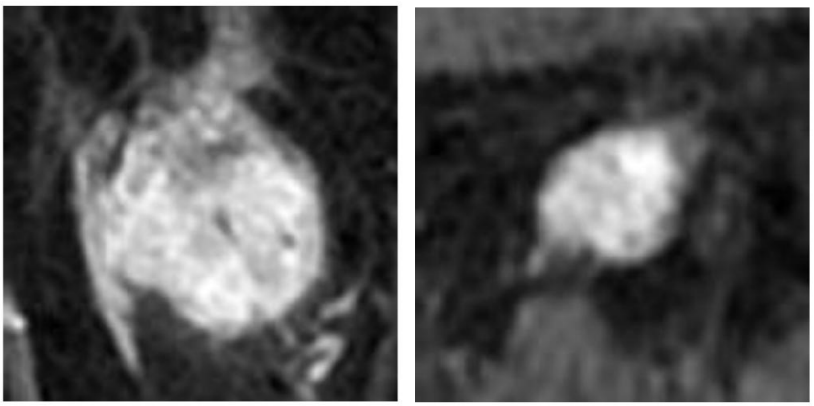

Figure 7.1. *Examples of a malignant Invasive Ductal Carcinoma (IDC) (a) and benign fibroadenoma (FAD) (b) breast lesions.*

In the following a multiparametric model is presented, which combines a selection of morphological and kinetic features for discriminating malignant from benign mass-like breast lesions at DCE-MRI [77]. Original features are introduced and combined with features already presented in literature, with the aim of trying a different approach. Model selection is performed by a genetic search [78] and a wrapper approach [79] using a support vector regressor.

7.1 Methods

To validate the method, 73 mass-like lesions were retrospectively used. Lesions were detected in 51 exams acquired at two centers at 1.5 T with MRI protocols described in 5.4 and confirmed by histopathology (54 malignant and 19 benign). Lesions were automatically segmented after image normalization and elastic registration of contrast-enhanced frames, as described in the previous steps, and then selected by two experienced radiologists in order to exclude non mass-like lesions or blood vessels. Lesion size was 13±8.4 mm (mean±standard deviation) for benign lesions and 16.1±14.7 mm) for malignant lesions, with lesion size determined as the longest diameter measured by radiologists. 33 lesions had a size smaller than 10 mm (22 malignant, 11 benign), whereas 40 lesions had a size larger than 10 mm (32 malignant, 8 benign). Table 7.1 summaries lesions histology. For each lesion, a set of 19 features were automatically extracted: 10 morphological features, related to shape, margins, and internal contrast-enhancement distribution, and 9 kinetic

Table 7.1. *Histological types for the 73 lesions included in the dataset.*

Malignant Lesions		**Benign Lesions**	
Invasive ductal carcinoma (IDC)	36		
Invasive lobular carcinoma(ILC)	4	Fibroadenoma (FAD)	9
Ductal carcinoma in-situ (DCIS)	4	Papilloma	4
Mixed Invasive Carcinoma	10	Other benign lesions	6
Total	**54**	**Total**	**19**

features computed from signal-to-time intensity curves. Two morphological features related to the lesion shape are calculated on the binary mask: circularity [73] and convex index [80]. Three features are used to describe the margin of a lesion: irregularity [73], mean and standard deviation of angles between surface normals ((mean(ABSN), std(ABSN)) [81]. Other five features characterizing the internal enhancement pattern are extracted: the autocorrelation function (evaluated at 2mm displacement), two features related to the peripheral uptake and the mean and standard deviation of the shape index(SI)47 computed inside the segmented mass. Enhancement kinetics features are used to characterize the time course of signal intensity through the contrast enhancement defined as:

$$C(\mathbf{r},j) = \frac{S(\mathbf{r},j) - S(\mathbf{r},0)}{S(\mathbf{r},0)} \quad j = 1,..,N \qquad (N = \frac{5}{6}) \tag{7.1}$$

where $S(\mathbf{r},i)$ is the intensity at voxel location r at time frame i and it is normalized to the contrast enhancement of mammary vessels. Two types of features are derived from the contrast enhancement. The first type is related to the fitting of the contrast enhancement to the following analytical exponential function:

$$C = At\exp(-t^D) \tag{7.2}$$

where the coefficients A and D control the function amplitude and decay, respectively. These coefficients characterize therefore the contrast uptake and washout inside the lesion. The lesion uptake and washout of contrast material were characterized by fitting the contrast enhancement $C(\mathbf{r},i)$ with an analytical function rather than using a two-compartmental pharmaco-kinetic model [83]. The use of a pharmaco-kinetic model implies strict constrains in the acquisition protocols [84], that were not fulfilled in the acquisition of many clinical datasets. Although, the analytical function proposed (Eqn. 7.2) cannot model physiologically the lesion, its simple form allows for relaxing constrains on the acquisition protocols still characterizing the kinetic behavior of the lesion.

The second type of feature computes the area under the contrast enhancement curve $C(\mathbf{r}, t)$, AUCEC. This feature is related to the total amount of contrast material in the lesion tissue. The mean, standard deviation and entropy were computed in the lesion segmented volume, yielding a total of 9 contrast enhancement kinetic features.

A support vector machine (SVM) was trained with feature subsets selected by a genetic search. Best subsets were composed of the most frequent features selected by majority rule. The performance was measured by receiver operator characteristics (ROC) analysis with the 10-fold cross-validation method that prevents optimistically biased evaluations due to overfitting. The bootstrap technique was used in order to estimate the confidence interval of area under ROC (AUC) and to compare the classification performances of the different features subsets. A Wilcoxon matched pairs one-tailed test was also performed to determine the significance level of the performance improvement.

7.2 Results

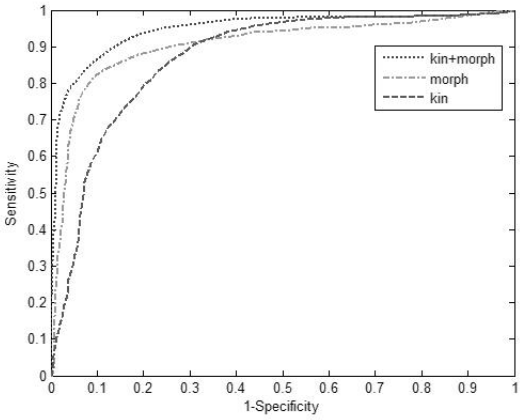

Figure 7.2. *ROC curves associated to the feature subsets selected in separated genetic searches for each class of features and to the features subset selected by the genetic search using all two classes of features.*

Figure 7.2 shows the mean ROC curves related to the feature subsets selected in separated genetic searches for each class of features and to the features subset selected by the genetic search using both classes of features. The AUC obtained in the three genetic searches were 0.90±0.06 (mean±standard deviation) for the morphological features subset, 0.87±0.06 for the kinetic features subset, and 0.94±0.03 with the combined feature subset. The AUC resulted from the combined feature subset was significantly higher (p-value

< 0.01) than those obtained with the other feature subsets, showing that the combination of features increases the classification performances. Three morphological features (mean(ABSN), std(ABSN), peripheralUptake) and three kinetic features (mean(D), entropy(D), entropy(A)) were selected in separated genetic searches for each feature class. Four features (mean(ABSN), std(SI), mean(D), mean(AUCEC)) were selected from the combined use all two classes of features.

Chapter 8

Conclusions

The fully automatic algorithm we developed for breast lesions detection and characterization in DCE-MRI has a high performance and is versatile as it can be used with different equipment and acquisition modes.

The lesion detection system achieved a sensitivity of 98%, with an acceptable number of FP findings. Moreover, the good performances obtained in detecting satellite lesions (16 of 17 were identified) highlights the system's potential in helping the detection of multifocal and multicentric breast cancers.

Fully automatic lesion detection has the potential of reducing inter- and intra-observer variability and reading time [42, 43, 44]. However, few methods have been developed to date to detect breast lesions automatically with DCE-MRI. Ertaş et al developed an automatic algorithm for the detection of breast lesions based on cellular neural network segmentation and 3D template matching [45]. They assessed the performance of their system on a dataset of 39 lesions, of which 19 were benign and 20 malignant. All MRI studies were performed with non-fat-sat sequences and they obtained a detection rate of 100% with less than one FP per study. An automatic lesion detection method based on support vector machine, proposed by Twellmann et al also showed promising results, yielding an area under the ROC curve of 0.98. However, the algorithm was tested on a limited dataset of 12 patients and only on non-fat-sat images [46]. The above mentioned methods cannot be applied to fat-sat images as normalization is performed by dividing each enhanced images by the unenhanced one. This process yields very noisy images if fat-sat is applied, as most of the breast signal is suppressed in the unenhanced frame. Moreover, Ertas et al applied a fixed threshold to extract suspicious areas and this may limit the applicability to studies

acquired with different protocols.

Our algorithm takes advantage of the following two innovative approaches. First, the normalization technique we proposed is based on the contrast enhancement of mammary vessels. Compared with normalization with respect to the unenhanced image, our approach gives stable results in the case of fat-sat images, as the obtained normalization factor is related to contrast agent administration. However, this method requires that DCE-MRI is performed on the axial plane, as the mammary vessels should be included in the field of view with an adequate spatial resolution. Second, we adopted the mIPT instead of the commonly used MIPT (maximum intensity projection over time), because it is less sensitive to noise and it produces more reliable segmentation. There are some limitations to our method. First, the detection was obtained using the mIPT and this process could underestimate lesion size, as late enhancing voxels and voxels with a rapid washout can be attenuated when averaging over time. For the step of malignancy discrimination, a more accurate identification of lesion boundary and morphology could be useful, and a further refinement of the lesion segmentation may become necessary. However, using the MIPT also has limitations. It affects the number of FPs negatively, as it is very sensitive to artifacts and noise, and may lead to overestimation of lesion size due to the "blooming sign"effect [66, 67, 68]. Second, our system has a higher number of FP findings if compared with other academic software and to commercially available solutions [69]. Most of our FPs are vessels, mainly tortuous vessels or bifurcations with low vesselness values. Detection of bifurcations is a known topological problem for vessel identification and tracking [70, 71]. Reduction of the number of FPs can conceivably be obtained by introducing a classification stage dedicated to the recognition of vessels, and more specifically of bifurcations. This stage is ongoing, and it consists in a fully automatic step to detect vessels in both fat-sat and non-fat-sat images. The algorithm consists of two main steps: a) linear structure detection, with a multi-scale analysis based on a second order image derivatives, and b) false positive reduction, based on the covariance matrix. We evaluated the algorithm performance on a testing set, composed of 33 patients coming from two different clinical centers. The system is showing promising results, evaluation and it could certainly be used to improve the specificity of the CAD system. Improving the accuracy of breast segmentation may also help reduce the number of FP findings. FP reduction is achieved by a set of simple heuristics criteria based on knowledge of the morphological and kinetics properties of FPs. A more efficient classifier could improve the system's FP rate.

On the other side, the classifier here proposed is able to discriminate malignant from benign breast mass-like lesions using two groups of features (morphological and kinetic), and obtaining a AUC of 0.94±0.03. The AUC for the feature selection (FS) resulting from the combination of all two feature groups was significantly higher than those obtained with all other selected FSs, showing that the combination of features increases the classification performances. A genetic algorithm was used to select feature subsets, in order to prevent unnecessary computation, overfitting, and to ensure a reliable classifier. The main limitation of the discrimination step is the limited number of lesions. This can produce overfitting of the training data, leading to overestimate the classifier's performance. In order to reduce these effects, the total number of features was limited to 19 and the selected feature subsets were composed only of 3 to 4 features. Moreover, classification performances were evaluated with a stratified 10-fold cross-validation method to reduce the classification bias. Another limitation is the unbalanced dataset. The number of malignant lesions is higher than benign lesions, leading to a possible bias in the discrimination of malignancy. This problem was partially reduced by presenting at training the same number of malignant and benign lesions using copies of benign lesions. Nevertheless, the benign class can be poorly described in the feature space.

In conclusion, the proposed CAD system was tested on MR datasets obtained from different scanners, with a variable temporal and spatial resolution and on both fat-sat and non fat-sat images, and has shown promising results. This type of system could potentially be used for early diagnosis and staging of breast cancer to reduce reading time and to improve detection, especially of the smaller satellite nodules. Further refinements are ongoing to improve vessel detection, breast segmentation, and to validated these conclusions on a larger dataset, including also non-mass like lesions.

Part II

Developing a computer aided diagnosis system for detection of prostate cancer using multispectral MRI

Prostate cancer (PCa) is the most common malignancy affecting men in the world, and represents the third cause of cancer death in industrialized countries [8, 9, 10]. Over the past two decades, prostate cancer diagnoses have become more common as a result of the aging population and the widespread use of screening tests. Whenever PCa is suspected, patients undergo biopsy guided by transrectal ultrasonography (TRUS). When cancer is confined to the gland patients are usually submitted to prostatectomy or undergo radiation therapy; a combination of radiation therapy, hormone therapy and chemotherapy is the preferred treatment in patients with advanced PCa. Five-year survival rate is high, being respectively 94.8% and 90% [85, 86].
There are several limitations to the currently applied diagnostic-therapeutic workflow, which can be summarized as follows:

1. Prostate-specific antigen (PSA) test has a low specificity in detecting PCa; common conditions, such as benign prostatic hyperplasia and prostatitis, also increase PSA levels. In [87] 19970 men that were screened with PSA, 2692 had PSA levels greater than 4.0 g/L, a widely used cutoff value for a positive screening result, but only 756 had prostate cancer (28%). Potential harms of PSA screening include: additional medical visits, adverse effects of prostate biopsies, anxiety, and over-diagnosis (e.g. the identification of prostate cancer that would never have caused symptoms in the patient's lifetime) leading to over-treatment with its associated adverse effects.

2. TRUS-guided biopsy has a low detection rate and low-specificity. Sextant biopsy has a high false-negative rate, approaching 30% when using extended biopsy schemes with retrieval of 10 to 12 cores [88]. Detection rate does not increase with repeated biopsies; on the opposite, sensitivity is reduced at the 2nd and higher rounds of biopsies [89].

3. Because of the lack of techniques for precise prostate cancer localization, current treatment strategies involve the whole gland. Due to the inherent risks associated with surgical resection and radiotherapy, many patients develop severe side effects (table 8.1) [90]. New and less invasive alternatives are now available for localized cancer, such as high intensity focused ultrasound (HIFU) or cryotherapy, but they require accurate imaging tools.

Magnetic Resonance Imaging (MRI) has shown promise in localizing PCa, because of its intrinsic high soft-tissue resolution. T2-w images allow clear visualization of the prostate

Table 8.1. *Adverse events of radical prostatectomy and radiotherapy.*

	Radical Prostatectomy	Radioteraphy
Bowel urgency	15%	32%
Urinary leakage	62%	34%
Erectile dysfunction	84%	77%

anatomy; the central lobe can be easily distinguished from the periphery of the gland, and the capsule is clearly discernible as a thin dark linear structure. Dynamic Contrast Enhanced MRI (DCE-MRI) captures T1-w images while a dose of contrast agent is injected and tumors can be detected since they usually show a distinctive early signal enhancement and washout of signal intensity in the delayed phases. Magnetic Resonance Spectroscopy (MRS) extends the possibilities of MRI to detect PCa by allowing assessment of molecular constituents of the tissue, especially of choline, which is in higher concentration in tissues with a high cellular metabolism [12]. Finally, Diffusion Weighted Imaging (DWI) can measure the diffusion of water molecules in tissue and hence provide information on the structural organization of the tissue. However, each MR approach alone has some drawbacks, which can be implied from the large range of sensitivity and specificity variations reported in the literature, only partially explained by the different diagnostic criteria used in the various study [12, 13]. Recently it has been shown that combining 2 or more MR modalities (such as for example T2-w and DCE-MRI) improves the sensitivity by almost 15%, bringing it up to 83-87% for tumors measuring 5 cm^3 or more[14]. However the more variables are introduced the more difficult it is even for the experienced reader to integrate all the available information into one reliable final report. Complex problems, such as the one reported in the previous paragraph, have been approached by developing computer aided diagnosis (CAD) systems that aid the radiologist in diagnosing disease. The aim of this part of the thesis was to develop a CAD system for detecting PCa, integrating all information available from the different MR sequences. By overcoming the limitations of the current subjective way of analyzing MR data, this approach could substantially modify the diagnostic and therapeutic work-up of individuals with PCa (Fig. 8.1). This could improve quality of patient's life dramatically.

Advantages are summarized as follows:

1. Individuals with high PSA values and a negative CAD-MR exam could avoid core-biopsies, thus reducing anxiety, the diagnostic delay of a false-negative finding, procedure related complications and the adverse events linked to overtreatment.

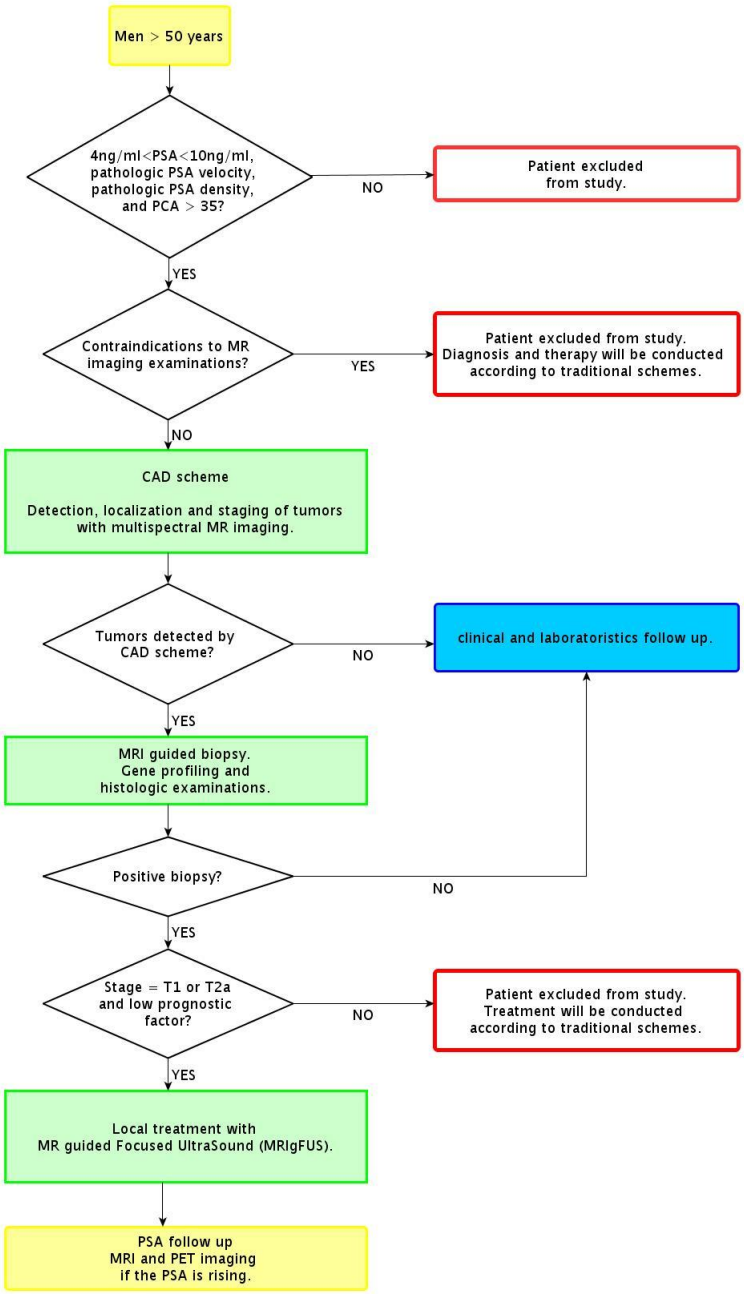

Figure 8.1. A new work-up for prostate cancer

2. In case of a positive finding, CAD-MR could be used to perform biopsy under MR guidance by using a specifically designed, commercially available medical device. This would increase the accuracy of the procedure. Furthermore, biopsy could allow

us not only to confirm the diagnosis of PCa but also possibly to identify tumor areas having a different grading.

3. Imaging guided procedures, such as cryotherapy or MR guided High Intensity Focused Ultrasound (MRgFUS) could be performed having accurate color parametric 3D maps of the tumor available to plan treatment. MR can monitor temperature or changes in diffusivity within the area of treatment if the procedure is performed directly in the MR unit, as is the case of MRgFUS.

Chapter 9

MRI sequences for multispectral MR imaging of the prostate gland

9.1 Defining a protocol for MRI acquisition

T2-w images are considered to be the *workhorse* images for PCa, and to optimize them, several T2-w images have been acquired on a dedicated phantom with different geometrical settings. Images have been then analyzed to identify those with the best trade off between spatial resolution and signal to noise ratio (SNR). Ideally, as T2-w images are also used as the morphological reference for the remaining MR sequences, all of the subsequent images should be acquired with the same geometrical setting as the T2-w acquisition. However, due to the scanner limitations, a compromise between spatial and temporal resolution has been necessary.

The DCE-MRI study must have a sufficiently high temporal resolution to obtain quantitative parameters from the dynamic curve fitting, and for this project 13 seconds have been proven to be sufficient in order to fit in the bi-compartmental model (or Toft model) without losing a large amount of anatomical information. Perfusion and permeability of the cancer vessels, in fact, can be investigated only provided that the sequence is fast enough to track such rapid physiological phenomena. Slow sequences are not indicated for this kind of studies, in fact a reduced temporal resolution results in significant errors in pharmacokinetic parameters, which may lead to an incorrect classification of the tumor kinetics.

Brownian motion of water in organs varies according to tissue characteristics and can be

estimated by means of DWI MR sequences. In this kind of acquisition the b-value is the crucial parameter; if it is not properly set the subsequent results may be erroneous. However, with this sequence it is necessary to reach a compromise between a b-value high enough to distinguish tumoral tissues, without dramatically decreasing the SNR, that is strictly correlated with the b-value. Considering that, two b-values –600 mm/s^2 and 1000 mm/s^2 – have been chosen.

9.2 MRI Protocols

The dataset is composed by 23 patients, 4 of them were part of the training set, the remaining 19 have been used to test and validate the algorithm. All studies have been acquired on a 1.5 Tesla (T) scanner (Signa Excite HDx, General Electric Healthcare, Milwakee, WI) using an endorectal radiofrequency coil.
DWI images have been acquired using a single-shot EPI sequence with the following technical parameters: FOV=16 cm, slice thickness 3 mm, pixel size=0.625 mm, BW=62.50 kHz, TR=7000ms, TE=92.8 ms, flip angle=90°, 256x256 matrix, b-value=600 s/mm^2, NEX=6, 24 slices. Apparent diffusion coefficient (ADC) values were calculated from two DWI images acquired with b-value=0 s/mm^2 and 600 s/mm^2.
T2-w images have been obtained using a fast recovery fast spin echo sequence with FOV=16 cm, slice thickness 3 mm, pixel size=0.3125 mm, BW=22.73 kHz, TR=3020 ms, TE=96.24 ms, flip angle=90°, 512x512 matrix, 24 slices.
For the DCE-MRI sequence the chosen protocol required a FAST spoiled gradient recalled echo sequence with the following parameters: FOV=16 cm, slice thickness 3 mm, pixel size=0.3906 mm, BW=83.33 kHz, TR=3.6 ms, TE=1.3 ms, flip angle=20°, 512x512 matrix, 24 slices. After the precontrast acquisition, patients were given 0,1 cc/kg gadobutrol (Gadovist) intravenously through a peripheral line at 2 ml/s, followed by an infusion of 20 cc normal saline at the same velocity. For each patient a total of 26 phases were acquired sequentially, each lasting 13 seconds.

Chapter 10

Registration

The first step for developing a CAD system, using multispectral MR images, is to perform an automatic image registration step to correct for misalignment between images coming from different MR sequences. Image registration is the process of finding a geometric transformation between the two respective image-based coordinate systems that maps a point in the first image set to the point in the second set that has the same patient-based coordinates. Registration should correct for voluntary and involuntary (breathing, hearth beating) movements during the dynamic acquisition (DCE-MRI), as well as for image distortion due to the magnetic susceptibility in the DWI images.

10.1 Registration between T2-w and DWI images

As previously said, DWI has extreme sensitivity to motion and, consequently, requires ultrafast imaging techniques, such as the single-shot echo planar imaging (EPI), in which an image is acquired within a single shot, thus during around 100 msec, and hence it is able to froze the motion during the acquisition. EPI, however, is affected by geometric distortions and chemical shift artifacts caused by the susceptibility effects. These effects are due to the air-filled balloon surrounding the endorectal coil and poor local B0 homogeneity which leads to pixel shifts, particularly in the phase encode direction. Jezzard [92] proposed a method to correct geometric distortion which requires the measure of the magnetic field map inside the FOV with the object to scan in place. Such a field map will include the effects of inhomogeneities of the main magnetic field and varying tissue susceptibility, then

values from the field map can then be compared with the expected values and the distortion calculated and corrected. This method achieved good performance but is difficult to implement in normal clinical practice. Other methods are semi automatic and require the manual placement of control points on both T2-w and DWI acquisition [91, 93]. In this section a new fully automatic method to register T2-w and EPI-DWI images which does not require the estimation of the static magnetic field and which is based on the automatic segmentation of the bladder and the endorectal coil will be presented. Bladder and endorectal coil are well-defined structures in both T2 and DWI and are easy to segment, while automatic prostate segmentation is challenging due to the heterogeneity of this anatomical region.

10.1.1 Methods

The entire registration procedure involves two major steps. First, an affine transform is estimated by a segmentation-based method. In this step the bladder is automatically segmented in the DWI image by a watershed algorithm applied on the apparent diffusion coefficient (ADC) map, where it is well visible because of its high water content. The watershed is computed over the gradient magnitude image and proceeds in several steps. First, an initial classification of all points into catchment basin regions is done by tracing each point down its path of steepest descent to a local minima. Next, neighboring regions and the boundaries between them are analyzed according to a saliency measure, which is, in this case, the minimum boundary height, to produce a tree of merges among adjacent regions. Then, excluding the background, the bladder is the biggest region obtained with an absolute minimum height percentage of 10% and a depth of the catchment basin of 30%. As the bladder segmentation on DWI is obtained, morphological erosion and dilation are applied to extract a stripe around the border of the bladder (Fig. 10.1c). The stripe thickness is 20 mm, so it always includes the bladder wall also on the T2-w image. Pixels belonging to this stripe on the T2-w image were classified by a k-means cluster in two groups according to their intensity values, and the segmentation of the bladder wall is obtained, as is shown in Fig. 10.1e.

Then bladder border points on the T2-w and DWI are extracted from the binary masks (Fig. 10.2) and coupled using the iterative closed points (ICP) algorithm (Fig. 10.3) in the slice where the bladder reaches its biggest area. The coupled points are used to find, by a least squares fitting, the affine transform parameters and then the transformation is

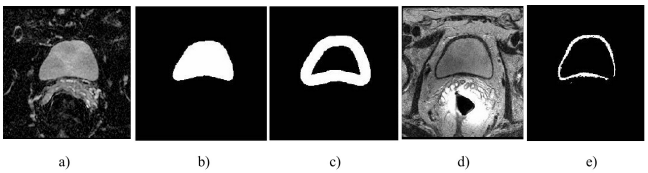

Figure 10.1. *a) Bladder on DWI image. b) Segmented bladder on DWI. c) Stripe around bladder wall on DWI d) Bladder on T2-w image. e) Segmented bladder wall on T2-w image.*

applied on the whole DWI image.

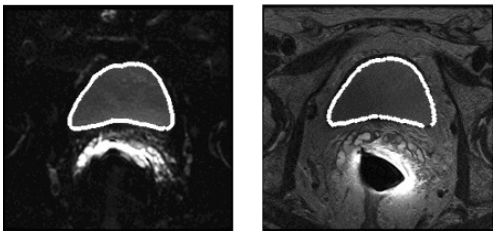

Figure 10.2. *Segmented bladder on the DWI image (a) and T2 image (b).*

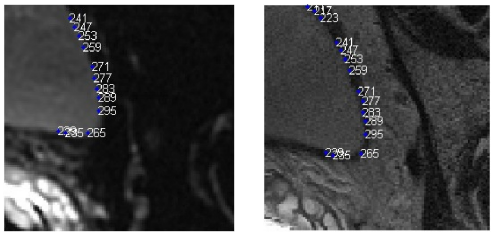

Figure 10.3. *Some of the bladder border points matched with ICP on DWI (a) and T2-w (b) images.*

The affine transform computed in the previous step can correct possible shearing, translational and scaling artifacts mainly caused by motion or by eddy currents (residual gradient field) formed in presence of a changing magnetic field [94], but do not correct non-linear geometric distortion caused in large part by static magnetic field inhomogeneities near the coil, and which is a major concern because most prostate tumors are localized in the peripheral zone. Therefore the first rigid registration step is refined with a non-rigid registration step based on the coil segmentation. The coil is segmented both in T2-w and DWI images by a region growing algorithm, starting from a seed point inside the coil which is

automatically found by a circular Hough transform. Then, for each slice where the coil is visible, two spline smoothing curves are fitted on the coil border points on the DWI and T2-w images and used to estimate the displacement near the coil surface (Fig. 10.4). The initial displacement is estimated as the difference between the upper points of these spline curves, as shown in Fig. 10.4. Therefore the deformation field T is modeled as a piecewise linear decay field along the vertical direction (Eq. 10.1), assuming that the pixel shifts caused by magnetic field inhomogeneities occur particularly in the phase encode direction [92] and decrease linearly with distance from the coil.

$$T(x) = 0$$
$$T(y) = \begin{cases} d_i - k * y & 0 < y < \frac{d_i}{k} \\ 0 & y > \frac{d_i}{k} \end{cases} \tag{10.1}$$

where the coordinate system is shown in Fig. 10.4. The decreasing rate of the vertical displacement k in (10.1) was chosen maximizing the overlap index described in the following section on a training set. Then the estimated deformation field T is applied to the DWI in order to correct the geometric distortion (Fig. 10.5).

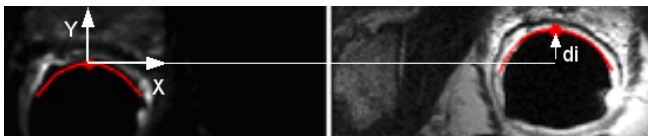

Figure 10.4. *Spline curves superimposed on DWI (left) and T2-w (right), and initial displacement between DWI and T2-w near the coil.*

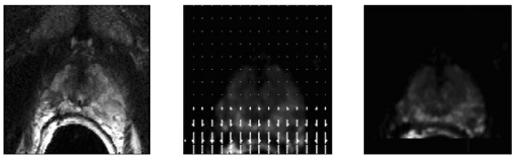

(a) (b) (c)

Figure 10.5. *a) Prostate on T2 image. b) Deformation field superimposed on DWI. c) Deformation field applied on DWI.*

10.1.2 Validation

In order to validate the registration method, the peripheral zone (PZ), the central gland (CG) and the whole prostate gland (TOT) were manually drawn by a radiologist on both DWI and T2-w images. In Fig. 10.6 are shown, both superimposed on the T2-w image, the outlines of PZ and CG binary masks drawn on DWI (red line) and the outlines of the same regions drawn on the T2-w (green) before (Fig. 10.6(a)) and after (Fig. 10.6(b)) the application of the registration method. Two performance indexes were calculated before and after registration: the overlap index (OI), defined as the ratio between intersection and union of the masks, and the mean surface distance (MSD).The training set was used to find the optimal decreasing displacement rate (k in (10.1)) maximizing the overlap index, then the algorithm was validated on the testing set described in section 9.2 . A t-test is performed to evaluate the p values between OI and MSD values before and after registration. The null hypothesis is that there is no difference between OI and MSD values before and after registration, with a significance level of 0.05.

10.1.3 Results

Table 10.1 reports the MSD values and Table 10.2 the OI values for CG, PZ and TOT before and after registration. P-values for MSD measurements for CG, PZ and TOT are respectively 0.001, 0.0000005 and 0.000004, while p-values of OI measurements are 0.0002, 0.00000 and 0.00000006 respectively. All p-values are smaller than the significance level, showing that the OI and the MSD obtained before registration are statistically different from those obtained after registration.

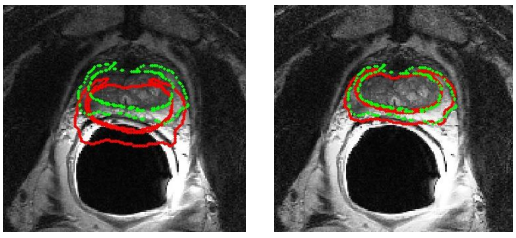

(a) (b)

Figure 10.6. *Manual prostate gland segmentation drawn on DWI(red) and T2 (green) superimposed on T2, before registration (a) and after registration(b)*

Table 10.1. *Mean Surface Distance (MSD) for CG, PZ, TOT zones pre- and post-registration. Δ represents the % difference between the MSD pre and post registration.*

Patients	CG pre (mm)	PZ pre (mm)	TOT pre (mm)	CG post (mm)	PZ post (mm)	TOT post (mm)	Δ CG	Δ PZ	Δ TOT
# 1	0.30	1.66	0.32	0.11	0.27	0.08	-63%	-84%	-75%
# 2	0.38	2.05	0.57	0.08	0.39	0.13	-79%	-81%	-77%
# 3	0.42	1.40	0.56	0.16	0.29	0.13	-62%	-79%	-77%
# 4	0.39	1.82	0.59	0.24	0.31	0.20	-38%	-83%	-66%
# 5	1.36	0.16	1.33	0.25	0.12	0.12	-82%	-25%	-91%
# 6	0.25	1.54	0.29	0.11	0.46	0.09	-56%	-70%	-69%
# 7	0.29	1.75	0.50	0.11	0.22	0.10	-62%	-87%	-80%
# 8	0.19	1.30	0.44	0.17	0.22	0.09	-11%	-83%	-80%
# 9	0.30	2.07	0.50	0.14	0.27	0.13	-53%	-87%	-74%
# 10	0.29	0.79	0.27	0.20	0.24	0.13	-31%	-70%	-52%
# 11	1.64	3.33	1.35	0.29	0.50	0.16	-82%	-85%	-88%
# 12	0.43	2.17	0.51	0.13	0.55	0.14	-70%	-77%	-73%
# 13	0.98	2.41	0.93	0.53	1.13	0.42	-46%	-53%	-55%
# 14	0.25	1.27	0.51	0.21	0.42	0.19	-16%	-67%	-63%
# 15	0.25	1.39	0.56	0.25	0.50	0.24	-0%	-64%	-57%
# 16	0.26	1.10	0.38	0.13	0.32	0.13	-50%	-71%	-66%
# 17	0.90	4.31	1.42	0.12	0.72	0.26	-87%	-83%	-82%
# 18	0.25	0.89	0.35	0.23	0.41	0.21	-8%	-54%	-40%
# 19	0.38	2.80	0.98	0.19	0.84	0.26	-50%	-70%	-73%
Mean	0.50	1.80	0.65	0.19	0.43	0.17	-50%	-72%	-70%
STD	0.42	0.95	0.37	0.10	0.25	0.08	26%	15%	13%

10.2 Registration between T2-weighted and dynamic contrast enhanced T1-weighted MRI

DCE-MRI, as it has been said in Section 3.5, is a widely used technique for quantitative assessment of the vascular properties of tissue. Observing the rate of change of image intensity in the presence of a gadolinium-based contrast agent allows inferences to be made about the underlying vascular status. The pattern of enhancement yields quantitative information that allows the assessment of pharmacokinetics in both single studies and in sequential studies such as screening [95]. In this situation, motion artifacts can have a strong influence on parameter estimation by causing apparently extreme changes in enhancement. An explicit example is a non-enhancing location that at some time-point is subject to motion that replaces the underlying tissue with that of tissue that has enhanced. Therefore, the model-fit used during DCE-MRI analysis, may distort the enhancement curve to accommodate this change. If the motion is early, the pixel will have a strong wash-in and wash-out, potentially aliasing to pathological enhancement. Similarly for

Table 10.2. *OI for CG, PZ, TOT zones pre- and post- registration. Δ represents the % difference between the OI pre and post registration.*

Patients	CG pre	PZ pre	TOT pre	CG post	PZ post	TOT post	Δ CG	Δ PZ	Δ TOT
# 1	0.77	0.33	0.80	0.85	0.65	0.88	10%	97%	10%
# 2	0.73	0.30	0.72	0.87	0.62	0.85	19%	107%	18%
# 3	0.64	0.37	0.69	0.77	0.68	0.83	20%	84%	20%
# 4	0.73	0.35	0.71	0.77	0.72	0.83	5%	106%	17%
# 5	0.50	0.24	0.60	0.78	0.69	0.84	56%	187%	40%
# 6	0.76	0.31	0.79	0.84	0.53	0.87	10%	71%	10%
# 7	0.76	0.36	0.74	0.83	0.71	0.86	9%	97%	16%
# 8	0.80	0.44	0.77	0.80	0.72	0.88	0%	64%	14%
# 9	0.77	0.30	0.75	0.84	0.67	0.85	9%	123%	13%
# 10	0.76	0.55	0.78	0.79	0.71	0.84	4%	29%	8%
# 11	0.42	0.18	0.51	0.70	0.54	0.81	67%	200%	59%
# 12	0.73	0.29	0.73	0.82	0.53	0.84	12%	83%	15%
# 13	0.53	0.30	0.60	0.64	0.49	0.71	21%	63%	18%
# 14	0.77	0.49	0.74	0.75	0.67	0.83	-3%	37%	12%
# 15	0.77	0.46	0.73	0.73	0.64	0.81	-5%	39%	11%
# 16	0.78	0.49	0.77	0.82	0.65	0.84	5%	33%	9%
# 17	0.57	0.12	0.54	0.82	0.46	0.76	44%	283%	41%
# 18	0.74	0.51	0.76	0.76	0.68	0.81	3%	33%	7%
# 19	0.69	0.27	0.64	0.78	0.49	0.79	13%	81%	23%
Mean	0.70	0.35	0.70	0.79	0.62	0.83	16%	96%	19%
STD	0.11	0.11	0.08	0.06	0.09	0.04	19%	66%	13%

later motion artifacts, the enhancement curve may be distorted such that the pixel is observed to enhance in a normal mode, particularly if the bolus arrival time is fixed. Thus, parameter estimation depends strongly on the flexibility of the fitted model and its ability to identify outliers resulting from either poor model choice or patient motion or both [96]. For these reasons the registration within the DCE sequence is a key point to develop a system able to analyze parameters derived from the images during the contrast injection. However, the aim of this part of the thesis was to develop a multispectral CAD system, that should take informations coming from different dataset. Therefore, the main idea was to register the whole dynamic sequence to the T2-w image. The advantages deriving from using T2-w images as an additional MR modality to discriminate PCa from benign regions in the peripheral zone (PZ) of the prostate has been widely studied [96], as they are also used by the radiologist for localizing PCa. Notwithstanding, the challenge of using T2-w images as reference in the registration step of a CAD system arises from adding a new source of possible misalignment, and introduce differences between the two datasets that should be taken into account (Fig. 10.7).

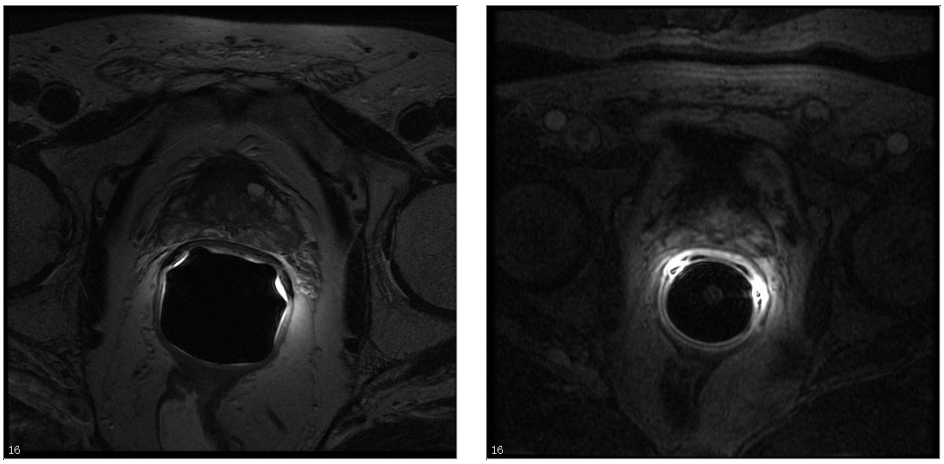

(a) (b)

Figure 10.7. *On the left: a slice from a T2-w volume. On the right: a slide from a DCE-MRI acquisition. It is important to notice how the two images are different in terms of spatial resolutions, signal intensity, field of view, and origin of the images.*

10.2.1 Methods

Image preprocessing

To overcome the problem of having two dataset with different field of view (FOV), origin, spatial resolution and signal intensities, some preprocessing algorithms have been developed as first step of this registration method.
As previously said (Section 9.1) T2-w images have a higher spatial resolution than the DCE-MRI sequences, thus having a smaller field of view (FOV). The slice thickness is 3 mm for both dataset, while the pixel size is 0.3125 mm for T2-w images and 0.3906 mm for the dynamic sequence. In order to register two dataset having the same FOV, the T2-w images have been downsampled to the DCE spatial resolution. The downsampling operation have been preferred to the upsampling of the dynamic sequence to avoid the introduction of interpolated pixels in a volume where a pixel wise analysis will be performed to detect and diagnose tumoral tissues. Hereinafter, each volume of the DCE sequence need to be cropped in order to obtain the same FOV of the T2-w images. Even if in this project the entire dataset belongs to one center, thus having the same scanner and using the same acquisition parameters, the whole procedure is fully automatic, and takes the spatial information from the dicom header, making the algorithm potentially able to work with dataset coming from different scanners or acquired with different parameters.

Secondly, in order to perform a registration between dataset having different image intensities, it is necessary to find a set of similar features in the first image to a set of features in the second image that are also mutually similar [97]. For example, according to the principle of mutual information (see Sec. 10.2.1), homogeneous regions of the first image set should generally map into homogeneous regions in the second set [98, 99]. However due to the coil susceptibility and other sources of noise, the histogram of both T2-w and DCE images have a tail of noisy pixels, that make the similarity measure less reliable. In order to make the shape of the histogram more congruent, a threshold based on the position of the 99% percentile of the images has been set (Fig. 10.8). In Fig. 10.9 results of the preprocessing step applied on the T2-w and on three enhanced images of the dynamic sequence are shown.

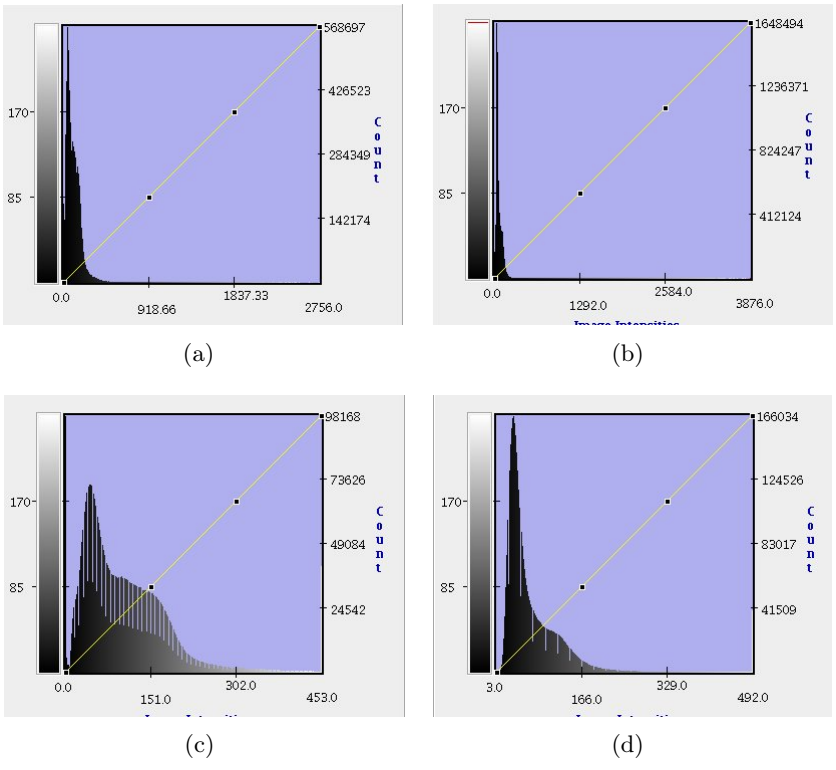

Figure 10.8. *Histograms of the t2-w and DCE images. a) Original T2-w histogram; b) Original DCE histogram; c) Thresholded T2-w histogram; d) Thresholded DCE histogram.*

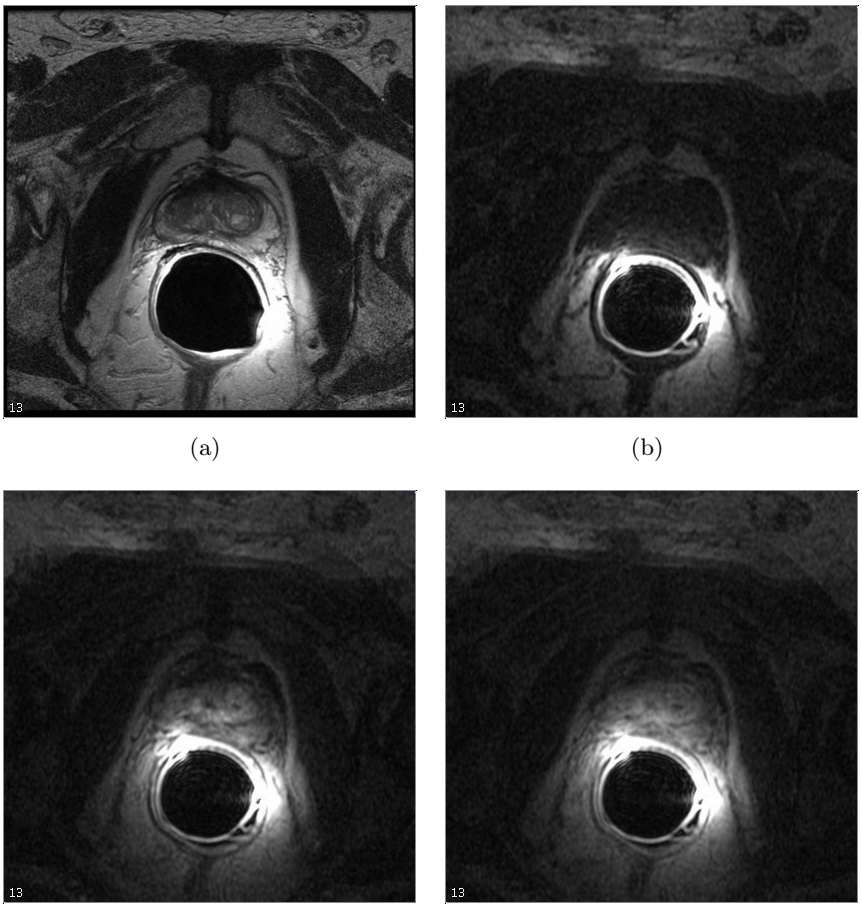

(a) (b)

(c) (d)

Figure 10.9. *Preprocessing step applied on the T2-w image (a),and on the first (b), seventh (c) and fourteenth (d) enhanced images.*

Affine transform

There are many different transforms algorithm studied and used for image registration, from simple translation, rotation and scaling to general affine and kernel transform. For prostate T1-w to T2-w image registration we found that the most suitable transform is the affine, because it is able to consider also the shearing derived from the transrectal coil. Affine transform is composed of rotation, scaling, shearing and translation. The transform is specified by a N×N matrix and a N×N vector where N is the space dimension. Its main advantage comes from the fact that it is represented as a linear transformation, and the coefficients of the N×N matrix can represent rotations, anisotropic scaling and shearing. Equation 10.2 illustrates the effect of applying the affine transform in a point in 3D space.

$$\begin{bmatrix} x\prime \\ y\prime \\ z\prime \end{bmatrix} = \begin{bmatrix} M_{00} & M_{01} & M_{02} \\ M_{10} & M_{11} & M_{12} \\ M_{20} & M_{21} & M_{22} \end{bmatrix} \cdot \begin{bmatrix} x - C_x \\ y - C_y \\ z - C_z \end{bmatrix} + \begin{bmatrix} T_x + C_x \\ T_y + C_y \\ T_z + C_z \end{bmatrix} \tag{10.2}$$

Registration metric

The metric component of a registration algorithm provides a measure of how well the fixed image (in our algorithm the T2-w) is matched by the transformed moving (each DCE volume) image, forming the quantitative criterion to be optimized during the iterative process. As we previously said, if different modalities are involved, metrics based on direct correlation of gray levels are not applicable, and a statistical measure need to be involved. The chosen metric is the one based on the mutual information (MI) similarity, in particular the one developed by Mattes [56]. The major advantage of using MI is that the actual form of the dependency does not have to be specified. Therefore, complex mapping between two images can be modeled. This flexibility makes MI well suited as a criterion of multi-modality registration. Mutual information is defined in terms of entropy. Let

$$H(A) = \int p_A(a) \log p_A(a) da \tag{10.3}$$

be the entropy of a random variable A, H(B) the entropy of a random variable B, and

$$H(A, B) = \int p_{AB}(a, b) \log p_{AB}(a, b) da db \tag{10.4}$$

be the joint entropy of A and B. If A and B are independent, then

$$p_{AB}(a, b) = p_A(a) p_B(b) \tag{10.5}$$

and

$$H(A, B) = H(A) + H(B). \tag{10.6}$$

However, if there is any dependency, then

$$H(A, B) < H(A) + H(B). \tag{10.7}$$

The difference is called Mutual Information: I(A,B)

$$I(A, B) = H(A) + H(B) - H(A, B) \tag{10.8}$$

In Mattes MI implementation, only one set of intensity samples is drawn from the image. Using this set, the marginal and joint probability density function (PDF) is evaluated

at discrete positions or bins uniformly spread within the dynamic range of the images. Entropy values are then computed by summing over the bins. Therefore the metric requires two parameters to be fine tuned: the number of bins used to compute the entropy and the number of spatial samples used to compute the density estimates. The number of spatial samples can usually be as low as 1% of the total number of pixels in the fixed image. Increasing the number of samples improves the smoothness of the metric from one iteration to another and therefore helps when this metric is used in conjunction with optimizers that rely of the continuity of the metric values. The trade-off, of course, is that a larger number of samples result in longer computation times per every evaluation of the metric. It has been demonstrated empirically that the number of samples is not a critical parameter for the registration process. In the algorithm development the best compromise on the time it takes to compute one evaluation of the Metric have been obtained using the 5% of the total number of samples. On the contrary, the number of bins may have dramatic effects on the optimizer's behavior, the chosen value for this algorithm was 50 bins.

Since the fixed image PDF does not contribute to the metric derivatives, it does not need to be smooth. Hence, a zero order (boxcar) B-spline kernel is used for computing the PDF. On the other hand, to ensure smoothness, a third order B-spline kernel is used to compute the moving image intensity PDF. The advantage of using a B-spline kernel over a Gaussian kernel is that the B-spline kernel has a finite support region. This is computationally attractive, as each intensity sample only affects a small number of bins and hence does not require a N×N loop to compute the metric value. During the PDF calculations, the image intensity values are linearly scaled to have a minimum of zero and maximum of one. This rescaling means that a fixed B-spline kernel bandwidth of one can be used to handle image data with arbitrary magnitude and dynamic range.

Multiresolution optimization strategy

The registration process is automated by varying the deformation in the test image (DCE) until the discrepancy between the two images is minimized. We use a regular step gradient descent optimizer, to reduce the cost function in until termination criteria are satisfied. The gradient descent optimizer method is the most straightforward method for incorporating gradient information in the minimization process [100]. The minimum of the function is found by a number of consecutive 1-D line minimization steps, and each of this step starts

at the minimum found in the previous step and proceeding in the direction of the gradient at that point, i.e. the direction of the steepest descent.
In order to avoid local minima, and to decrease computation time, we use a hierarchical multiresolution optimization scheme. We initially optimize for a deformation to recover the gross motion of the patient and large anatomic structures. As we increase the resolution, we recover increasingly fine misalignments. The spatial mapping determined at the coarse level is then used to initialize registration at the next finer scale. This coarse-to-fine strategy greatly improve the registration success rate and also increases robustness by eliminating local optima at coarser scales. The registration pipeline for the multiresolution approach is described in Fig. 10.10(a) where the image pyramids represent the set of downsampled and smoothed fixed and moving images. Each level of the image is used for a single level of the registration method (see Fig. 10.10(b)); in the method here presented the number of resolution steps was set as 4.

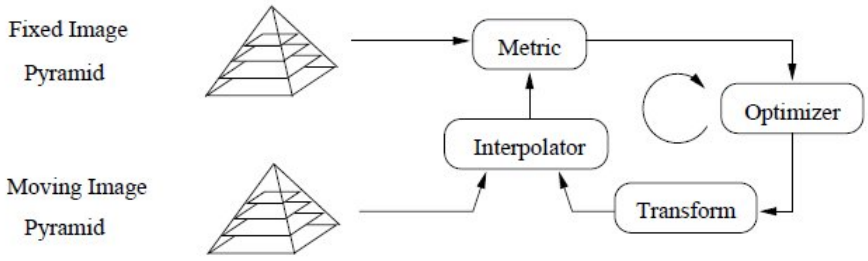

(a)

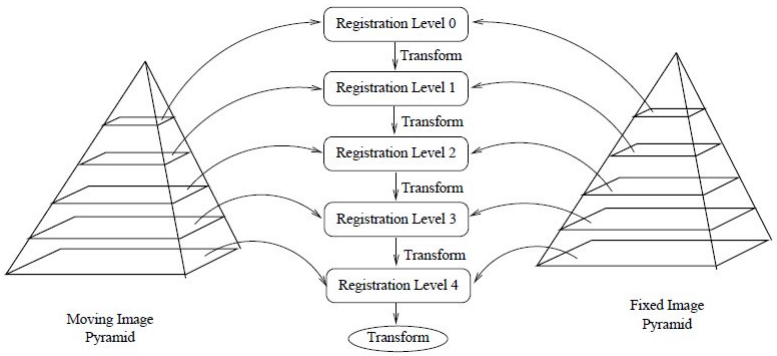

(b)

Figure 10.10. *Components of the multi-resolution registration framework*

10.2.2 Results

Validating the performance of an image registration algorithm with real images is not straightforward. The lack of a gold standard complicates matters and prevents any automated assessment of registration accuracy. Even if individuals trained to interpret medical images are involved in a validation experiment, providing a method for consistently assessing individual images is difficult. There is a tradeoff between the number of images that can be assessed and the time required to assess each one, a situation that often forces researchers to validate algorithms based on a limited sample size. However the capacity of the human eye to rapidly and accurately (albeit only qualitatively) determine the quality of a registration should not be underestimated. While validation methods involving human assessment will be prone to error, bias, and inconsistencies, if two images are presented in a user-friendly manner, experienced physicians can rapidly assess the "gestalt"quality of the registration in a short amount of time. Furthermore, they have a priori knowledge of where in the anatomy the quality of the registration should be high and where these requirements can be relaxed. An experienced radiologist blindly analyzed the registered and non-registered images, having the possibility to draw region of interest on the images. After the analysis of 10 patients the radiologist affirmed that the quality of the registered images was superior than the quality of the non-registered ones. A more accurate validation will be done, analyzing the performances of the lesion classifier working with both registered and non-registered images. The registration algorithm would be considered useful if we will obtained a more robust classification using the registered images. In Fig. 10.2.2, 10.2.2 are shown some registration results.

10.3 Discussions

In this Chapter we presented two automatic registration algorithms able to correct misalignment between T2-w, DWI and DCE images, due to a) incorrect determination of the resonance frequency by the scanner in some measurements leading to a "rigid body" shift in the phase-encoding direction of the echo planar images, b) susceptibility inhomogeneities resulting in irregular distortions, e.g. proximal to rectal wall at the air-tissue interface, and c) voluntary and involuntary patients movements during the acquisition.
To the best of our knowledge there are no methods in literature addressing the registration between T2-w and DWI in an fully automatic way. De Souza et al. [91] corrected the

displacement between by shifting the DWI images according to the amount of displaced center of mass, manually calculated. Automatic methods have the potential of reducing inter- and intra-observer variability and reading time, and could be integrated in a fully automatic CAD system for prostate cancer detection and diagnosis. One limitation of this method is represented by the choice of the parameters for the piecewise linear decay modeling. These parameters are heuristic constants chosen in order to obtain the best performance on the training set. Future works should include the choice of such parameters based on a optimization step, i.e. including mutual information, in order to obtain more reproducible results and better generalize the problem.
In conclusion, we presented a method to automatically register images coming from three different datasets, and results showed a good overlap after registration and a strong decrease of mean surface distance in both the central gland and peripheral zone. The algorithm should be certainly tested on a larger dataset, but its promising results suggest that it could be integrated in a CAD system which will combine the pharmacokinetic parameters derived from DCE-MRI, T2-w MRI and DWI MR.

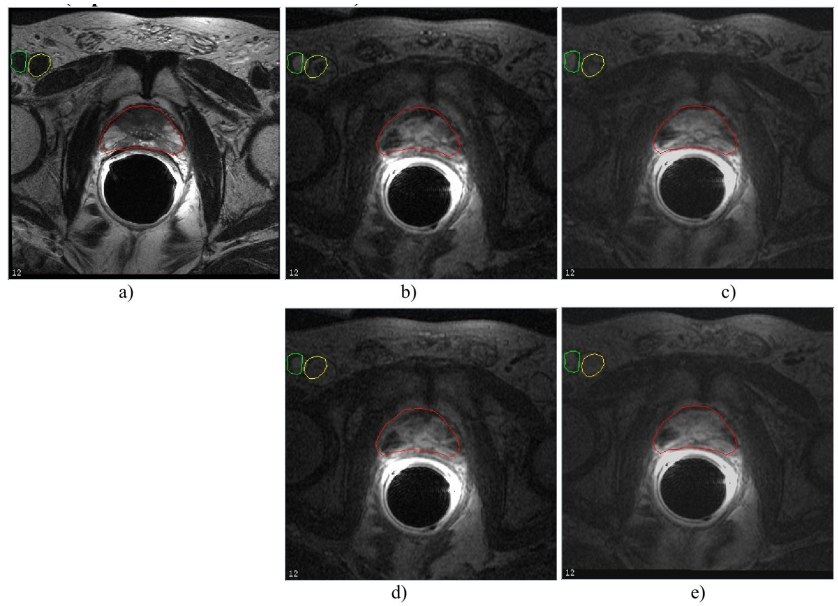

(a)

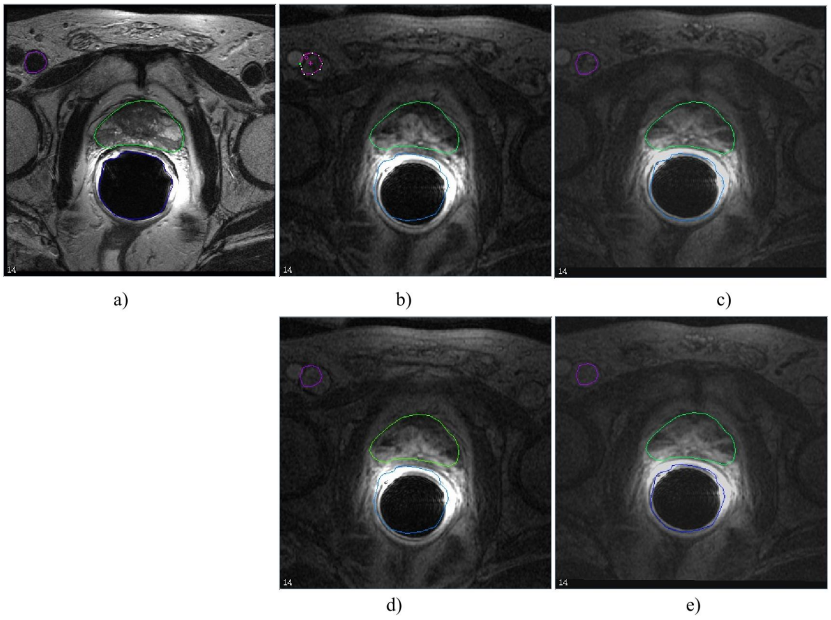

(b)

Figure 10.11. *Result of the registration between T2-w and DCE images. Above: a) T2-w, b) non-registered frame 7 post-contrast, c) registered frame 7 post-contrast, b) non-registered frame 14 post-contrast, c) registered frame 14 post-contrast. Below is represented the same frame of the same patients, but in a different slice of the volume. The colored ROIs represent the region of interest drawn by the radiologist on the T2-w image and superimposed on the non-registered and registered images. It is noticeable the better overlap between the ROIs and the anatomic region on the registered images.*

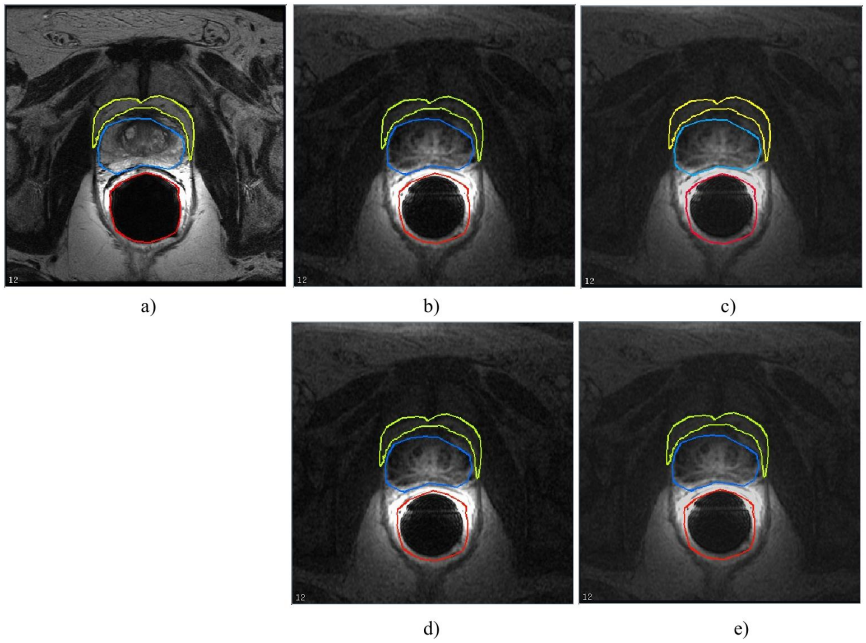

Figure 10.12. *Result of the registration between T2-w and DCE images applied on another patient. a) T2-w, b) non-registered frame 7 post-contrast, c) registered frame 7 post-contrast, b) non-registered frame 14 post-contrast, c) registered frame 14 post-contrast. In this case patient's movements are smaller and less evident, but it is still significant a better overlap in the registered images.*

Chapter 11

Lesions characterization

Having all the datasets registered, suspicious areas could be segmented, by representing each pixel like a vector containing scalar values, such as T2-w image intensity, quantitative physiological parameters (i.e. K_{ep}, K_{trans}) obtained from DCE-MRI datasets, and values of apparent diffusion coefficient (ADC) maps obtained from DWI images.
The aim of this chapter is to present a fully automatic scheme for the discrimination of malignant prostate lesion from healthy tissue, based on quantitative extraction of features coming from DCE-MRI images. DCE-MRI may offer quantitative information about perfusion, vessel permeability, blood volume and interstitial volume. The main drawback of this approach is that accurate pharmacokinetic modeling of DCE-MRI data requires knowledge of the concentration of the contrast agent in plasma, which is generally difficult to measure, largely because of limited temporal resolution, especially in a standard clinical setting. Low temporal resolution causes systematic errors in model output parameters, inter-patient variability and intra-patient variations between successive measurements. As an alternative to this approach empirical functions can be used, avoiding any assumption about tumor physiology.
The algorithm here presented will assess the probability of malignancy pixel-wise in a predefined area of the prostate gland.

11.1 Methods

All DCE-MRI studies, previously described (Sec 9.2) were examined by an expert radiologist who drew, by using a self-made algorithm, a series of regions of interest (ROI) around

the suspicious areas and on the opposite side of the gland on healthy tissue. Twenty areas of prostate carcinoma, all located in the peripheral zone (PZ) of the gland, were detected and contoured. The median tumor size was 61 mm^2; range from 18 to 119 mm^2. Benign regions were selected for each patient in healthy PZ whose dimension was comparable to that of the corresponding malignant tumor. Pixels belonging to the same selected ROI were then extracted from each of the 26 series of images in order to construct the time-intensity curves, hereinafter $C(t)$.

11.1.1 Time-intensity curves extraction and filtering

The signal intensities of pixels belonging to the same ROI were extracted from each of the 26 DCE volume acquisitions, to construct the time-intensity curves $C(t)$ as

$$C(t) = \frac{S(t) - S(0)}{S(0)} \tag{11.1}$$

where $S(t)$ is the image signal intensity in each volume and $S(0)$ is the precontrast signal intensity. Subsequently a wavelet filtering operation was performed to reduce the noise contribution. This step is composed by the following steps: a) 4^{th} level signal decomposition using a 4^{th} order Daubechies filter; b) threshold on the wavelet coefficients; c) inverse transform to reconstruct the signal. Figure 11.1 shows an application of such signal denoising procedure. The signal to noise ratio (SNR) was estimated as the ratio between the

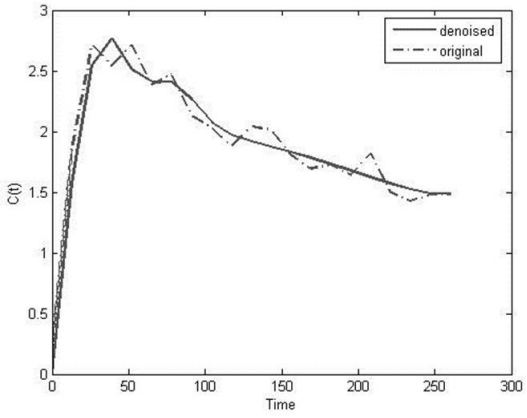

Figure 11.1. *Example of the wavelet denoising result on a time-intensity curve.*

power of the original signal to the power of the difference between the original and the

denoised signal. Pixels with SNR lower than 10 dB were excluded from the analysis.

11.1.2 Features extraction

Bicompartmental Toft model [101][6], Eq. 11.2, was used to perform fitting on the remaining curves to extract pharmacokinetic parameters (v_e, K_t, k_e).

$$C(t) - v_p C_p(t) + K^{trans} \int_0^t C_p(\tau) e^{-k_{ep}(t-\tau)} d\tau \tag{11.2}$$

where C_p is the CA concentration in the plasma, also called the artery input function (AIF), K_{trans} is the trans-endothelial transport of contrast medium from vascular compartment to the tumor interstitium, k_{ep} is the transport parameter of contrast medium back into the vascular space, v_e is the extravascular-extracellular space fraction of the tumor, and v_p is the plasma volume fraction ($v_e + v_p = 1$). The AIF was computed by placing a ROI on the iliac artery by an expert operator.
In addition to the pharmacokinetic model, the following two empirical functions were used to fit $C(t)$, without making any assumption about tumor physiology: the Weibull function, Eq.11.3, and the Phenomenological Universalities (PUN) approach [102] in Eq. 11.4.

$$y_{weib}(t) = At \cdot exp(-t^B) \tag{11.3}$$

$$y_{PUN}(t) = exp\left[rt + \frac{1}{\beta}(a_0 - r)(exp(-\beta t) - 1\right]. \tag{11.4}$$

The nonlinear curve fitting was solved in the least-squares sense with the Levenberg-Marquardt algorithm, starting from an initial guess estimated with a grid parameters search. Fitting goodness was evaluated using the determination coefficient (R^2). Upper and lower bounds of the model parameters were chosen to reflect physiological behavior normally found in healthy and tumor tissues. Furthermore, some model-free features were also derived from $C(t)$: maximum uptake (MU), peak location (PL), defined as the frame index at which the maximum enhancement occurs, uptake rate (UR) defined as MU/PL, initial area under the curve C(t) (IAUC), calculated within the first 60 seconds after the contrast injection, and washout rate (WR) defined as $\frac{MU - C(t_{END})}{t_{END} - PL}$, where t_{END} is the final time point in the acquisition series. A total of 13 parameters were extracted for each pixel in each ROI. The scatter plots of the most significant combination of features for Toft,

Weibull, and PUN models are reported in Figure 11.2. A good separation between the features describing the malignant curves and the benign ones can be observed in each of the three parameter planes.

11.1.3 Features selection

The initial 13 features set was reduced in order to avoid over-fitting problems and to discard redundant information. Therefore the best features were selected according to their area under the Receiving Operator Characteristic (ROC) curve (Table 11.1). In couples of highly correlated features the parameters with the smaller area under the ROC curve was discarded 11.2.

Table 11.1. *Area under ROC curves for each single parameters*

Toft			**Non parametric features**					**Weibull**		**PUN**		
v_e	K_T	k_e	MU	PL	UR	WR	IAUC	A_{weib}	B_{weib}	r	β	a_0
0.6	0.86	0.86	0.72	0.88	0.85	0.81	0.53	0.89	0.90	0.83	0.79	0.85

Table 11.2. *Area under ROC curves for each single parameters*

(k_e, K^{trans})	(MU, UR)	(UR, A)	(MU, A)
0.81	0.83	0.93	0.87

11.1.4 Bayesian classifier

A 6-dimensional vector $X = [K_T, \mathrm{PL}, \mathrm{WR}, A_{weib}, B_{weib}, a_0]$ was generated for all of the 10964 pixels (5168 benign and 5796 malignant) whose model fitting did not fail ($R^2 \geq 0.7$). Since the available dataset was not large enough to build two separated subsets, one for the training and the other for the testing procedure, the performance of the algorithm was estimated by exploiting the leave-one-out (LOO) method. The LOO involves training on all but one patient, and testing on the left-out patient by estimating the likelihood of pixels malignancy. The procedure was repeated until each case has been tested individually. In each LOO step the training pixels were used to estimate the class-conditional probabilities P(X|mal) and P(X|ben), assuming that the features come from a multivariate normal distribution. The malignancy probabilities for the testing pixels were calculated with the Bayes rule as stated in Eq.11.5

$$P(mal)|X_i) = \frac{X_i|P(mal)P(mal)}{P(X_i)} \tag{11.5}$$

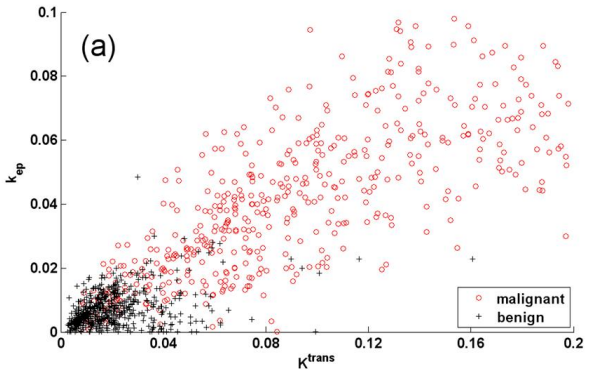

(a)

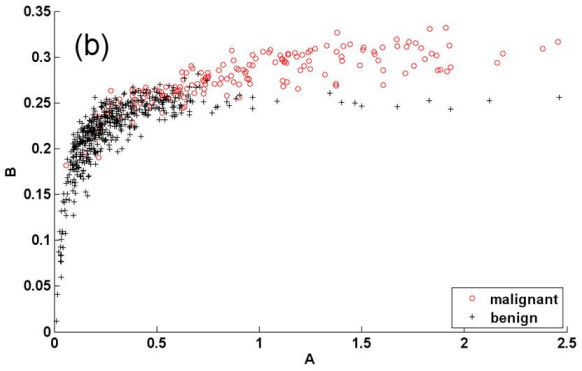

(b)

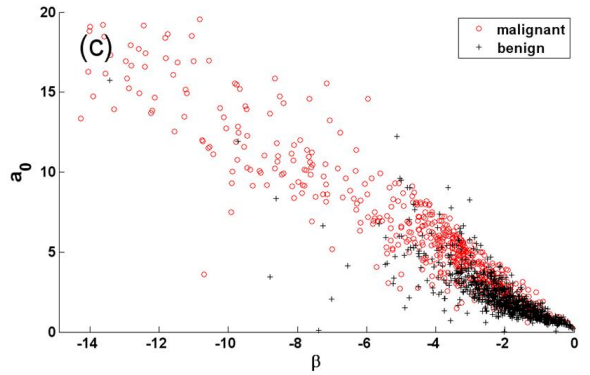

(c)

Figure 11.2. *Scatter plots of three quantitative models implemented: (a) Toft (K_{trans}, k_{ep}), (b) Weibull (A, B), and (c) EU1 model (β, a_0). Good separation between malignant and benign points can be observed for the three combination of parameters shown.*

where X_i is i-th feature vector associated to the i-th pixel, $P(mal)$=0.5 is the a priori probability of malignancy assumed equal to the a priori probability of benignity, and

$P(X_i) = P(mal)P(X_i|mal) + P(ben)P(X_i|ben)$.

11.2 Results

Figure 11.3 shows the output ROC curve for the Bayesian classifier. The resulting area

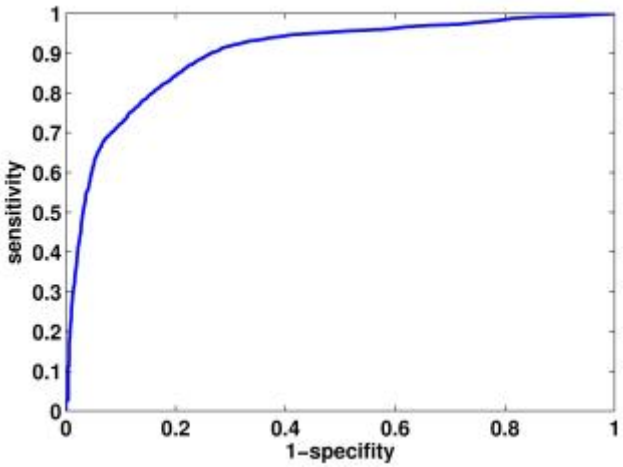

Figure 11.3. *ROC curve for the Bayesian classifier computed on a total of 10964 pixels (5168 benign and 5796 malignant)*

under the curve was 0.899 (95%CI:0.893-0.905); sensitivity and specificity were 82.4% and 82.1% respectively at the best cut-off point (0.352). Using only the three Toft parameters (v_e, K_T, k_e)the ROC area was equal to 0.879 (CI 95%:0.873-0.886). The difference between the area under the ROC computed using the 6-dimensional vector and the Toft model alone parameters is significant ($p < 0.001$)[103].Among the features here proposed, the Weibull-ones show the better discriminating performance with respect to all the others (ROC area = 0.896, 95%CI:0.889-0.902).
Figure 11.4 shows an example of the output probability map of a suspected lesion and a healthy region.

11.3 Discussion

The Bayesian classifier here shown achieved good performances in discriminating between benign and malignant regions in the prostate PZ. This system obtained a bigger area under the ROC curve compared to the results of previous works available in literature based on Toft model, leading to a better lesion detection rate. However, the classifier

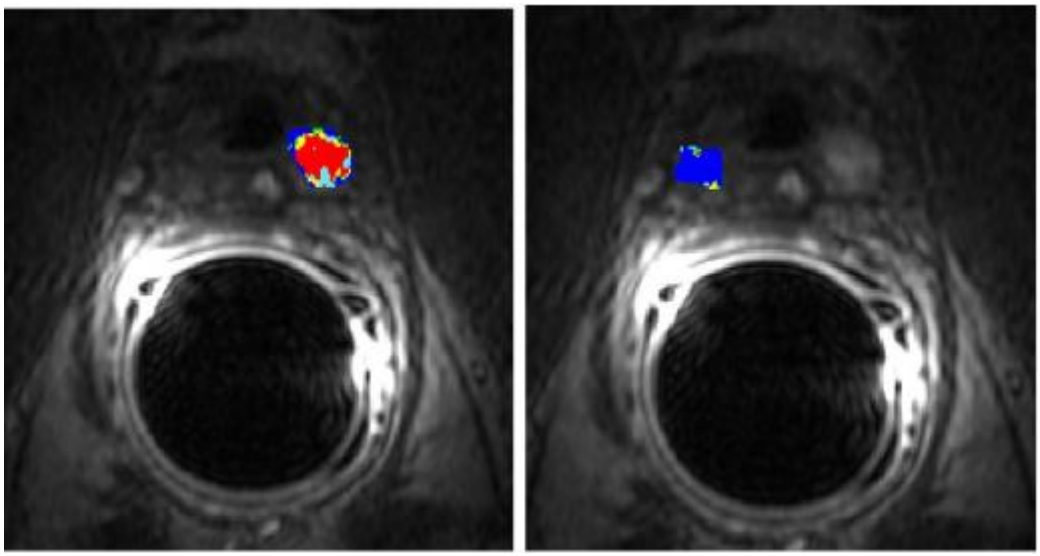

Figure 11.4. *Output probability map computed on a suspected lesion as well as on a healthy zone. Red color means a probability $p \geqslant 0.8$, yellow: $0.6 \leqslant p < 0.8$, green: $0.4 \leqslant p < 0.6$ and blue:$p < 0.4$.*

performs a pixel-wise analysis without taking into account neighbor pixels, hence a possible improvement will be the integration of information coming from a kernel analysis.
Moreover this system should integrate parameters obtained on T2-w and DWI image, in order to perform a multispectral analysis, and should be test in a larger dataset, using histological tumor maps as ground truth, but the promising results here obtained suggest high likelihood to be successful.

Chapter 12

Monitoring local treatment using Diffusion Weighted MR Imaging

In the proposed diagnostic-therapeutic path, once the lesion detection and characterization have been obtained, a MRI guided biopsy could be performed, directing the biopsy needles on the suspected region, thus avoiding random biopsies. In case of positive biopsy and localized tumors (stage T1—localized to one part of the body, and stage T2 —locally advanced) a local treatment will be performed. Four modalities appear to have the most clinical promise for prostate cancer focal therapy, including HIFU, cryotherapy, Radiation Therapy (RT) and Photodynamic Therapy (PDT) (see Table 12.1).

12.1 Criotherapy

Interest in cryotherapy has been renewed as understanding of cryobiology has evolved and newer cryoprobes have become available. Third-generation cryoprobes currently use gas rather than liquid, allowing smaller diameter probes and a more conformal technique. Cryotherapy is typically administered via the perineum under ultrasound guidance. Cell destruction occurs primarily from disruption of the cellular membrane, leading to necrosis and vascular thrombosis.

Based on available data, whole gland cryotherapy provides intermediate term biochemical control in a reasonable proportion of patients but it results in a high rate of erectile dysfunction. As a focal therapy treatment, feasibility has been shown but it has yet to be formally or extensively studied. Cryotherapy may lack the requisite precision for focal

Table 12.1. *Focal therapy modalities*

Focal therapy modalities				
	HIFU	**Cryotherapy**	**Radiation therapy**	**PDT**
Mechanism	Thermal induced protein denaturation + coagulative necrosis	Disruption of cellular membrane + delayed vascular occlusion	DNA damage, cell damage apoptosis	Light activated, oxygen dependent effects vascular occlusion
Application	Transrectal with cooling device	Transperineal	apoptosis XRT, brachytherapy (removable or permanent seed implants)	Transperineal light fibers
Available systems	Ablatherm®, Sonablate®500	AccuProbe®, SeedNet™, Cryocare®	Numerous	Tookad in phase I/II trials for vascular targeted phototherapy
Retreatment	Yes	Yes	Depends on dose delivered to surrounding normal tissues	Yes
Limitations	Treating anterior tumors + small prostates	Treating large prostates	XRT (prostate motion + proximity of bowel to target region), brachytherapy (large prostates + pts with significant urinary symptoms)	Unknown
Anesthesia	General or regional	General or regional	XRT (none), brachytherapy or HDR (general or regional)	General or regional
Treatment monitoring	MRI or ultrasound	Ultrasound + thermosensors	CT, ultrasound, fluoroscopy, cystoscopy	MRI or ultrasound

ablation with minimal disruption of normal function.

12.2 Radiation Therapy

RT has traditionally been administered to the entire gland by external beam or brachytherapy. Technological progress has allowed RT to be concentrated more selectively and recently to dose intensify predetermined regions of the prostate. The ability to dose escalate is notable since the likelihood of long-term cancer control is directly associated with the radiation dose. Three-dimensional conformal therapy delivers the intended radiation dose to the target area while limiting irradiation of critical surrounding structures, such as the bladder and rectum.

Intensity Modulated Radiation Therapy (IMRT) further achieves these objectives by providing an unprecedented focal application of radiation dose to pre-specified areas. With IMRT, Zelefsky et al achieved excellent long-term biochemical control rates while improving the toxicity profile by sparing adjacent organs from treatment related effects [104].

RT appears to be particularly suitable for study as a focal treatment option. It has an

established biological basis, known tumoricidal activity, and familiarity to radiotherapists and urologists. When applied as focal therapy its use remains investigational since the effects of radiation scatter, long-term tumor control rates and ability to re-treat are unknown.

12.3 Photodynamic therapy

In PDT a topically or systemically administered photosensitizer accumulates in a target tissue, where it can be activated by light. Activation of the photosensitizer leads to the generation of active radicals that are toxic to the tissue.Most current photosensitizers are porphyrin derivatives that primarily target the cellular compartment of a tumor. PDT was first used to treat skin lesions and then tested in cancers of the breast, central nervous system, head and neck, lung, esophagus, cervix, bladder and prostate. Clinical studies have been done using PDT for prostate cancer but its use remains experimental. Given the preclinical demonstration of tumor destruction and clinical evidence suggesting a favorable side effect profile, Vascular-targeted Photodynamic Therapy (VTP) is now also being explored in phase II trials for the preliminary treatment of localized prostate cancer. These ongoing and future trials will define the role of VTP in the treatment of prostate cancer.

12.4 High Intensity Focused Ultrasound (HIFU)

In HIFU treatment a convergent beam of high intensity ultrasound is emitted by a highly focused piezocomposite transducer in shots lasting a few seconds. The sudden and intense absorption of the ultrasound beam at the focal point provokes a sharp temperature increase (about 85°C) that causes irreversible necrosis of tissue in the target area. Ultrasound energy is tightly focused, absorbed and converted to heat, resulting in a sharp delineation between ablated and undamaged tissue. Accordingly, hundreds of cycles are often required for complete treatment. The size and location of the ablated area is modifiable based on the focusing system, ultrasound frequency, and the duration and absorption coefficient of the tissue.
HIFU has been used for cancers of the liver, kidney, pancreas and breast, and as treatment for uterine fibroids using MR guidance. However, its most widely studied application is for prostate cancer. Using general or regional anesthesia and a transrectal probe equipped

with a cooling device, real-time ultrasound visualization monitors the treatment effect. Limitations include difficulty in treating the anterior prostate or smaller prostates and a lack of long-term data. One of 2 systems is typically used, the Ablatherm® or Sonablate® 500.
HIFU has generally been intended for whole gland ablation, and early results with HIFU appear encouraging in the context of study limitations for properly selected patients with clinically organ confined disease. Since the overall experience is limited and follow-up is immature, long-term cancer control rates and more comprehensive analyses of treatment morbidity are necessary before advocating more widespread use of HIFU. Because HIFU has been used predominantly as whole gland therapy, additional experience will determine whether it can be successfully applied to focal lesions.
Magnetic resonance imaging is an outstanding modality for guiding placement of an interventional device into the prostate due to its excellent soft tissue contrast and multi-planar capabilities. However, the greatest reason to use MRI to guide ultrasound ablation of the prostate is its ability to quantify tissue temperature. MR thermometry yields images of the maximum temperature reached during the treatment, the thermal dose, and the temperature time product [105, 106, 107]. It has been recognized that the most significant problem for in vivo MR thermometry has been its sensitivity to motion.

Once the treatment is done, the current gold standard to evaluate tissue viability is Contrast Enhanced (CE) MRI, in which tissue lacking perfusion appears as an area lacking signal enhancement. CE-MRI provides an excellent delineation of the necrotic tissue. However, since it involves the administration of contrast materials, repeat use after a second treatment is difficult due to the previously administrated contrast material that remains in the tissue. In addition, it cannot differentiate between treated areas and preexisting conditions such as cystic changes. For this reason, in this chapter I will explore the DWI capability to assess tissue damage and cell death, without relocating the patient and the applicators and without involving the administration of contrast agent.
The goals of this part of my thesis were to:

- optimize an EPI DWI sequence at 3T;
- demonstrate a drop in ADC similar to the one seen earlier in a previous study of the group [106];
- investigate changes in ADC values before and after ablation.

12.5 Methods

12.5.1 Experimental setup

A custom-made, high intensity ultrasound device was used to perform on 3 dogs transurethral thermal ablation with MR thermometry based closed-loop feedback control in a GE 3T scanner. The curvilinear applicator design utilized an array of two transducers measuring 3.5mm×10mm (Fig. 12.1). The radius of curvature across the short axis of

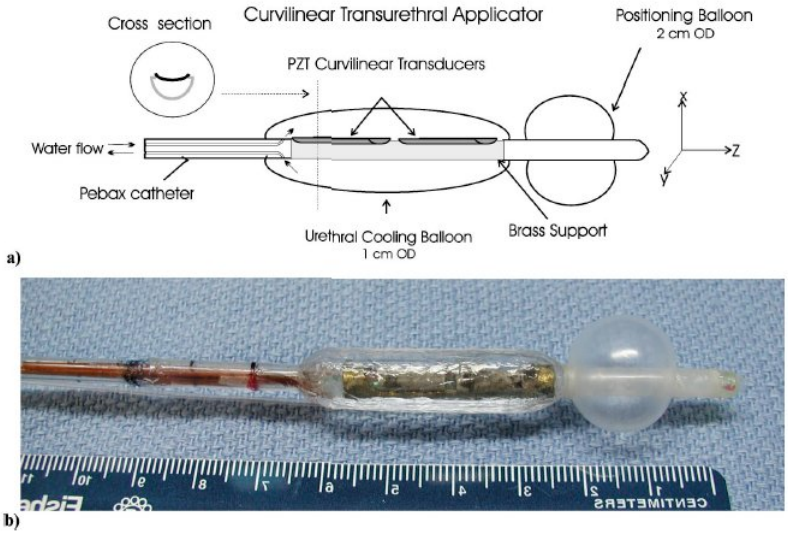

Figure 12.1. *a) Schematic drawing of the distal end of the curvilinear transurethral ultrasound applicator. b) Applicator photograph.*

the transducers was 15 mm and the operating frequency was 6.5 MHz. They were attached using silicone and conformal coating to a rectangular parallelepiped brass fixture (34×4.5×1.3 mm) with a window (25×3.5×0.3 mm) milled out of the brass for the transducers. A custom multilumen pebax catheter (50 cm×34 mm OD) (Danforth Biomedical Inc., Santa Clara, CA) formed the shaft of the applicator. Water flow from the catheter circulated within a thin walled polyester balloon (35×10 mm) that surrounded the brass structure. The water in this balloon removed excess heat from the transducers, cooled the urethra, and acoustically coupled the transducer to the tissue. The catheter assembly could be rotated within the cooling balloon via the proximal end of the applicator. A bladder retention balloon was attached to the tip of the applicator for proper positioning [108]. In vivo heating experiments with the curvilinear applicator were performed in three canine prostates using an open intervention MR system for guidance. Multiple single shot

and two sweeping procedures were performed in the three prostates. The transverse MR temperature profile at the end of one of the single sonications is shown in Fig 12.2. The total treatment time for the ablation of half the prostate in average was 42 min. Self-made

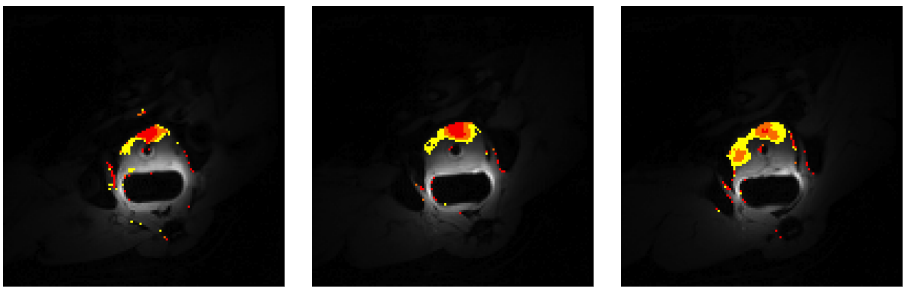

(a) (b) (c)

Figure 12.2. *MR temperature profiles at the end of single sonications for in vivo canine prostates (different slices from the same dog). Yellow pixels represent T=50°, orange T=55°, red=60°.*

EPI-DWI sequences with background suppression (DWIBS) were performed before and after the ablation to characterize water diffusion in prostate tissues. The most common diffusion imaging strategy, based on single-shot echo planar imaging (EPI) acquisitions, helps solve the motion problem but is prone to severe artifacts and geometric distortions from the chemical shift and the susceptibility effects prevalent in the abdomen and pelvis. Thus, in this project an alternative diffusion imaging strategy has been used. Different variants of DWIBS exist, but the basic idea is common to all of them. First, low ADC lipids are suppressed; second, DWI of the entire body or a region of interest is performed with considerable (for tissue outside the CNS) diffusion attenuation to make the low ADC structures stand out (eg, 500-1000 s/mm^2), whereas the remainder of the other tissues are suppressed; third, maximum intensity projections (MIPs) are computed at different projection angles to improve lesion visibility and facilitate diagnostic utility; and, fourth, an inverted gray scale is applied to the MIPs. That is, low ADC structures appear hypointense, whereas regular background appears bright to resemble scintigraphic images. The latter step is cosmetic and can be used depending on the preference of the interpreting radiologist.

To compute ADC value, we used 12 b-factor from 0 to 3500 s/mm^2 (0, 50, 100, 300, 500, 700, 1000, 1400, 1800, 2300, 2800, 3500), using a tetrahedral encoding scheme to increase signal-to-noise (SNR) ratio.

Since b increases quadratically with the gradient strength, often more than one gradient

axis is applied simultaneously to boost the net diffusion-encoding gradient for a given echo time. A very effective encoding scheme is tetrahedral encoding which uses four encoding directions ($\mathbf{g_1} = [G_x\ G_y\ G_z]^T$; $\mathbf{g_2} = [-G_x\ G_y\ G_z]^T$; $\mathbf{g_3} = [G_x\ -G_y\ G_z]^T$; and $\mathbf{g_4} = [G_x\ G_y\ -G_z]^T$) applied simultaneously at full strength to uniformly measure diffusion in four different directions. All three gradient axes are turned on simultaneously leading to an effective gradient that is $\sqrt{3}G_i(i = x, y, z)$. This scheme has proven useful to compute isotropically diffusion-weighted images with little extra time but SNR increased by up to a factor of about three compared to scans with encoding applied just along the principal gradient direction, i.e. along x, y, and z. However, because more effective gradients are involved, tetrahedral encoding usually demonstrates more eddy current effects than unidirectional encoding. Thus, when DWI scans with diffusion encoding along different directions are combined to compute an isotropically diffusion-weighted image, the resultant image will be blurred if the eddy current-induced distortions are not compensated.

12.5.2 Image Processing

Initially four averages were obtained at each b value, and direction, then the four directions have been averaged to obtain one image for each b-values. Two ROIs were identified on each ablated area on each prostate: a central area appearing darker on the DWI image (yellow ROI in Fig. 12.3(c)) and an outer ROI appearing brighter on the DWI image (cyan ROI in Fig. 12.3(c)). Even if studies have used a range of b-values assuming a monoexponential model to describe the changing signal from the prostate associated with an increasing diffusion gradient, there are some [109, 110] that have been assumed a biexponential model to evaluate prostate diffusion changing. This model has been taken from studies in the brain, indicating two components of diffusion in tissue, said "fast" and "slow" [111]. These fast and slow components are believed to arise from extracellular and intracellular diffusion processes, respectively, with slow diffusion also showing correlation with cell membrane density [112].
In addition to the tissue ROIs, noise measurements were made from an ROI within the air of the inflated balloon within the rectum, demonstrated above 4.4. The signal vs b- factor from each ROI, as extracted from the mean data sets were fit with both monoexponential functions and biexponential decay functions of the form:

$$S = Aexp(-bD_a) + Bexp(-bD_b) \tag{12.1}$$

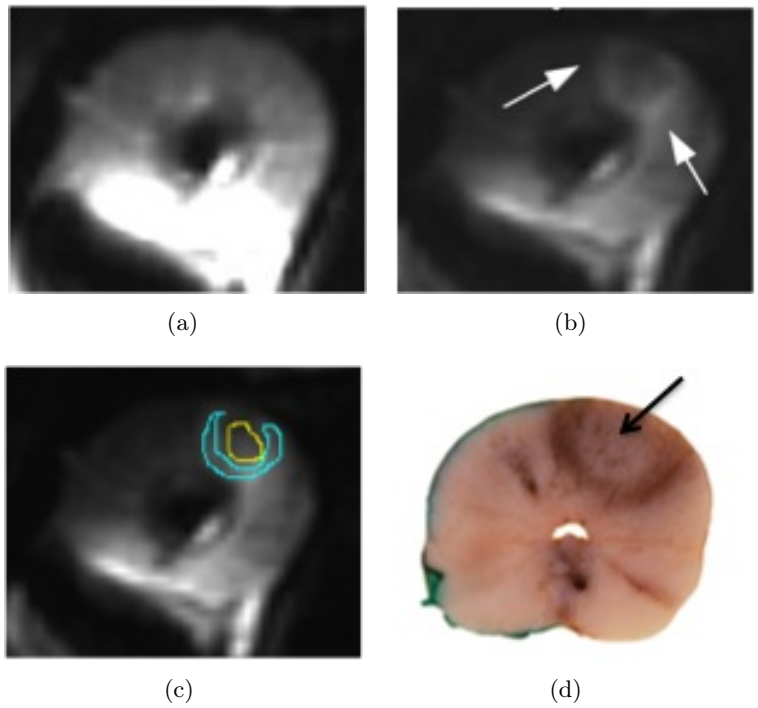

Figure 12.3. *a) DWI image at b-value 700 s/mm^2 obtained before the ablation. b) DWI image at b-value 700 s/mm^2 obtained after the ablation. White arrows point the ablated region, where it is visible a darker central area surrounded by a brighter area. Two ROIs are drawn on this regions (c). d) H&E image obtained after prostatectomy.*

where S is the signal intensity, b the b- factor, D_a and D_b the fast and slow diffusion coefficients, respectively, and A and B their amplitudes with the fraction of the fast diffusion component given by A/(A + B). Fits were performed with a Marquardt-Levenberg algorithm as implemented in Matlab software (The MathWorks, Inc., Natick, MA). The fits of the data to monoexponential decay curves (B = 0 in Eq 12.1)) were performed in order to allow for a comparison to determine whether the biexponential model provided a statistically improved fit over the monoexponential model. Finally histology with H&E was performed.

12.6 Results

This preliminary results suggested that, if a single b-value is to be obtained to monitor the HIFU treatment, the preferred is 700 s/mm^2, as this gives the highest CNR between

ablated and non-ablated tissue, in fact this b-value has a signal intensity decreasing comparable to 1000 and 1400, but a higher SNR (Table 12.2). Moreover, in this study we

Table 12.2. *Mean differences on 3 dogs between signal intensity before and after ablation. SNR computed for each b-value*

b-value	**Signal differences between pre and post ablation**	**SNR**
0		26.09
50	5.56%	27.90
100	-0.54%	26.59
300	-10.70%	23.11
500	-16.68%	19.98
700	**-18.63%**	**15.84**
1000	**-18.95%**	**11.69**
1400	**-18.18%**	**8.44**
1800	-15.83%	6.92
2300	-13.53%	5.23
2800	-12.18%	4.75
3500	-10.74%	4.525

demonstrated that the biexponential model fits the data with a mean $R^2 = 0.998$, thus better than the monoexponential fit ($R^2 = 0.967$) (Fig 12.4). A bi-exponential decay of the signal increasing the b-values, suggesting the presence of two different type of diffusion, said fast and slow, who change in rate and fraction after thermal ablation. Eq. 12.2 and 12.3 show the mean fitting parameters obtained in the three dogs.
Central yellow ROI (Fig. 12.3(c))

$$\begin{aligned} S_{pre\_ablated} &= 0.71e^{-b_n 2.71} + 0.28e^{-b_n 0.83} \\ S_{post\_ablated} &= 0.49e^{-b_n 2.57} + 0.49e^{-b_n 0.40} \end{aligned} \tag{12.2}$$

Outer blue ROI (Fig. 12.3(c))

$$\begin{aligned} S_{pre\_ablated} &= 0.73e^{-b_n 2.60} + 0.26e^{-b_n 0.71} \\ S_{post\_ablated} &= 0.48e^{-b_n 2.35} + 0.50e^{-b_n 0.34} \end{aligned} \tag{12.3}$$

After ablation, there is a shift from fast to slow diffusion. In addition, each diffusion coefficient decreases after ablation, with the slow component decreasing more than the fast

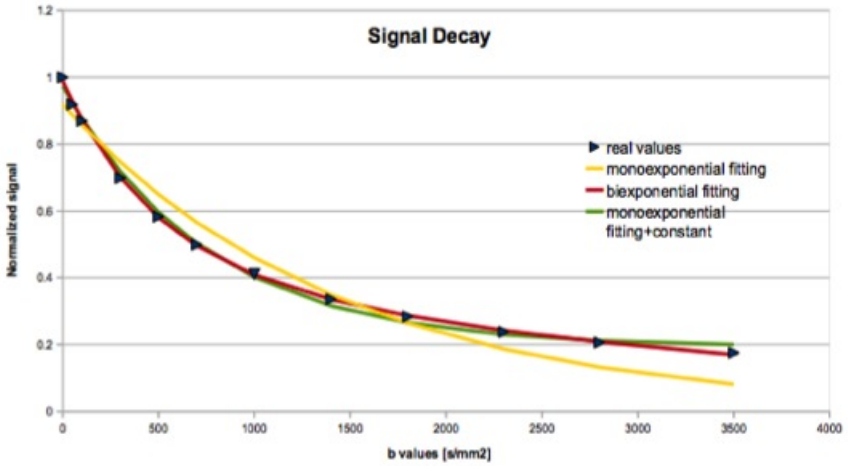

Figure 12.4. *Signal decay representing the fitting of real data acquired on one dog with monoexponential model (yellow line), biexponential model (red line) and a monoexponential + a constant model. The last model should be represent a noise signal presents in all the dataset.*

component. Finally, histology indicated two histologically different areas: a central core, where glands appeared to be intact, hence the name *heat-fixed*, surrounded by coagulative necrosis without heat fixation. These two areas match the two ROIs different areas visible in DWI images post ablation, indicating a different diffusivity according to the histological conditions (Fig. 12.5).

12.7 Discussion

This preliminary study demonstrates changes in the fast and slow diffusion rates and fractions after thermal ablation, suggesting the possibility to use DWI to monitor focal treatment, without contrast injection and without relocating the patient. In addition, this study showed differences in the diffusion rates in heat fixed vs. non-heat fixed ablated tissue.

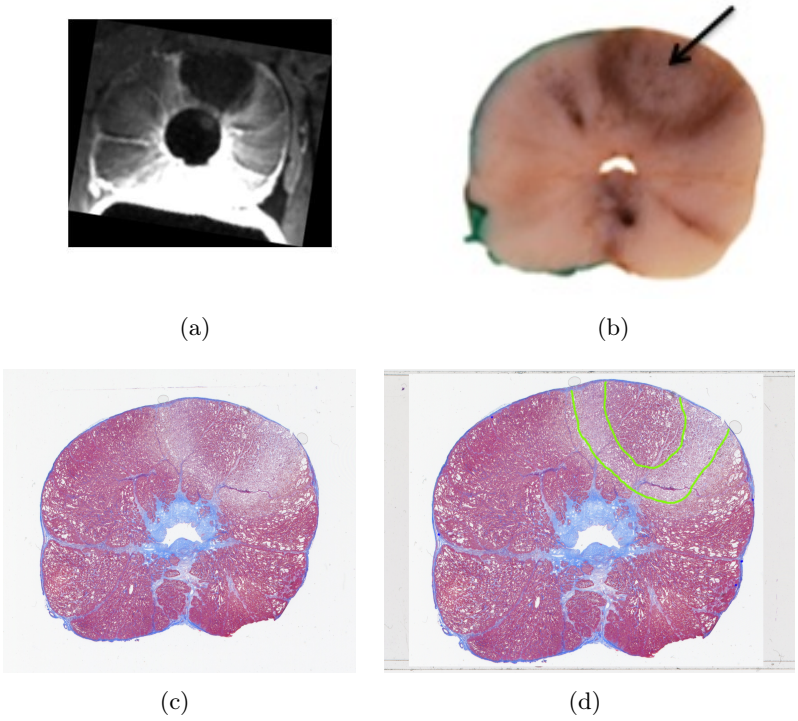

(a) (b)

(c) (d)

Figure 12.5. *a)CE-MRI image acquired after the ablation, manually registered to the histological image. b) Histology of the ablated area; the black arrow points the heat fixed area. c) Haematoxylin Eosin (H&E) fixed image of the ablated prostate; the brighter area indicates damaged cells. d) The ROIs previously drawn on the DWI image manually superimposed to the H&E fixed image. Registration was manually performed between DWI and H&E image; matching between the two ROIs and the histologically different areas is clearly visible.*

Chapter 13

Conclusions

In conclusion, advantages of this innovative workup for prostate cancer are summarized as follows:

1 CAD system using multispectral MRI could allow to diagnose PCa with a higher accuracy than current tests, distinguishing areas within the gland with cancer from those with normal or fibrous tissue. In this way, individuals with high PSA values and a negative CAD-MR exam could avoid core-biopsies, thus reducing anxiety, the diagnostic delay of a false-negative finding, procedure related complications and the adverse events linked to over-treatment.

2 In case of a positive finding, CAD-MR could be used to perform biopsy under MR guidance increasing the accuracy of the procedure. Furthermore, biopsy could allow us not only to confirm the diagnosis of PCa but also possibly to identify tumor areas having a different grading.

3 Imaging guided procedures, such as cryotherapy or MR guided High Intensity Focused Ultrasound (MRgFUS) could be performed having accurate color parametric 3D maps of the tumor available to plan treatment. MR can monitor temperature and DWI can assess the success of the treatment by measuring the necrosis within the area of treatment if the procedure is performed directly in the MR unit, as is the case of MRgFUS.

However, all the steps here presented (registration, lesion detection) need to be unified in a sole stand-alone system, as it has been done for the breast CAD system, in order to validate the CAD in a larger dataset. If the CAD system will be sufficiently accurate

in a laboratory setting we will conduct a prospective feasibility clinical trial to assess its new role in the diagnostic work-up of patients with PCa. It is our intention to promote a multicenter study, if the preliminary trial is successful.

Bibliography

[1] Doi K, *Diagnostic imaging over the last 50 years: research and development in medical imaging science and technology.* Phys Med Biol 2006;51(13):R5-27.

[2] Friedman CP, Elstein AS, Wolf FM, Murphy GC, Franz TM, Heckerling PS, Fine PL, Miller TM and Abraham V, *Enhancement of clinicians diagnostic reasoning by computer-based consultation: a multisite study of 2 systems.* JAMA 1999;282:1851-6.

[3] Van Ginneken B, Ter Haar Romeny BM and Viergever MA *Computer-aided diagnosis in chest radiography: a survey.* IEEE Trans Med Im 2001;20:1228-41.

[4] Kawamoto K, Houlihan CA, Balas EA, Lobach DF, *Improving clinical practice using clinical decision support systems: a systematic review of trials to identify features critical to success.* BMJ 2005;330(7494):765.

[5] Sampat MP, Markey MK and Bovik AC *Computer-aided detection and diagnosis in mammography Handbook of Image and Video Processing* 2005:1195-217.

[6] Boyle P, Ferlay J, *Cancer incidence and mortality in Europe, 2004.* Annals of Oncology 2005;16:481-488.

[7] Mahoney M et al, *Opportunities and Strategies for Breast Cancer Prevention Through Risk Reduction.* CA Cancer J Clin 2008;58:347-371.

[8] Jemal A, Siegel R, Ward E et al, *Cancer Statistics, 2006.* CA Cancer J Clin 2006;56:106-130.

[9] Shibata A, Ma J, Whittemore AS. *Prostate cancer incidence and mortality in the United States and the United Kingdom.* J Natl Cancer Inst. 1998;19;90(16):1230-1.

[10] Bray F, Sankila R, Ferlay J, Parkin DM. *Estimates of cancer incidence and mortality in Europe in 1995.* Eur J Cancer. 2002;38(1):99-166.

[11] Sardanelli F, Giuseppetti GM, Canavese G et al. *Indications for breast magnetic resonance imaging. Consensus document.* Radiol Med 2008;113(8):1085-1095.

[12] Candefjord S, Ramser K, Lindahl OA, *Technologies for localization and diagnosis of*

prostate cancer. J Med Eng Technol. 2009;33(8):585-603.

[13] Turkbey B, Pinto PA, Choyke PL, *Imaging techniques for prostate cancer: implications for focal therapy.* Nat Rev Urol. 2009 Apr;6(4):191-203.

[14] Liu X, Langer D, Haider MA, Yang Y, Wernick MN and Yetik IS, *Prostate Cancer Segmentation With Simultaneous Estimation of Markov Random Field Parameters and Class.* IEEE Trans Med Imag 2009;28(6):906-915.

[15] Tonini T, Rossi F, Claudio P *Molecular basis of angiogenesis and cancer.* Oncogene 2003;22:6549-6556.

[16] Ehrmann R, Knoth M, *Choriocarcinoma. Transfilter stimulation of vasoproliferation in the hamster cheek pouch. Studied by light and electron microscopy.* J Natl Cancer Inst 1968;41:1329-1341.

[17] Folkman J, *Tumor angiogenesis: therapeutic implications.* New Engl J Med, 1971;285:1182-1186.

[18] Jain RK, Di Tomaso E, Duda DG, Loeffler JS, Sorensen AG, Batchelor TT, *Angiogenesis in brain tumours.* Nature 2007;28:610-622.

[19] Brasch R, Turetschek K, *MRI characterization of tumors and grading angiogenesis using macromolecular contrast media: status report.* Eur J Radiol 2000;34:148-155.

[20] Taylor JS, Tofts PS, *MR imaging of tumor microcirculation: Promise for the new millennium.* JMRI 1999;10:903-907.

[21] Hassid Y, Eyal E, Margalit R, Furman-Haran E, Degani H, *Non-Invasive Imaging of Barriers to Drug Delivery in Tumours.* Microvascular Research 2008;76(2):94-103.

[22] Miller JC, Pien HH, Sahani D, Sorensen AG, Thrall JH, *Imaging Angiogenesis: Applications and Potential for Drug Development.* Journal of the National Cancer Institute 1995;97(3):172-87.

[23] Muller RN, Rinck PA *MRI contrast agents vary in stability, chelate power.* Diagnostic Imaging May 1, 2009.

[24] Jackson A, Buckley DL, Parker GJ, *Dynamic contrast-enhanced magnetic resonance imaging in oncology.* Springer University Press; 2004.

[25] Roberts TPL, *Physiologic measurements by contrast-enhanced MR imaging: Expectations and limitations.* JMRI 1997;7:82-90.

[26] Tofts PS, Brix G, Buckley DL, Evelhoch JL, Henderson E, Knopp MV et al, *Estimating kinetic parameters from dynamic contrast-enhanced T_1-weighted MRI of a diffusable tracer: standardized quantities and symbols.* JMRI 1999;10:223-32.

[27] Koh DM, Padhani AR, *Diffusion-weighted MRI: a new functional clinical technique for tumour imaging.* The British Journal of Radiology 2006;79:633-635.

[28] Callaghan P. *Principles of Nuclear Magnetic Resonance Microscopy.* Clarendon Press, 1991.

[29] Liang ZP, Lauterbur PC, *Principles of Magnetic Resonance Imaging, A Signal Processing Perspective.* IEEE Press Series in Biomedical Engineering. The Institute of Electrical and Electronics Engineers, 2000.

[30] Merbach AE, Toth E, editors. *The Chemistry of Contrast Agents in Medical Magnetic Resonance Imaging.* John Wiley & Sons, 2001.

[31] Haake EM, Brown RW, Thompson MR, Venkatesan R, *Magnetic Resonance Imaging, Physical Principles and Sequence Design.* Wiley Liss, 1999.

[32] Stehling MJ, Howseman AM, Ordidge RJ, et al, *Whole-body echo-planar MR imaging at 0.5 T.* Radiology 1989;170:257-263

[33] Mansfield P, *Real-time echo-planar imaging by NMR.* Br Med Bull 1984;40:187-190.

[34] Feinberg DA, Turner R, Kakab PD, von Kienlin M, *Echo-planar imaging with asymmetric gradient modulation and inner-volume excitation.* Magn Reson Med 1990;13:162-169.

[35] Li Bihan D, Breton E, Lallemond D, Grenier P, Cabanis E, Laval-Jeantet M, *MR imaging of intravoxel incoherent motions: application to diffusion and perfusion in neurologic disorders.* Radiology;1986; 161:401-407.

[36] Delfaut EM, Beltran J, Johnson G, Rousseau J, Marchandise X, Cotten A, *Fat Suppression in MR Imaging: Techniques and Pitfalls.* RadioGraphics 1999;19:373-382.

[37] Chakraborti KL. et al, *Magnetic resonance imaging of breast masses: Comparison with mammography.* Breast Imaging 2006;15(3):381-387.

[38] Kuhl CK, *The Current Status of Breast MR Imaging. Part I. Choice of Technique, Image Interpretation, Diagnostic Accuracy, and Transfer to Clinical Practice.* Radiology 2007;244(2):356-78.

[39] Montemurro F et al, *Relationship between DCE-MRI morphological and functional features and histopathological characteristics of breast cancer.* European Radiology 2007;17(6):1490-1497.

[40] Kuhl CK *Current Status of Breast MR Imaging.Part 2. Clinical Applications.* Radiology 2007;244(3):672-91.

[41] Fausto A, Magaldi A, Babaei Paskeh B, Menicagli L, Lupo EN, Sardanelli F, *MR imaging and proton spectroscopy of the breast: how to select the images.* Radiol Med

2007;112(7):1060-1068.

[42] Liney GP, Gibbs P, Hayes C, Leach MO, and Turnbull LW, *Dynamic contrast-enhanced MRI in the differentiation of breast tumors: User-defined versus semiautomated region-of-interest analysis.* JMRI 1999;10:945-949.

[43] Mussurakis S, Buckley DL and Horsman A, *Dynamic MRI of invasive breast cancer: Assessment of three region-of-interest analysis methods.* J Comput Assist Tomogr 1997;21:431-438.

[44] Niemeyer T, Wood C, Stegbauer K and Smith J, *Comparison of automatic time curve selection methods for breast MR CAD.* Proceedings SPIE, Medical Imaging 2004: Image Processing, Vol. 5370, 2004.

[45] Ertaş G et al, *Breast MR segmentation and lesion detection with cellular neural networks and 3D template matching.* Comp Biol and Med 2008;38(1):116-126.

[46] Twellmann T, Saalbach A, Mueller C, Nattkemper TW, Wismueller A, *Detection of suspicious lesions in dynamic contrast-enhanced MRI data.* Conf Proc IEEE Eng Med Biol Soc 2004;1:454-7.

[47] Woods BJ, Clymer BD et al, *Malignant-lesion segmentation using 4D co-occurence texture analysis applied to dynamic contrast-enhanced magnetic resonance breast image data.* JMRI 2007;25:495-501.

[48] Kuhl CK, Mielcareck P, Klaschik S, Leutner C, Wardelmann E, Gieseke J, Schild HH, *Dynamic Breast MR Imaging: Are Signal Intensity Time Course Data Useful for Differential Diagnosis of Enhancing Lesions?* Radiology 1999;211:101-110.

[49] American College of Radiology, *ACR practice guideline for the performance of magnetic resonance imaging (MRI) of the breast.* Practice guidelines and technical standards 2004. Reston, VA, 2004.

[50] Mann RM, Kuhl CK, Kinkel K, Boetes C, *Breast MRI: guidelines from the European Society of Breast Imaging.* Eur Radiol 2008;18(7):1307-1318.

[51] Otsu N, *A threshold selection method from grey-level histograms.* IEEE T. Syst. Man Cyb. 9(1):62-66, 1979.

[52] Lu W et al, *DCE-MRI segmentation and motion correction based on active contour model and forward mapping* IEEE SNPD, Las Vegas, Nevada, USA, 2006;2006:208-212.

[53] Giannini V, Vignati A, Morra L et al, *A fully automatic algorithm for segmentation of the breasts in DCE-MR images.* Conf Proc IEEE Eng Med Biol Soc. 2010;2010:3146-9.

[54] Rueckert D, Sonoda LI, Hayes C, Hill DL, Leach MO, Hawkes DJ, *Nonrigid registration using free-form deformations: application to breast MR images.* IEEE Trans Med Imaging 1999;18:712-721.

[55] Ibáñez L, Schroeder W, Lydia NQ et al, *The ITK Software Guide, First Edition, Kitware Inc.* 2005.

[56] Mattes D, Haynor D, Vesselle H, Lewellyn TWE, *Nonrigid multimodality image registration*, Proceedings of the Medical Imaging Conference of SPIE, International Society for Optical Engineering, 2004;4322:1609-1620.

[57] Broyden C, *The convergence of a class of double-rank minimization algorithms 1. General considerations*, IMA J Appl Math 1970;6:76-90.

[58] Hill DL, Batchelor PG, Holden M, Hawkes DJ, *Medical Image Registration.* Phys Med Biol. 2001 Mar;46(3):R1-45. Review.

[59] Gribbestad I, Gjesdal K, Nilsen G, Lundgren S, Hjelstuen M, Jackson A, *An introduction to dynamic contrast-enhanced MRI in oncology.* In: Jackson A, Buckley D, Parker GJM, editors. Dynamic contrast-enhanced magnetic resonance imaging in oncology. Heidelberg:Springer Verlag; 2005:3-20.

[60] cology. Heywang-Kobrunner SH, Beck R, *Contrast-enhanced MRI of the breast.* New York: Springer;1996:229.

[61] Carbonaro LA, Verardi N, Di Leo G, Sardanelli F, *Handling a high relaxivity contrast material for dynamic breast MR imaging using higher thresholds for the initial enhancement.* Invest Radiol 2010;45:114-120.

[62] Sardanelli F, Fausto A, Esseridou A, Di Leo G, Kirchin MA, *Gadobenate dimeglumine as a contrast agent for dynamic breast magnetic resonance imaging: effect of higher initial enhancement thresholds on diagnostic performance.* Invest Radiol 2008;43:236-242.

[63] Antiga L, *Generalizing vesselness with respect to dimensionality and shape.* The Insight Journal (2007).

[64] Sato et al, *Three-dimensional multi-scale line filter for segmentation and visualization of curvilinear structures in medical images.* Medical Image analysis 1998;2(2):143-168.

[65] Greene FL, American Joint Committee on Cancer, American Cancer Society, *AJCC cancer staging manual.* 6th edition. New York: Springer-Verlag; 2002. xiv, 421 p.

[66] Dietzel M, Baltzer PA, Vag T, et al, *Differential diagnosis of breast lesions 5 mm or less: is there a role for magnetic resonance imaging?.* J Comput Assist Tomogr 2010;34:456-464.

[67] Penn A, Thompson S, Brem R, et al, *Morphologic blooming in breast MRI as a characterization of margin for discriminating benign from malignant lesions.* Acad Radiol 2006;13:1344-1354.

[68] Fischer DR, Wurdinger S, Boettcher J, Malich A, Kaiser WA, *Further signs in the evaluation of magnetic resonance mammography: a retrospective study.* Invest Radiol 2005;40:430-435.

[69] Kurz KD, Steirthaus D, Klar V, et al, *Assessment of three different software systems in the evaluation of dynamic MRI of the breast.* Eur J Radiol 2009;69:300-307.

[70] Kirbas C., Quek F. *A review of vessel extraction techniques and algorithms*, ACM Computing Surveys, 36(2): 81-121, 2004.

[71] Freiman M., Joskowicz L., Sosna J. *A variational method for vessels segmentation: algorithm and application to liver vessels visualization.* Proceedings of SPIE, 7261, 2009.

[72] *Breast imaging reporting and data system (BIRADS). 2003.* Available at: http://www.acr.org/SecondaryMainMenuCategories/quality_safety/BIRADSAtlas/BIRADSAtlasexcerptedtext/BIRADSMRIFirstEdition.aspx. Accessed September 2011.

[73] Gilhuijs KG, Giger ML, Bick U, *Computerized analysis of breast lesions in three dimensions using dynamic magnetic-resonance imaging.* Med Phys 1998;9:1647-1654.

[74] Gilhuijs KG, Deurloo E et al, *Breast MR imaging in women at increased lifetime risk of breast cancer: clinical system for computerized assessment of breast lesions.* Radiology 2002;225:907-916.

[75] Gibbs P, Turnbull L, *Textural analysis of contrast-enhanced images of the breast.* Magn Reson Med 2003;50:92-98.

[76] Gal Y, Mehnert A, Bradley A et al, *Feature and Classifier Selection for Automatic Classification of Lesions in Dynamic Contrast-Enhanced MRI of the breast*, Proceedings Digital Image Computing: Techniques and Applications, DICTA 2009:132-139.

[77] Agliozzo S, De Luca M, Martincich L et al, *A Multiparametric Model Combining a Selection of Morphological, Kinetic, and Spatio-temporal Features of Mass-like Lesions at Breast MRI* Proceedings of RSNA Annual Meeting, November 28- December 3, Chicago IL (2010). Available at: http://rsna2010.rsna.org/search/search.cfm?action=add&filter=Author&value=89595.

[78] Eshelman LJ, *The CHC adaptive search algorithm*, Foundations of genetic Algorithms 1991, Ed San Mateo, CA.

[79] Kohavi R and G. John, *Wrappers for feature subset selection*, Artif Intell 1997;97:273-324.

[80] Barber CB, Dobkin DP, Huhdanpaa HT, *The Quickhull Algorithm for Convex Hulls*, ACM Trans Math Software 1996;22:469-483.

[81] Zhang T, Nagy G, *Surface turtuosity and its application to analyzing cracks in concrete*, Proceeding of the IAPR International Conference on Pattern recognition 2004:851-854.

[82] Koenderink J, *Solid Shape*, MIT Press, Cambridge, MA, 1990.

[83] Tofts PS, *Modelling Tracer Kinetics in Dynamic Gd-DTPA MR Imaging* JMRI 1997;7:91-101.

[84] Henderson E, Rutt BK, Lee TY, *Temporal sampling requirements for the tracer kinetics modeling of breast disease*, Magn Reson Imaging 1998;6:1057-1073.

[85] D'Amico AV, *Biochemical Outcome after Radical Prostatectomy or External Beam Radiation Therapy for Patients with Clinically Localized Prostate Carcinoma in the Prostate Specific Antigen Era*, Cancer 2002;95:281-286.

[86] Roemeling S. et al, *Management and Survival of Screen-Detected Prostate Cancer Patients who Might Have Been Suitable for Active Surveillance.* European Urology 2006;50:475-482.

[87] Postma R and Schröder FH, *Screening for prostate cancer.* EJCA 2005;41:825-833.

[88] Jones JS, Patel A, Schoenfield L, Rabets JC, Zippe CD, Magi-Galluzzi C, *Saturation technique does not improve cancer detection as an initial prostate biopsy strategy.* J Urol 2006;175(2):485-488.

[89] Lujan M, Paez A, Santonja C, Pascual T, Fernandez I, Berenguer A, *Prostate cancer detection and tumor characteristics in men with multiple biopsy sessions.* Prostate Cancer Prostatic Dis. 2004;7(3):238-242.

[90] Hoffman RM, Hunt WC, Gilliland FD, Stephenson RA, Potosky AL, *Patient satisfaction with treatment decisions for clinically localized prostate carcinoma. Results from the Prostate Cancer Outcomes Study.* Cancer 2003; 97(7):1653-1662.

[91] DeSouza NM, Reinsberg SA, *Magnetic resonace imaging in prostate cancer: the value of apparent diffusion coefficients for identifying malignant nodules.* British Journal of Radiology 2007;80:90-95.

[92] Jezzard P, Balaban RS, *Correction for geometric distorsion in echo planar images from B0 field variations.* MRM 1995;34:65-73.

[93] Kozlowski P, Chang SD, Goldenberg SL, *Diffusion-weighted MRI in prostate cancer*

- *comparison between single-shot fast spin echo and echo planar imaging sequences* Magnetic Resonance Imaging 2008;26:72-76.

[94] Koh DM, *Diffusion-weighted MR Imaging, Applications in the body.* H. C. Thoeny (Eds.), Springer 2010.

[95] Padhani AR, Hayes C, Landau S, Leach MO, *Reproducibility of quantitative dynamic MRI of normal human tissues.* NMR Biomed. 2002 Apr;15(2):143-53.

[96] Melbourne A, Hipwell J, Modat M, Mertzanidou T, Huisman H, Ourselin S, Hawkes DJ, *The effect of motion correction on pharmacokinetic parameter estimation in dynamic-contrast-enhanced MRI.* Phys Med Biol 2011 Dec 21;56(24):7693-708.

[97] Thevenaz P and Unser M, *A pyramid approach to sub-pixel image fusion based on mutual information*, Proc. 1996 IEEE Int. Conf. Image Processing (ICIPâĂŹ96), vol. I, Lausanne, Switzerland, Sept. 16âĂŞ19, pp. 265-268.

[98] Studholme C, Hill DLG, and Hawkes DJ, *An overlap invariant entropy measure of 3D medical image alignment* Pattern Recogn 1999;32:71-86.

[99] Maes F, Collignon A, Vandermeulen D, Marchal G, and Suetens P, *Multimodality image registration by maximization of mutual information.* IEEE Trans Med Imag 1997;16:187-198.

[100] Maes F, Vandermeulen D, Suetens P, *Comparative evaluation of multiresolution optimization strategies for multimodality image registration by maximization of mutual information.* Med Image Anal 1999 Dec;3(4):373-86.

[101] Horsfield MA and Morgan B, *Algorithms for calculation of kinetic parameters from T1-weighted dynamic contrast-enhanced magnetic resonance imaging.* J Magn Reson Im 2004; 20:723-729.

[102] Castorina P, Delsanto PP, et al, *Classification Scheme for Phenomenological Universalities in Growth Problems in Physics and Other Sciences*, Phys Rev Lett 2006; 96:188701.

[103] Hanley JA, McNeil BJ, *The Meaning and Use of the Area under a Receive Operating Characteristic (ROC) Curve.* Radiology 1982; 743:29-36.

[104] Zelefsky MJ, Fuks Z, Hunt M, Yamada Y, Marion C, Ling CC et al, *High-dose intensity modulated radiation therapy for prostate cancer: early toxicity and biochemical outcome in 772 patients.* Int J Radiat Oncol Biol Phys 2002;53:1111.

[105] Peters RD, Chan E, Trachtenberg J, et al, *Magnetic resonance thermometry for predicting thermal damage: an application of interstitial laser coagulation in an in vivo canine prostate model.* Magn Reson Med 2000;44:873-883.

[106] Chen J, Daniel BL, Diederich CJ, Bouley DM, van den Bosch MA, Kinsey AM, Sommer G, Pauly KB, *Monitoring prostate thermal therapy with diffusion-weighted MRI.* . Magn Reson Med 2008;59(6):1365-72.

[107] Hazle JD, Diederich CJ, Kangasniemi M, et al, *MRI-guided thermal therapy of transplanted tumors in the canine prostate using a directional transurethral ultrasound applicator.* J Magn Reson Imaging 2002;15:409-417.

[108] Ross AB, Diederich CJ, Nau WH, Rieke V, Butts RK, Sommer G, Gill H, Bouley DM, *Curvilinear transurethral ultrasound applicator for selective prostate thermal therapy.* Med Phys 2005;32(6):1555-65.

[109] Mulkern RV, Barnes AS, Haker SJ, Hung YP, Rybicki FJ, Maier SE, Tempany CM, *Biexponential Characterization of Prostate Tissue Water Diffusion Decay Curves Over an Extended b-factor Range.* Magn Reson Imaging 2006;24(5):563-8.

[110] Riches SF, Hawtin K, Charles-Edwards EM, de Souza NM, *Diffusion-weighted imaging of the prostate and rectal wall: comparison of biexponential and monoexponential modelled diffusion and associated perfusion coefficients.* NMR Biomed. 2009;22(3):318-25.

[111] Mulkern RV, et al, *Multi-component apparent diffusion coefficients in human brain.* NMR Biomed 1999;12: 51-62.

[112] Sehy JV, Ackerman JJ, Neil JJ, *Evidence that both fast and slow water ADC components arise from intracellular space.* Magn Reson Med 2002; 48: 765-770.